University of Alberta

Anatomically-Tailored Magnetic Resonance Radio Frequency Probes

by

Nicola De Zanche ©

A thesis submitted to the Faculty of Graduate Studies and Research in partial fulfillment of the requirements for the degree of **Doctor of Philosophy**.

in

Medical Sciences–Biomedical Engineering

and

Department of Electrical and Computer Engineering

Edmonton, Alberta
Spring 2002

National Library of Canada
Acquisitions and Bibliographic Services
395 Wellington Street
Ottawa ON K1A 0N4
Canada

Bibliothèque nationale du Canada
Acquisitions et services bibliographiques
395, rue Wellington
Ottawa ON K1A 0N4
Canada

Your file Votre référence

Our file Notre référence

The author has granted a non-exclusive licence allowing the National Library of Canada to reproduce, loan, distribute or sell copies of this thesis in microform, paper or electronic formats.

L'auteur a accordé une licence non exclusive permettant à la Bibliothèque nationale du Canada de reproduire, prêter, distribuer ou vendre des copies de cette thèse sous la forme de microfiche/film, de reproduction sur papier ou sur format électronique.

The author retains ownership of the copyright in this thesis. Neither the thesis nor substantial extracts from it may be printed or otherwise reproduced without the author's permission.

L'auteur conserve la propriété du droit d'auteur qui protège cette thèse. Ni la thèse ni des extraits substantiels de celle-ci ne doivent être imprimés ou autrement reproduits sans son autorisation.

0-612-68561-6

Canada

University of Alberta

Library Release Form

Name of Author: Nicola De Zanche

Title of Thesis: Anatomically-Tailored Magnetic Resonance Radio Frequency Probes

Degree: Doctor of Philosophy

Year this Degree Granted: 2002

Permission is hereby granted to the University of Alberta Library to reproduce single copies of this thesis and to lend or sell such copies for private, scholarly or scientific research purposes only.

The author reserves all other publication and other rights in association with the copyright in the thesis, and except as herein before provided, neither the thesis nor any substantial portion thereof may be printed or otherwise reproduced in any material form whatever without the author's prior written permission.

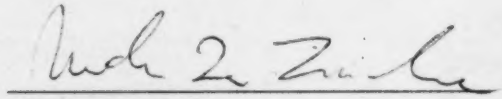

Nicola De Zanche
5505-54A Street
Barrhead, Alberta
T7N 1E3, Canada

Date: Jan. 4, 2002

University of Alberta

Faculty of Graduate Studies and Research

The undersigned certify that they have read, and recommend to the Faculty of Graduate Studies and Research for acceptance, a thesis entitled **Anatomically-Tailored Magnetic Resonance Radio Frequency Probes** submitted by Nicola De Zanche in partial fulfillment of the requirements for the degree of **Doctor of Philosophy** in *Medical Sciences–Biomedical Engineering.*

Peter S. Allen (Supervisor)

Frederick E. Vermeulen (Co-Supervisor)

Abdul Elezzabi

W.R. Wayne Martin

Richard E. Snyder

Alan H. Wilman

J. Thomas Vaughan Jr. (External Examiner)

Date: Jan. 3, 2002

The best theory
is
inspired by practice

◇◇◇

The best practice
is
inspired by theory

Donald E. Knuth

To the memory of

Angelo Drigo

Abstract

In-vivo nuclear magnetic resonance (NMR) techniques utilise the magnetic interaction between nuclei and the radio frequency (RF) probe to extract information about the nuclei and their environment. The efficiency of this interaction, or coupling, is strongly dependent on the geometric match between the probe and the sample, and determines the signal-to-noise ratio (SNR). Therefore, standard circular RF probe designs are not optimal for many regions of the human anatomy. In this thesis the coupling is improved by constructing probes with access bores tailored to specific anatomical regions.

This work begins with an analytical method to adapt either the birdcage or transverse electromagnetic (TEM) coil topology to any non-circular cross section encountered in practice, while allowing the production of magnetic fields having a high degree of uniformity like that of the standard circular coils. Both the placement of the probe's conductors as well as the shape of the probe's RF shield are determined analytically. The analytical method also shows that, although in general the shield contour that gives optimal field uniformity depends on the field's orientation, for the elliptical cross section a shield constructed on a *confocal* elliptical cylinder is ideal for any field orientation.

A prototype birdcage coil designed for the head was constructed on an oval of

Cassini, a curve similar to the ellipse but which maintains a more regular curvature even for high aspect ratios. At 3 Tesla the Cassinian coil offers a 20% improvement in SNR over a circular coil of comparable dimensions, against a theoretical maximum of 30% achievable with a lossless sample. Greater improvements can be expected at lower operating frequencies or with higher aspect ratios (e.g., for the pelvis or thorax).

In the second part of this thesis, a method using multiconductor transmission-line theory to perform the modal analysis of TEM resonators is extended to oval TEM coils as well as to birdcage coils. Experimental data from a circular birdcage coil shows excellent agreement between the predicted and measured resonance spectra. This model is also able to account for some of the finite-wavelength effects that are observable at high frequencies.

Acknowledgements

First and foremost I want to thank my supervisors, Drs. Peter Allen and Fred Vermeulen, who have been models and inspirations for my career, and without whose guidance and dedication this research would never have given the fruits that it has. The historical and practical knowledge of my external examiner, Dr. Thomas Vaughan, are also gratefully acknowledged, with regret for the short time we had to talk after the defense. I also wish to thank the other members of my examining committee, Drs. Abdul Elezzabi, Wayne Martin, Richard Snyder and Alan Wilman for carefully reading this thesis and pointing out many ways to improve it.

Much of what I know about NMR coil construction is due to the patient instruction of Mr. Al-Karim Damji and I also thank Dr. Terry Riauka for his (unsuccessful) efforts to make me into a proficient programmer. I thank Dan Gheorghiu for his steady willingness to de-bug our NMR system and to reveal its inner workings.

I must acknowledge my fellow graduate students, Rich, Kim, Steven, Osama, Jason, Dan, Keith, Mark and Adam for the many lunches, beers, jokes and soccer victories. I thank Dr. Jim Wild for the frequent and intense skiing that I hope to repeat after this thesis is finally submitted. Special thanks and encouragement go to Atiyah for the friendship, help and keen observations.

I thank the Alberta Heritage Foundation for Medical Research and the Natural Sciences and Engineering Research Council for the generous bursaries that have put bread on my table and gasoline in my car.

I will be eternally grateful to the community of St. Joseph's College, the Basilian

Fathers and the residents and alumni of the College for providing more than just a roof over my head, but also life-long friendships and countless parties. For the home-cooked meals that have kept my appetite satisfied I praise Denis and the tireless kitchen staff.

My family, including my grandfather to whom this thesis is dedicated, has been an example and inspiration since my childhood. I especially thank my parents Pietro and Laura, whose sacrifices and unconditional support have relented almost three decades.

Finally I thank my best friends Diana and Franco for the true and enduring friendships that will always be a part of me.

Contents

1 Introduction **1**

1.1 Physical Principles of NMR 2
1.1.1 Nuclear Magnetism 2
1.1.2 Bulk Magnetisation at Thermal Equilibrium 4
1.1.3 Perturbation and Evolution of the Excited Spin System 5
1.1.4 Signal Detection 9
1.1.5 Spatial Encoding Using $\mathbf{B_0}$ Gradients 9
1.2 *In-vivo* Applications of NMR 11
1.2.1 Basic Pulse Sequences 11
1.2.2 Magnetic Resonance Imaging 14
1.2.3 Functional MRI 15
1.2.4 Biochemical Analysis 16
1.3 RF Probe Technology 17
1.3.1 The Ideal RF Field 17
1.3.2 Common Radio Frequency Probe Designs 18
1.3.3 High-Frequency Effects on Field Homogeneity 27
1.3.4 The Signal-to-Noise Ratio in the NMR Experiment 28
1.3.5 Improvements in Signal-to-Noise Ratio from Anatomical Tailoring of RF Coils 31

2 Elliptical Birdcage Coils **41**

2.1 Introduction 41
2.2 Mathematical Analysis 42
2.2.1 The Circular Birdcage Coil (Discrete Implementation) 43
2.2.2 Circular Birdcage (Continuous Current Distribution) 45
2.2.3 Conformal Transformations 47
2.2.4 The Elliptical Birdcage Coil (Continuous Current Distribution) 49
2.2.5 Elliptical Birdcage (Discrete Implementation) 53
2.3 Results and Practical Considerations 56
2.3.1 Comparison of Circular and Elliptical Birdcage Coils 56

2.3.2 Coil Loading and Signal-to-Noise 57
2.3.3 Port Imbalance and Noise Performance in Quadrature Operation 58

3 Birdcage Coils on Oval Cylinders **64**
3.1 General Theory of Optimal Current Distributions 64
3.1.1 Unshielded Coils on a General Cross Section 64
3.1.2 Shielded Birdcage Coils 67
3.1.3 The Cassinian Head Coil Prototype 71
3.2 Modal Analysis and Capacitor Optimisation 75
3.2.1 Analytical Method for Calculation of Capacitances 75
3.2.2 Numerical Optimisation of Capacitances 77
3.3 Experimental Verification 79
3.3.1 Coil Construction and Tuning 79
3.3.2 Probe Quality Factor 82
3.3.3 Field and SNR Measurements 82
3.4 Conclusion 87
3.5 Appendix: Unique Properties of Confocal Elliptical Shielding 88

4 TEM Resonators on Oval Cylinders **92**
4.1 Inductance Matrix of the Cassinian Transmission Line 93
4.2 General Comments on the Calculation of Modal Currents 96
4.3 An Oval TEM Coil Designed for Linear-Mode Operation 98
4.4 A Quadrature Oval TEM Coil 102
4.5 Discussion 104

5 A High-Frequency Model of the Birdcage Coil **108**
5.1 Multiconductor Transmission Line Model 110
5.2 The Band-pass Circular Birdcage Coil Prototype 112
5.3 Concluding Remarks 112

6 Construction and Measurement Methods **116**
6.1 Coil Construction Methods and Materials 116
6.1.1 Mechanical Support 117
6.1.2 Conductors: Resistance and Inductance 118
6.1.3 Capacitors 119
6.2 Shielding and Grounding 121
6.3 Coupling Circuitry 123
6.3.1 Electric Coupling 123
6.3.2 Magnetic Coupling 124
6.3.3 Impedance Matching 124

6.3.4 Balance Transformers 125
6.4 Bench Measurements 126
6.4.1 Resonant Frequency 127
6.4.2 Quality Factor (Q) 128
6.4.3 Damping Factor, Efficiency and Dielectric Loss 129
6.4.4 Input Sensitivity 130
6.4.5 Port Isolation 130
6.5 NMR Measurements on Phantoms 130
6.5.1 Field Mapping with Small Samples 131
6.5.2 Field Mapping with Flood-Field Phantoms 132
6.6 *In-Vivo* NMR Measurements 133
6.6.1 Anatomical Imaging 133
6.6.2 Spectroscopy 133

7 Summary and Conclusions **138**
7.1 Theoretical Analysis 138
7.2 Experimental Validation 140
7.3 Future Directions 141

Appendices **143**

A Comments on TBME 47, p.535 **143**

B Cassinian Head Coil Programs **146**
B.1 Coil Capacitance Cost Function 146
B.2 Sample NEC-2 Command File 151

C Method of Images **159**
C.1 Location of the Equivalent Source Line 159
C.2 Image of a Magnetic Dipole 160

List of Tables

1.1 Several nuclei that have biological importance along with their spin quantum numbers, magnetogyric ratios and natural abundances. . . . 4

1.2 Relaxation times for several types of tissue along with their respective water content which is indicative of spin density. 8

2.1 Geometric sensitivities of elliptical birdcage coils appropriate for the head (major access diameter $2m_1 = 28$ cm, minor access diameter $2n_1 = 22$ cm) and the body ($2m_1 = 55$ cm, $2n_1 = 27.5$ cm) relative to those of corresponding circular coils having the same diameter as the major diameter of the ellipse. In the shielded case, the diameters of the shields are $2m_2 = 33$ cm and $2n_2 = 28$ cm for the head coil, and $2m_2 = 71$ cm and $2n_2 = 52.5$ cm for the body coil. Again the diameter of the corresponding circular shield is taken equal to the major diameter of the ellipse. For the shielded elliptical coils the improvements in sensitivity for the single modes are tabulated separately, together with their average, which corresponds to the improvement expected in reception when an ideal 90° phase shift is performed on one channel before summation with the other. The ratio of the modal sensitivities is equal to the axial ratio of the shield, as predicted by Eq. (2.21). . . 57

3.1 Initial and final values in the optimisation of the capacitances of the Cassinian head coil are shown for comparison with those used in the standard circular coil (last row). Nominal values used in the Cassinian coil are also indicated (the + sign indicates capacitors in parallel). Capacitances labelled C_i are on the end-ring segments, while C_{ij} are on the longitudinal segments of the coil (see Fig. 1.10(a)). The similarities in their capacitance values confirms that the electrical parameters of the two coils are related only by a small perturbation. All values are in picoFarads. 80

3.2 Comparison of the loaded and unloaded quality factors and damping ratios of the Cassinian and circular head coils. The Cassinian's higher damping ratios are indicative of better noise performance and higher efficiency (losses in the patient relative to the total losses). 82
3.3 Field polarisation ratios measured at coil centre: comparison of circular and Cassinian coil. An ideal circularly polarised field has a circular polarisation ratio of zero or equivalently a linear polarisation ratio of 1. 83

4.1 Element radii and termination capacitances needed for linear operation of the Cassinian TEM body coil having a length of 60 cm, access diameters 25.8 × 51.6 cm and shield diameters 40 × 60 cm. Elements are numbered from the one closest to the major axis and values for the remaining 12 elements are obtained by symmetry. 99
4.2 Resonant frequency and order of each mode of the Cassinian TEM body coil optimised for linear operation. 99
4.3 Angular locations in the circle plane, element radii and termination capacitances needed for quadrature operation of a Cassinian TEM body coil having a length of 60 cm, access diameters 25.8 × 51.6 cm and shield diameters 40 × 60 cm. Values for the remaining 9 elements are obtained by symmetry. 103
4.4 Resonant frequency and order of each mode of the Cassinian TEM body coil optimised for quadrature operation. 103

List of Figures

1.1 Precession of magnetic dipole moment $\boldsymbol{\mu}$ in a magnetic field $\mathbf{B}_0$. . . . 3

1.2 Zeeman splitting and eigenstates of a nucleus with spin quantum number $I = 1/2$ in a magnetic field of intensity B_0. 3

1.3 Orientation of individual magnetic moments in a macroscopic sample. a) In the absence of an external polarising field the moments are randomly oriented, while b) in the presence of an external field their average orientation is shifted in the direction parallel to the field to produce an observable magnetisation $\mathbf{M}$. 5

1.4 Trajectory of the net magnetisation vector $\mathbf{M}$ in the laboratory frame during a 90° pulse. Notice that the length of the vector is constant during RF excitation if the excitation is short compared with T_1 and T_2. 7

1.5 Trajectory of the net magnetisation vector in the laboratory frame during free precession with relaxation. Notice that the length of the vector is not constant. 7

1.6 Relaxation curves for tissues having T_2's differing by a factor of two. Differences in transverse magnetisation are greatest approximately halfway between the two time constants, shown by extrapolation of the initial slopes (dashed lines). 8

1.7 Typical time course of the free induction decay (FID), the signal induced in the receiver coil by the precessing magnetisation after a radio frequency excitation. All spins that contribute to this signal are assumed to precess at the same Larmor frequency. The envelope (dashed lines) of the FID represents the amplitude of the transverse component of the magnetisation. 10

1.8 Timing diagram for the spin echo imaging sequence. This sequence is repeated several times, each with a different value of the phase encode gradient (G_{pe}). 13

1.9 The gradient echo imaging sequence. 14

1.10 a) A section of birdcage ladder network, which is created by repeating the same cell N times and connecting the ends to create b) a circular structure that is often shielded to prevent interactions with other parts of the NMR scanner. The shield is shown with a sector removed for clarity. The inductors in a) represent the self inductances of the longitudinal conductors and end-ring sections, as well as the mutual couplings between segments that are not orthogonal. Leg currents are related to the mesh currents by $I_n = J_{n+1} - J_n$, $n = 0, 1, ...(N-1)$. . 20

1.11 a) Structure of the TEM resonator and b) its resonant modes, labelled according to their spatial frequency. The longitudinal elements may be flat strips, as illustrated, or cylindrical rods. Gaps between the ends of the longitudinal elements and the shield (shown with a sector removed for better viewing) are capacitively loaded. 24

1.12 Equivalent circuit for an NMR probe exhibiting parallel resonant characteristics. 30

2.1 Transverse magnetic field lines (quasi-static approximation) produced by shielded circular coils a) in a realistic implementation such as a birdcage coil or TEM coil with 16 elements and b) the ideal field which it seeks to approximate. 48

2.2 An illustration of the geometry of a confocally-shielded elliptical coil having an axial ratio appropriate, for example, for coupling to the pelvic region. The birdcage ladder network is constructed on an elliptically cylindrical surface $\mathcal{E}_1$, while the RF shield is on $\mathcal{E}_2$. The lines $x = \pm a$ are the foci of both cylinders. 50

2.3 Magnetic field lines of a) the major-axis and b) the minor-axis field modes of an idealised shielded elliptical coil wherein the inner ellipse is carrying an ideal continuous current density. The outer ellipse is seen to be an ideal shield that limits the RF coil's interaction with the rest of the NMR system, while preserving the ideal field homogeneity achievable without a shield. The difference in field amplitude between the two field orientations is due to the different geometric sensitivity of the two modes. 54

3.1 The quartic section coil (inner dotted curve) and shield contours. The continuous lines represent shield countours (calculated from Eqs. (3.5) using the same value of H_2 for both modes) that allow the production of perfectly uniform linearly-polarised fields. The actual shield shape that was used for the prototype coil is the larger dotted curve. 70

3.2 Elemental placement for a three-term truncation of the transformation function of Eq. (3.2) and the corresponding shield contours appropriate for fields oriented parallel to the coil axes (solid line for the major-axis field orientation and dotted line for the minor-axis orientation. The contours obtained for discrete current distributions are seen to be dependent on field orientation like their counterparts for continuous distributions, but also exhibit corrugations in correspondence to each filamentary current. 72
3.3 Magnetic field lines of a) the horizontal and b) the vertical field modes of the Cassinian head coil. The difference in field amplitude between the two field orientations is due to the different geometric sensitivities of the two modes. 76
3.4 The NEC wire model of the shielded Cassinian coil prototype includes thick grey segments to indicate the position of the capacitors on the ladder network and a wire mesh to model the shield. 78
3.5 The Cassinian coil prototype with shield removed for clarity. 81
3.6 Field amplitude plots normalised to maximum at coil centre: the circles (o) indicate field samples along the circular coil's axis obtained with a small spherical sample of water moved by 2cm intervals; the asterisks (*) indicate the field amplitudes along the Cassinian coil's axis. Axial field homogeneity is seen to be essetially identical for the two prototype coils. 84
3.7 Normalised axial and transverse spin-echo image profiles of a spherical oil phantom obtained using the Cassinian head coil and the standard circular coil for comparison. a) and b) are the superposition of two profiles obtained by acquiring two images with the phantom offset by ± 4 cm in the axial (z) direction, while for c) and d) the phantom was centered in the coil. Profile c) is taken along the major-axis direction of the oval coil. 85
3.8 Typical brain image obtained using the Cassinian coil prototype. The square indicates the region used to calculate the average signal for the image SNR measurements and also the approximate location of the voxel from which the spectra of Fig. 3.9 were obtained. 86
3.9 Spectra obtained from a $2 \times 2 \times 2$cm voxel in the occipital lobe using a PRESS sequence ($T_E = 120$ ms, $T_R = 4$ s, 32 averages). The SNR gain of a) the Cassinian coil over b) the circular coil is approximately 20%. 87

4.1 Magnetic field lines in a) the model (circle) plane and b) the problem plane of a TEM coil having a Cassinian shield. Only one element carries a net current while the others locally distort the field lines that it produces. The dashed lines indicate b) the oval of Cassini on which the coil elements are placed, and a) its image in the circle plane which is not a Cassinian. 95
4.2 Resonance spectrum of the Cassinian TEM body coil having $N = 16$ elements and optimised for linear-mode operation. The major-axis mode is tuned to the 3T proton frequency (128 MHz), while nearby modes are kept as far from it as possible to avoid potential coupling under loaded conditions. 100
4.3 Current distributions for the two mode 1 resonances (solid lines) and the ideal distributions they seek to approximate (dashed lines). The distribution of the major-axis mode (sinusoidal current distribution) is nearly ideal while that of the unused minor-axis mode is allowed to deviate from the ideal cosinusoidal distribution. 100
4.4 Magnetic field produced by the major-axis mode 1 resonance of the linear TEM body coil. a) field lines and b) field amplitude contours in the positively-rotating frame illustrate the high degree of homogeneity that is obtained. 101
4.5 Resonance spectrum of the Cassinian oval TEM coil having $N = 12$ elements and optimised for quadrature operation. The two mode 1 frequencies are tuned to the 3T proton frequency (128 MHz), while nearby modes that produce inhomogeneous fields are kept as far away as possible to avoid potential coupling under loaded conditions. . . . 103
4.6 Current distributions for the two mode 1 resonances of the quadrature oval TEM coil. The ideal distributions are *not* sinusoidal because the locations of the elements are not the same as those determined previously by conformal mapping. 104
4.7 Field lines of the two mode 1 resonances of the quadrature oval TEM body coil. 105
4.8 Rotating-frame field amplitude contours of the quadrature oval TEM coil. a) indicates the field homogeneity in the positively-rotating frame of reference, while b) is that in the negatively-rotating frame. 106

5.1 Resonance spectrum of a high-pass birdcage coil designed to operate at 200 MHz. The end-ring resonances (not shown) are at 233 MHz. . 111

5.2 Simulated, a), and measured, b), resonance spectra of the circular hybrid birdcage coil prototype designed to operate at 128 MHz. Excellent agreement is observed in the resonant frequencies, especially those of the useful modes of order one. 113

C.1 Magnetic field lines of a current-carrying rod enclosed in a cylindrical shield. Notice that the equivalent line source is not coaxial with the rod but is at a distance f from the rod's axis. The image current is located at a radial distance of $R^2/(c+f)$ from the centre of the shield. 161

C.2 Magnetic field lines of a magnetic dipole enclosed in a cylindrical shield. Such field distributions represent the field produced by the currents induced on a conducting rod in the presence of a field produced by another current inside the shield. 162

List of Symbols and Abbreviations

$\triangleq$	equal by definition
§	section
ALS	Amyotrophic Lateral Sclerosis
B_0, $\mathbf{B_0}$	static magnetic flux density
B_1	radio frequency magnetic flux density
Cho	Choline
CT	Computed Tomography
E	energy
EMF	Electromotive Force
FID	Free Induction Decay
fMRI	functional MRI
G, $\mathbf{G}$	static magnetic flux density gradient
$\hbar$	Plank's constant divided by 2π
H, $\mathcal{H}$	complex magnetic field
H_1, H_2	radio frequency magnetic field amplitude

I	spin quantum number, current intensity
J	spin angular momentum, current density
k	Boltzmann constant, wavenumber
$\mathbf{L}$	inductance-per-unit-length matrix
m	major radius
$\mathbf{M}$	magnetisation vector
MRI	Magnetic Resonance Imaging
MRS	Magnetic Resonance Spectroscopy
n	minor radius
NAA	N-Acetyl Aspartate
NEC	Numerical Electromagnetics Code
(N)MR	(Nuclear) Magnetic Resonance
P	Power, magnetic dipole moment
(P)Cr	(Phospho-) Creatine
PRESS	Point-REsolved SpectroScopy
$\Re$	real part
RF	Radio Frequency
RMS	Root Mean Square
Q	Quality factor

SNR	Signal-to-Noise Ratio
STEAM	Stimulated-Echo Acquisition Mode
$\mathcal{S}_G$	geometric sensitivity
$\mathcal{S}_I$	input sensitivity
T	absolute temperature
T_1	longitudinal relaxation time constant
T_2	transverse relaxation time constant
T_E	echo time
T_R	repetition time
TEM	Transverse ElectroMagnetic
W, $\mathcal{W}$	complex magnetic potential
$\mathbf{Z_0}$	characteristic impedance matrix
γ	magnetogyric ratio, propagation constant
$\mathbf{\Gamma}$	voltage reflection matrix
μ	magnetic permeability, magnetic moment
ω	angular frequency, complex spatial coordinate
ω_0	Larmor angular frequency

Chapter 1

Introduction

The objective of the present work is to enhance the sensitivity of *in-vivo* NMR techniques by providing better RF coupling between the patient and the RF probe (coil). It has been known for some time that an RF probe whose size matches the size of the sample is able to provide better coupling, and therefore better performance, than a probe that is significantly larger than the sample. In recent years, there has been increased interest in further improving the coupling by tailoring the *shape* of the probe to the shape of the body part that is being examined. In fact, while standard probes have a circular access bore, body parts such as the head or torso are considerably oval in cross-section, and therefore there exists the potential for an improvement in coupling to such areas by constructing probes having oval access bores. *In-vivo* NMR techniques can benefit from the consequential improvements in sensitivity and signal quality, even if not necessarily as large as previous advances such as quadrature detection [1], but equally important to the advancement of NMR technology.

Another reason to consider tailored RF coils is to employ them in conjunction with elliptical gradient coils [2] that are designed to minimise stored energy and therefore maximise switching speed. With the reduced minor access dimension of such gradient coils, circular RF coils may not be made large enough to accommodate the patient while allowing entry into the gradient bore. Probes that conform to the elliptical

inner bore of the gradient coil are therefore required.

1.1 Physical Principles of NMR

1.1.1 Nuclear Magnetism

The phenomenon of magnetic resonance is observed when nuclei possessing intrinsic spin $J = \hbar I$, where $I \geq 1/2$ is the spin quantum number, and magnetic moment $\mu = \gamma J$ are placed in an external magnetic field $\mathbf{B_0}$, where $\gamma = \mu/I\hbar$ is the magnetogyric ratio of the nucleus and $\hbar$ is Planck's constant divided by 2π. In a classical description, the torque generated by the external field and the law of conservation of angular momentum result in a precession of the vector $\boldsymbol{\mu}$ about an axis parallel to $\mathbf{B_0}$ according to the equation $\frac{d\boldsymbol{\mu}}{dt} = \gamma\boldsymbol{\mu} \times \mathbf{B_0}$ (c.f. Figure 1.1). The angular (Larmor) frequency of precession is therefore proportional to the field strength, $\boldsymbol{\omega_0} = -\gamma\mathbf{B_0}$. Accounts of the first independent experiments to observe this phenomenon are due to Bloch et al. [3] and Purcell et al. [4] in 1945.

For uncoupled-spin systems such as the abundant water molecule used in anatomical MR imaging, these classical results are consistent with a rigorous quantum-mechanical description [5]. Such details exceed the scope of this work, and we will simply state that in the presence of the $\mathbf{B_0}$ field, an isolated nucleus has $2I + 1$ quantum states, which for many common nuclear species having $I = 1/2$ corresponds to either a parallel or anti-parallel alignment with $\mathbf{B_0}$. The energy separation, E, of these two states (Zeeman splitting) is related to the Larmor frequency by $E = \omega\hbar$ (Figure 1.2), although this separation does not imply the existence of discrete transitions between states. Rather, the nucleus goes from one state to the next through a continuous transition of mixed quantum-mechanical states.

Various biologically important nuclei (c.f. Table 1.1) exhibit magnetic resonance, but the hydrogen nucleus (the proton) is the most commonly used, for imaging as well as spectroscopy (c.f. §1.2.4). This is due to both its high magnetogyric ratio and

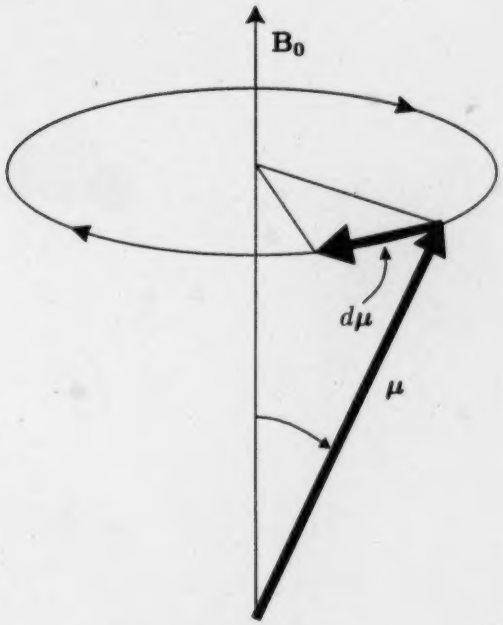

Figure 1.1: Precession of magnetic dipole moment $\boldsymbol{\mu}$ in a magnetic field $\mathbf{B_0}$.

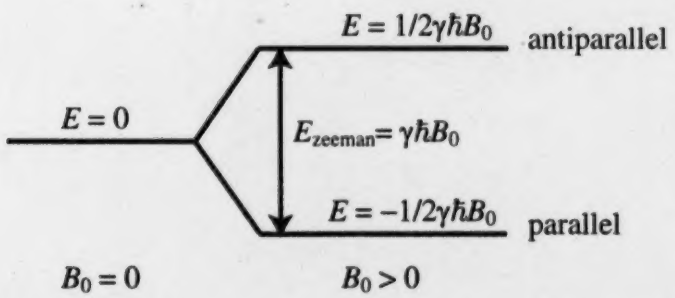

Figure 1.2: Zeeman splitting and eigenstates of a nucleus with spin quantum number $I = 1/2$ in a magnetic field of intensity B_0.

Nucleus	I	γ [10^6 rad/s/T]	Abundance [%]
^{1}H	1/2	267.4	99.9844
^{3}He	1/2	203.7	0.00013
^{13}C	1/2	67.1	1.108
^{19}F	1/2	251.7	100
^{23}Na	3/2	70.8	100
^{31}P	1/2	108.3	100

Table 1.1: Several nuclei that have biological importance along with their spin quantum numbers, magnetogyric ratios and natural abundances [6, p. 66].

to its abundance in tissue as a component of water and other molecules, thus enabling it to induce the largest signals in the receiving coil.

1.1.2 Bulk Magnetisation at Thermal Equilibrium

In a sample containing a macroscopic number of magnetic nuclei, their random orientations result in zero net magnetisation in the absence of an external field, as illustrated in Figure 1.3. In the presence of an external field, their random precessional phases in thermal equilibrium result in a cancellation of the components transverse to the magnetic field, and in a finite net equilibrium magnetisation, $\mathbf{M}$, parallel to $\mathbf{B_0}$. Figure 1.3 illustrates the classical description of this phenomenon, whereby the orientations of the spins are no longer totally random but are, on average, pointed in alignment with the field. Conversely, in the quantum-mechanical description the nuclei populate the two quantum states according to Boltzmann statistics. At an absolute temperature, T (Kelvin), the population of the lower quantum state exceeds that of the higher state by the factor $\frac{\hbar\omega_0}{2kT} = 3.8 \cdot 10^{-12}\omega_0/T$, in the high-temperature approximation, where k is the Boltzmann constant. Consequently, at room temperature the number of nuclei that contribute to the magnetisation is usually very small (a few parts per million), as is the magnetisation that is observed (typical magnetic susceptibilities of paramagnetic materials are also of the order of 10^{-6}). To increase the available magnetisation, the sample can be cryogenically cooled, although this

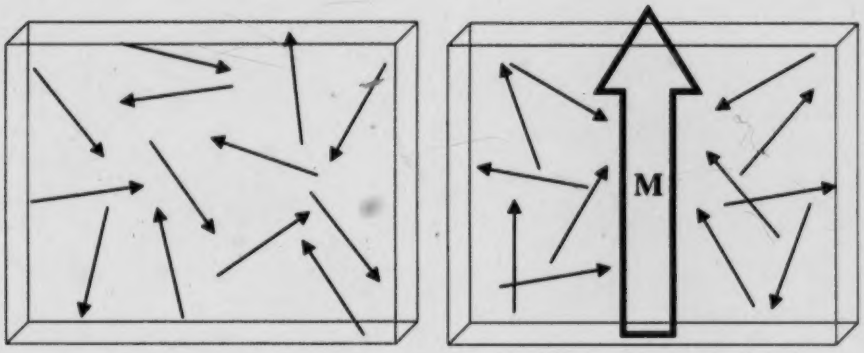

(a) $\mathbf{B_0} = \mathbf{0}$ (b) $\mathbf{B_0} \neq \mathbf{0}$

Figure 1.3: Orientation of individual magnetic moments in a macroscopic sample. a) In the absence of an external polarising field the moments are randomly oriented, while b) in the presence of an external field their average orientation is shifted in the direction parallel to the field to produce an observable magnetisation **M**.

is impossible in *in-vivo* applications. Another technique, applicable to noble gases [7], is to enhance the difference in the number of nuclei in the two states by optical pumping of linked electronic states.

1.1.3 Perturbation and Evolution of the Excited Spin System

If a transverse magnetic field $\mathbf{B_1}$, rotating in the same sense as the nuclear moments and at a frequency close to their precessional frequency, is applied to the spins, the nuclei experience a further torque and **M** can be displaced from the $\mathbf{B_0}$ axis. The angle of displacement (tip angle) depends on the mismatch of the two rotational frequencies and on the amplitude and duration of the excitation pulse. For example, on resonance a pulse of duration $\tau = \pi/2\gamma B_1$ produces a tip angle of 90° and is commonly referred to as a 90° pulse. The trajectory of the magnetisation during the pulse is illustrated in Figure 1.4. Similarly, a 180° pulse has a duration of 2τ, after which the magnetisation is pointing in the $-z$ direction.

From such an excited state, the transverse component of **M** precesses at the Larmor frequency, while the total magnetisation relaxes back to its thermal equilibrium state, usually with an exponential time dependence when the spins are in a liquid such as most biological media. The equation that describes this phenomenon, known as the Bloch equation [8, §III.II], is

$$\frac{d\mathbf{M}}{dt} = \gamma \mathbf{M} \times \mathbf{B_0} - \frac{\mathbf{M_T}}{T_2} - \frac{(M_z - M_{z,0})\hat{\mathbf{z}}}{T_1}, \tag{1.1}$$

where T_1 and T_2 are the characteristic time constants for the longitudinal (M_z) and transverse ($\mathbf{M_T}$) components of the magnetisation, respectively. A typical trajectory of the magnetisation vector during relaxation is shown in Figure 1.5.

The different values of the relaxation time constants are an important source of contrast in anatomical images. If, for example, two regions have T_2's that differ by a factor of 2, as illustrated in Figure 1.6, a maximal difference in amplitudes of the transverse magnetisation in those two regions will occur at a time after the excitation pulse that lies between the two T_2's. Such differences in the relaxation properties of tissue (see Table 1.2) are due to different degrees of interaction between the spins, and between the spins and their magnetic environment. Naturally-occurring differences in relaxation usually create sufficient contrast, but exogenous agents containing paramagnetic ions (e.g., Gd^{+3}) can also be administered to create or exaggerate contrast.

Another source of contrast are the differences in spin density, which alter the *initial* amplitude of the magnetisation. Tissues of different compositions (e.g., soft tissue vs. bone) often have dissimilar spin densities and therefore different initial values of the signal. However, the water content, and hence the spin density, of many soft tissues varies little (see last column of Table 1.2) and therefore it is not as good a source of contrast as the relaxation properties when imaging regions such as the brain or the abdomen.

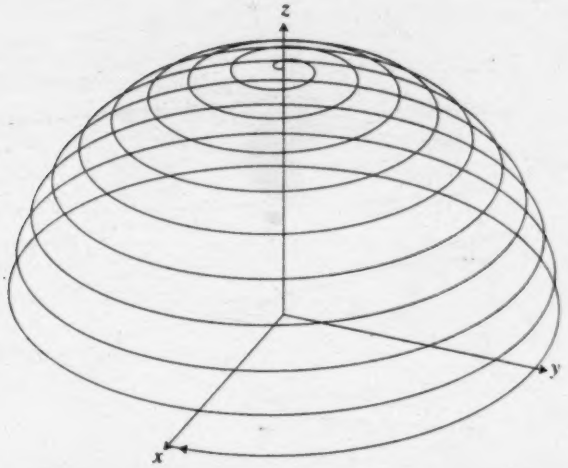

Figure 1.4: Trajectory of the net magnetisation vector **M** in the laboratory frame during a 90° pulse. Notice that the length of the vector is constant during RF excitation if the excitation is short compared with T_1 and T_2.

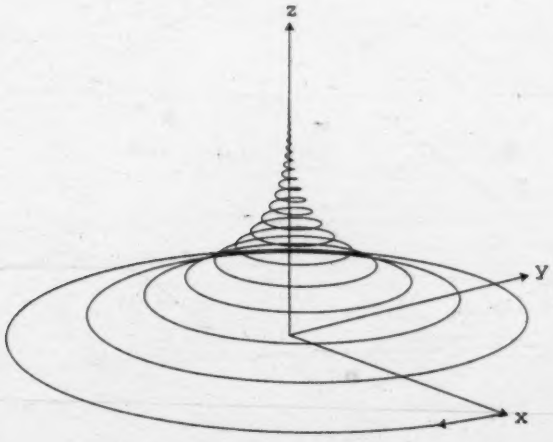

Figure 1.5: Trajectory of the net magnetisation vector in the laboratory frame during free precession with relaxation. Notice that the length of the vector is not constant.

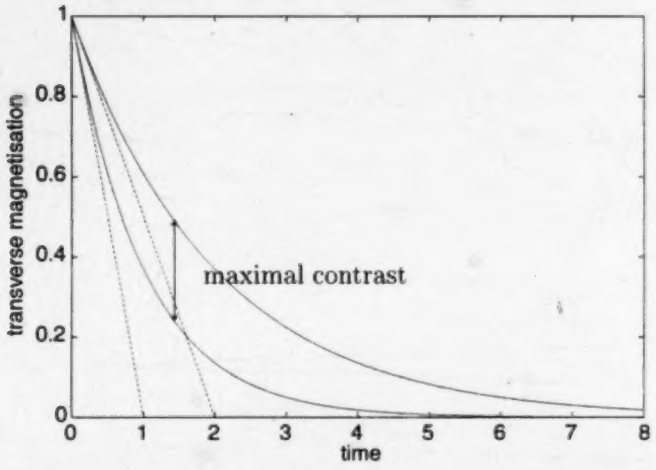

Figure 1.6: Relaxation curves for tissues having T_2's differing by a factor of two. Differences in transverse magnetisation are greatest approximately halfway between the two time constants, shown by extrapolation of the initial slopes (dashed lines).

Tissue	T_1 at 1.5 T [ms]	T_1 at 0.5 T [ms]	T_2 [ms]	water content [%]
Skeletal muscle	870	600	47	79
Liver	490	323	43	63–74
Kidney	650	449	58	71–81
Spleen	780	554	62	72–79
Lung	830	600	79	72–84
Gray matter	920	656	101	84–86
White matter	790	539	92	68–77
Cerebrospinal fluid	>4000	>4000	>3000	99

Table 1.2: Relaxation times [9] for several types of tissue along with their respective water content [10] which is indicative of spin density.

1.1.4 Signal Detection

During free precession, the transverse components of the magnetisation produce a time-varying magnetic field, albeit of very small amplitude. This field can produce a time-varying magnetic flux in a receiver coil (often the same coil used to excite), and therefore by Faraday's law a measurable electromotive force (EMF) is induced [11, §3.1]. This small voltage is subsequently amplified and demodulated using phase-sensitive detectors before being sampled and digitised. Since it is acquired during free precession of the magnetisation as it relaxes back to its equilibrium value, it is often referred to as the free induction decay (FID). The FID from a group of spins having identical Larmor frequencies (an *isochromat*) is shown in Figure 1.7.

To improve the noise performance of the system, two independent and orthogonal receiver coils are utilised, or similarly a single probe having two ports that produce signals that are 90° out of phase. The signals from the two coils or ports are added, amplified and subsequently processed, using *quadrature detection* [12], as the real, or in-phase, and imaginary, or quadrature, channels. Multiple coils are also used to increase the area of coverage and also to improve the SNR in what is termed *phased array* configuration [13]. In this arrangement, the signals from the single receiver coils are processed independently until after the digitisation step, and combined only during the post-processing to produce composite images.

1.1.5 Spatial Encoding Using $\mathbf{B_0}$ Gradients

The acquisition of anatomical information requires that some spatial information be encoded into the nuclear signal. The main $\mathbf{B_0}$ field is usually as uniform as technically possible over the region of interest, therefore in order to differentiate between spins in different spatial locations, three orthogonal gradient fields (i.e., magnetic fields that are parallel to $\mathbf{B_0}$ but vary linearly in amplitude in one direction) are required. In such a field gradient $\mathbf{G}$, the Larmor frequency at point $\mathbf{r}$ will be a function of spatial

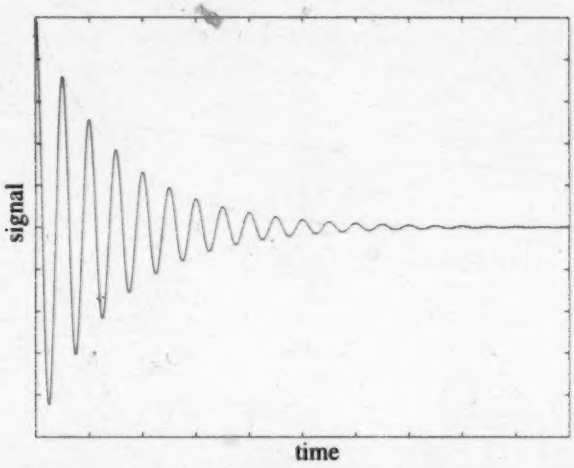

Figure 1.7: Typical time course of the free induction decay (FID), the signal induced in the receiver coil by the precessing magnetisation after a radio frequency excitation. All spins that contribute to this signal are assumed to precess at the same Larmor frequency. The envelope (dashed lines) of the FID represents the amplitude of the transverse component of the magnetisation.

location according to

$$\omega(\mathbf{r}) = \omega_0 + \gamma \mathbf{G} \cdot \mathbf{r}. \tag{1.2}$$

Gradient fields are produced by low-inductance coils in which the time course of the current must be controlled and synchronised precisely with the RF pulses in the sequence. It is supplied by high-current amplifiers that can also produce considerable voltages for fast rise times. With today's gradient coil and amplifier technology, however, the limitation in rise times is often not due to technical limitations, but rather to the induced electric fields which must remain below the threshold for nerve stimulation in order to prevent discomfort to the patient [14].

To provide spatial information, gradient fields can be used in several ways, often in combination, during a pulse sequence.

Selective Excitation

If a gradient of amplitude G is present during a radio frequency excitation of finite bandwidth $\Delta\omega$, only the spins whose Larmor frequencies fall within this bandwidth will be excited. The thickness of the slab of spins that will respond is therefore $\Delta r = \Delta\omega/\gamma G$. This method is also called "slice selection".

Phase Encoding

If the gradient is applied for a brief time Δt during free precession, the difference $\Delta\phi$ in the phases of precession between two points that are at distance $\mathbf{r}$ apart will be $\Delta\phi = \Delta t\gamma\mathbf{G}\cdot\mathbf{r}$. The amplitude of the phase encoding gradient is usually varied during repetitive pulse sequences to impart varying degrees of phase shift to the NMR signal.

Frequency Encoding

Application of a gradient during signal reception will cause the Larmor frequencies of the spins in the sample to be spread according to Eq. (1.2). In order to avoid aliasing, the resulting signal will need to be sampled at least at a frequency of

$$BW = \gamma G \cdot FOV, \tag{1.3}$$

where FOV is the field of view. Subsequently the FID is Fourier transformed to separate its frequency components and to obtain information on the spins at spatial locations along the gradient. This use of a gradient during signal acquisition is also known as the "readout gradient".

1.2 *In-vivo* Applications of NMR

1.2.1 Basic Pulse Sequences

Modern NMR techniques can extract various types of anatomical and/or physiological information from a patient by employing a succession of RF pulses accompanied by

timely switching of the gradient fields. Most are variations of two basic sequences in which the FID is not detected immediately after an RF excitation (as in Figure 1.7), but rather after the precessional phases of spins in different locations have been re-focussed to create an "echo". The time that lapses between the last excitation and the echo (the "echo time", T_E) is often the means by which contrast is created between tissues having different relaxation properties (c.f. 1.1.3).

Spin-Echo

The spin echo was first observed by Erwin Hahn in 1950 [15]. It is based on the property of the 180° pulse to "re-focus" the effects of spatial inhomogeneities in the $\mathbf{B}_0$ field. In fact, the inhomogeneities are responsible for a decrease in the transverse relaxation time constant to a value T_2^* that is less than the intrinsic T_2 of the material. This phenomenon is caused by the dephasing of the single spins which precess at slightly different Larmor frequencies.

If the 180° pulse is applied at a time T_E after the initial 90° excitation pulse, its effect is to invert the accumulated phases of all the spins relative to the central frequency. Consequently, after another interval of duration T_E, all the spins will be in phase once again and a signal maximum will be observed in the receiving coil. The signal's amplitude will not, however, be the same as immediately after the 90° pulse because dephasing due to mechanisms of transverse relaxation such as spin-spin interactions cannot be reversed. Hence the spin-echo sequence provides a means to measure the T_2 even if the magnetic field is not perfectly uniform.

Figure 1.8 is the timing diagram of a spin-echo sequence applied to create an image. Slice selection gradients (G_{ss}) are applied during both RF excitations, and the phase encode gradient (G_{pe}) is varied in a number of steps equal to the number of times the sequence is repeated, from a maximal value to a minimum. The frequency encode gradient (G_{fe}) has the same amplitude during each acquisition of the echo, and is orthogonal to the other gradients. The echoes thus measured are arranged in a

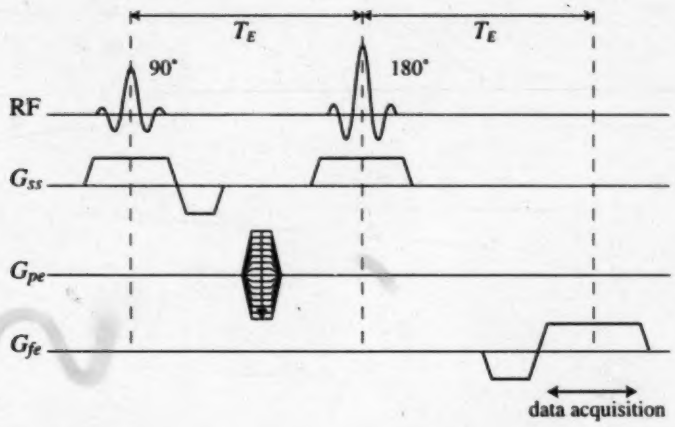

Figure 1.8: Timing diagram for the spin echo imaging sequence. This sequence is repeated several times, each with a different value of the phase encode gradient (G_{pe}).

matrix and Fourier transformed in both dimensions to produce an image of the object. Further details about spin-echo imaging can be found, for example, in reference [16, §7.4].

Gradient-Echo

The gradient-echo sequence (c.f. Figure 1.9) is similar to the spin-echo but it lacks the 180° pulse which is responsible for refocussing the spins but also delivers a relatively large amount of RF energy. Consequently a gradient-echo sequence can be repeated much faster, but it cannot extract true T_2 information. The amplitude of the gradient echo is dependent on the echo time, T_E, by the exponential decay factor $\exp(-T_E/T_2^*)$, where $T_2^* \triangleq (1/T_2 + \gamma\Delta B_0)^{-1}$, the effective decay time constant, is not equal to T_2 as for the spin-echo, but is reduced by the effects of the field inhomogeneity, ΔB_0. Field inhomogeneity significantly accelerates the transverse spin relaxation during the gradient-echo sequence, and therefore T_E needs to be much shorter than for the spin-echo sequence.

As the name implies, the gradient echo is created solely by the frequency encode

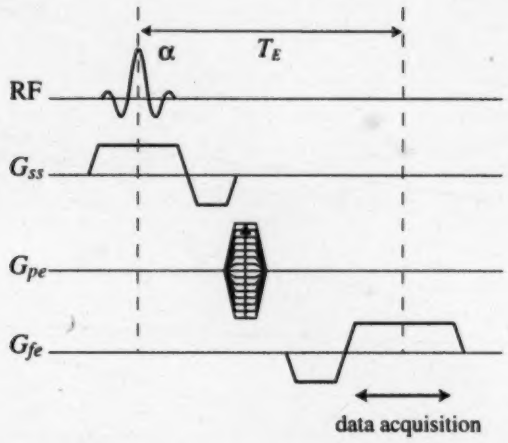

Figure 1.9: The gradient echo imaging sequence.

gradient (G_{fe}), which creates spin dephasing during the negative lobe of the gradient pulse, and immediately refocusses the spins during its positive lobe. Acquired data is processed in the same way as for the spin-echo to produce an image.

1.2.2 Magnetic Resonance Imaging

The most common diagnostic application of NMR is magnetic resonance imaging, MRI. While providing accurate anatomical information, numerous advantages over imaging techniques that utilise ionising radiation (e.g., computed tomography, plain-film X-ray) have contributed greatly to the proliferation of MRI in the clinical setting. The absence of potentially carcinogenic radiation in MRI eliminates the concern for patient and operator safety that is encountered in imaging techniques that use X-rays. Furthermore, contrast in MR images is not limited to tissue (proton) density, but can also be made to depend on one or other of several properties of the environment of the resonant nuclei, e.g., relaxation times (c.f. 1.1.3), diffusion rates, flow, etc. This gives MRI superior contrast resolution of soft tissues, allowing, for example, the discrimination between white and gray matter in the brain, which cannot be achieved using either traditional plain film X-ray or CT.

One advantage that CT and plain film X-ray have enjoyed over MRI is superior spatial resolution which extends well into the sub-millimetre range. The resolution of typical MR images, however, is typically 1 mm or larger, and is directly related to the SNR of the NMR signal [17]. The improvements in RF coupling that are sought by tailoring the RF probe to a particular anatomical region are therefore expected to bring about improvements in the spatial resolution of MRI, helping to make it applicable in situations where the required detail would call for the traditional imaging techniques.

1.2.3 Functional MRI

In addition to anatomical information, NMR is also able to provide physiological information about the patient under study. The ability to map neuronal activity in the brain is one such type of information, and it can be applied to the study of various cognitive functions and disorders. This technique goes under the name of functional MRI (fMRI), and allows the location of changing activity in the brain during sensory stimulation (e.g., light flashes) or voluntary movement (finger tapping) to be determined. It is based on the fact that changes in neuronal activity alter local levels of blood flow and oxygenation, which in turn modify the relaxation properties of the nuclei and the resulting nuclear signal [18]. A large series of images is acquired during alternating periods of activity and inactivity, and statistical techniques are then used to correlate the changing pixel intensities to the activity level. One attractive feature of fMRI is the absence of exogenous contrast agents such as those used in radio-isotope imaging to obtain similar information.

Research using such techniques benefits from the increased sensitivity offered by RF coils with improved coupling to the human head. In fact, the resolution of the resulting images is usually less than optimal because of the great number of image acquisitions that need to be performed over a short time to ensure cooperation of the subject. Hence, improvements in sensitivity obtained by using tailored coils can be

traded off for improvements in resolution and/or faster image acquisition.

1.2.4 Biochemical Analysis

Another important application of NMR is biochemical analysis, accomplished using the technique of magnetic resonance spectroscopy (MRS). The bases of spectroscopy are the phenomena of *chemical shift* and *scalar coupling* which impart unique features on the NMR spectrum of molecules which can be used to identify and quantify the chemical species in a sample. Chemical shift is the result of chemical shielding, the reduction of the total magnetic field experienced by a nucleus due to the effects of the electron cloud around it. Scalar, or J, coupling, on the other hand, is due to the indirect interaction of nuclei in the same molecule through its electronic bonds. The combination of these two phenomena results in a resonance (frequency) spectrum that contains a series of peaks whose relative amplitudes and frequency shifts are unique to each compound, i.e., a fingerprint.

Before the 1980's, MRS was used primarily in the study of small, homogeneous samples of matter in small bore, high field spectrometers. In the past 15 years, however, MRS has been applied *in-vivo*, with the goal of measuring local concentrations of single metabolites in living organisms [19]. Such information is important for the study of localised physiological processes as well as pathological conditions. Ultimately, the resulting concentration maps in anatomical regions such as the brain will be a useful diagnostic tool for numerous pathologies. For example, it is possible to study the concentrations of the neurotransmitters glutamate and N-acetyl aspartate in amyotrophic lateral sclerosis (ALS or Lou Gehrig's disease) patients [20], as well as inositol in bipolar disorder [21].

The technical difficulties associated with in-vivo MRS are due primarily to the small concentrations ($\sim$1–5mM [22]) of metabolites relative to the large amounts of water ($\sim$40M) present in soft tissue. Although the NMR signal from water can be eliminated using multiple quantum filtering techniques [23] or other water suppres-

sion methods, the remaining metabolite signal has still a very low amplitude and any improvement in sensitivity using optimally-coupled coils is greatly advantageous. Besides increasing the visibility of the lower concentration species, this allows for a reduction of the experiment's duration and therefore an improvement in comfort for chronically ill patients, as well as a reduction of the voxel size.

1.3 RF Probe Technology

1.3.1 The Ideal RF Field

The role of the RF probe was introduced in §1.1.3 and 1.1.4 as a device that communicates with the nuclear spins through the RF magnetic field that it generates. Ideally, an RF probe should produce a transverse (relative to $\mathbf{B_0}$), circularly polarised magnetic field of uniform amplitude throughout the useful volume of the coil. Furthermore, some techniques also require that the direction or rotational phase of the magnetic field vector at any particular instant be the same for every point inside the useful volume of the coil. These criteria for field uniformity ensure that nuclear spins at different locations within the coil respond in exactly the same manner to the RF field, and on reception generate signals of the same amplitude and phase. In practice, however, the field is generally elliptically polarised, with uneven spatial distributions of eccentricity, amplitude and phase throughout the volume of the coil. Variations in the phase are normally not as important as variations in field amplitude [24, 25], but they can be a contributing factor to loss of signal by destructive interference [26, 27, §3.1].

Since a time-harmonic field has, in general, elliptical polarisation [28, §1.4.2], it can be decomposed into two counter-rotating circularly polarised fields, where the minor counter-rotating circular component is responsible only for losses (and, reciprocally, for noise on reception) because it does not couple to the nuclear spins. It should therefore be minimised, although in common linearly polarised coil designs such as

surface coils its amplitude is actually *equal* to that of the major component. A probe designed to produce circularly polarised fields is referred to as a *quadrature* coil because usually two orthogonal resonant modes of the probe are excited in quadrature phase. Quadrature excitation and detection can provide up to a factor of 2 savings in power requirements and a factor of $\sqrt{2}$ improvement in SNR over linear excitation and detection [1, 12].

The inevitable electric fields produced by the RF probe are not responsible for any useful interaction and furthermore contribute to power loss in the sample, and, reciprocally, to noise on reception (c.f. §1.3.4). Consequently they should be minimised by careful design of the probe (c.f. §6.1.2, 6.3.4, 6.4.3).

1.3.2 Common Radio Frequency Probe Designs

Radio frequency probes for *in-vivo* applications can be divided into two broad groups, based on their sensitive volumes. Small coils that are used to investigate relatively small regions near the surface of the body are appropriately referred to as surface coils. They are sensitive only within a fraction of the loop diameter along the axial direction [29], although multiple loops may be employed to extend the field of view. Due to their intrinsic field inhomogeneity they are often employed as receivers only, where the small field of view is advantageous in reducing the amount of noise picked up from the patient. In such applications, the transmission pulses are supplied by another coil with a larger field of view and better homogeneity for a more uniform spin response.

To investigate deeper structures, or to provide a uniform excitation in transmission, a so-called volume coil or resonator is required.[1] Most RF volume coil designs are based on the well-known fact that a longitudinal current density, confined to the surface of a circular cylinder of infinite length, and having a sinusoidal dependence

[1] While the terms "coil" and "resonator" describe probes that are structurally quite different, it has become common in the NMR community to use these terms interchangeably to refer to the radio frequency probe.

on the azimuthal coordinate, creates a uniform transverse magnetic field [30, §2.7]. This ideal current density is approximated, to varying degrees, by several designs that have been introduced over the years. The simplest designs involve only two diametrically opposed conductors; two such implementations have been described by Alderman and Grant [31], and by Schneider and Dullenkopf [32], and a quadrature version was described by Sank et al. [33]. Better homogeneity can be achieved using more current-carrying elements, such as the four elements of the "saddle coil" [34], or in general N (usually 12 or 16) circumferentially evenly spaced rungs. Such designs permit quadrature operation by producing currents that have the dependence, in phasor notation, $I_n = I_0 e^{2\pi i n/N}$, where $n = 0, 1, ...(N-1)$ is the circumferential index of the element and i is the imaginary unit. This distribution can be interpreted as a superposition of a sinusoidal current mode and a cosinusoidal current mode that has been phase shifted in time by 90°, resulting in a circularly polarised field. Several such "ladder" coils have been devised; the two most common implementations are explained below, while others such as those of refs. [35, 36] have not reached much widespread popularity.

The Birdcage Resonator

The birdcage resonator employs an LC ladder network to create the correct distribution of currents on the coil's rungs [37]. This resonator produces two degenerate, orthogonal field modes capable of producing very homogeneous transverse fields, which can be superimposed with a 90° electrical phase shift in order to create the desired circularly polarised magnetic field.

A section of the ladder network is shown in Fig. 1.10(a), where the same cell is repeated N times and the two ends of the network are connected (Fig. 1.10(b)), creating a cyclical structure capable of supporting azimuthal standing waves. The frequency for which the total phase shift around the network equals 2π is the frequency of the two modes that are of interest in NMR applications. The rigorous analysis of the

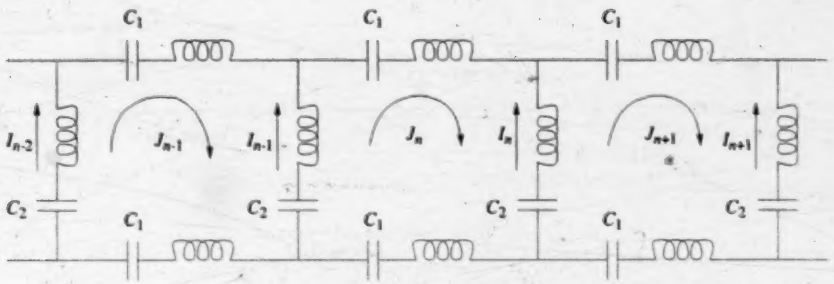

(a) Ladder Network

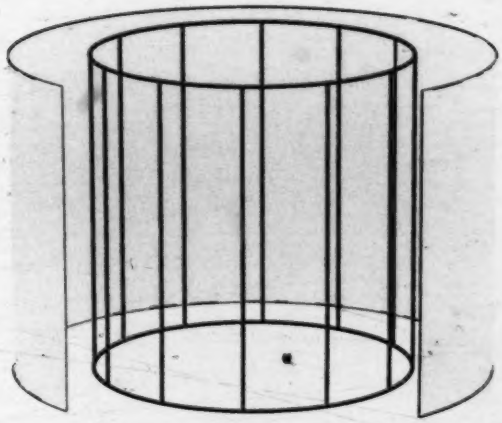

(b) Structure

Figure 1.10: a) A section of birdcage ladder network, which is created by repeating the same cell N times and connecting the ends to create b) a circular structure that is often shielded to prevent interactions with other parts of the NMR scanner. The shield is shown with a sector removed for clarity. The inductors in a) represent the self inductances of the longitudinal conductors and end-ring sections, as well as the mutual couplings between segments that are not orthogonal. Leg currents are related to the mesh currents by $I_n = J_{n+1} - J_n$, $n = 0, 1, ...(N-1)$.

resonant modes of the birdcage coil in the low-frequency limit has been the object of several publications [38, 39, 40, 41]. At high frequencies, when the wavelength becomes comparable to the coil's dimensions, these low-frequency models are no longer valid and wavelength effects such as longitudinal variations of current amplitude and phase lead to field inhomogeneties. Parasitic capacitances also play an increased role at high frequencies and effect coil resonance.

Following the low-frequency treatment by Leifer [41], the circuit equations for the N mesh currents J_n yield the eigenvalue equation

$$\mathbf{M}^{-1}\mathbf{E}\mathbf{J} = \lambda\mathbf{J} \tag{1.4}$$

where the eigenvalues $\lambda = (i\omega)^2$, the ω is the angular frequency, and $\mathbf{J}$ is the column vector whose elements are the mesh currents. The matrices

$$\mathbf{E} = \begin{bmatrix} -2(C_1^{-1}+C_2^{-1}) & C_2^{-1} & 0 & \dots & 0 & C_2^{-1} \\ C_2^{-1} & -2(C_1^{-1}+C_2^{-1}) & C_2^{-1} & 0 & \dots & 0 \\ 0 & C_2^{-1} & \ddots & C_2^{-1} & \dots & 0 \\ \vdots & & & & & \vdots \\ 0 & 0 & \dots & C_2^{-1} & \ddots & C_2^{-1} \\ C_2^{-1} & 0 & 0 & \dots & C_2^{-1} & -2(C_1^{-1}+C_2^{-1}) \end{bmatrix} \tag{1.5a}$$

and

$$\mathbf{M} = \begin{bmatrix} M_0 & M_1 & M_2 & \dots & M_{N-1} \\ M_{N-1} & M_0 & M_1 & \dots & M_{N-2} \\ M_{N-2} & M_{N-1} & M_0 & \dots & M_{N-3} \\ \vdots & & & \ddots & \vdots \\ M_1 & M_2 & \dots & M_{N-1} & M_0 \end{bmatrix}, \tag{1.5b}$$

contain, respectively, the electric (see Fig. 1.10(a)) and magnetic parameters of the network, where $M_n = M_{N-n}, n = 0, 1, \dots N/2$ is the sum of the mesh's self inductance and the mutual inductance with the meshes that are n meshes apart. Because of the linear nature of the birdcage ladder network, both matrices are real and symmetric and therefore the eigenvectors of $\mathbf{M}^{-1}\mathbf{E}$, which correspond to the distribution of

mesh currents of the various modes of resonance, form an orthogonal basis [42, §9.5]. Orthogonality ensures that the modes can be excited independently of each other, even if they resonate at the same frequency.

If the coil is carefully constructed to achieve circular symmetry (i.e., a rotation of $2\pi/N$ does not change the coil), the matrices will also be *circulant*, and the eigenvectors will be the columns of the matrix whose elements are the coefficients of the discrete Fourier transform [43, 44]. Among these N eigenvectors, there will be $N/2-1$ degenerate pairs (i.e., corresponding to the same eigenvalue and spatial frequency), plus one whose elements are all equal (zero spatial frequency) and another whose elements have the same amplitude but alternate in sign ($N/2$ phase rotations for one physical rotation around the coil). Only the two modes having a spatial frequency of one are of interest because they approximate the ideal continuous current distributions.

In addition to the N modes discussed above, the two meshes created by the end-rings give rise to two more modes, the co-rotating current (like the Helmholtz coil [24], [45, §713]) and anti-rotating current (the so-called Maxwell pair) end-ring modes, neither of which produces currents in the coil legs. If C_1 is not present (i.e., in the low-pass configuration), their natural frequency is zero and therefore they can support undesirable eddy currents that decay with an exponential time constant and are induced by the switching of the gradient coils. This effect is eliminated in practice by splitting the end-ring and shorting the gap with a capacitor that has a low impedance at the coil's desired operating frequency, but whose capacitance is low enough to resonate with the inductance of the end ring at a frequency well above the typical frequencies present in the gradient waveforms (tens of kHz). In cases where C_1 is finite, the end-ring modes are normally not useful because they do not produce uniform transverse fields (the Maxwell pair is in fact the basis for z-gradient coils). However, some recent work by Fujita et al. [46, 47] has shown that the Helmholtz mode can be used to produce quadrature coils for "open" NMR systems.

thus avoiding the geometric conflicts that arise in such systems because the patient's axis is *orthogonal* to the vertical $\mathbf{B_0}$ field as opposed to the more common coaxial orientation in solenoidal magnets.

The TEM Resonator

The transverse electromagnetic mode (TEM) resonator evolved from earlier transmission-line resonator designs like Pound and Purcell's coaxial cavity [4]. In the decades that followed, NMR coils were primarily solenoids with some exceptions like Schneider and Dullenkopf's slotted tube resonator [32]. By the late 1980's, however, the major NMR instrument manufacturers were experimenting with novel coil designs for high-field systems and several transmission-line probes were reported [48, 49, 50]. In 1988 Röschmann developed a resonant coil element that did not require discrete capacitors [51], but used tubular capacitors that are adjustable and help to shield the patient from electric fields. Almost simultaneously, a design by Bridges [52] suggested a method of arranging N such elements around a cylinder similarly to the birdcage coil.

The structure of the TEM resonator consists of a cylindrical conducting cavity which is open at least at one end for patient access and inside which are placed N longitudinal conducting rods or strips. These elements are evenly spaced on a cylinder that is coaxial with the cavity and each is connected to the shield through a capacitive load at each end. Figure 1.11(a) illustrates the basic structure of such resonators, and a current commercial implementation can be found in refs. [53, 54].

The resonant behaviour of TEM resonators has been accurately modelled, using the theory of multiconductor transmission lines (see, for example, ref. [55]), by Baertlein et al. [56], from whom the following analysis is abstracted. A note (included in Appendix A) has been submitted for publication to clarify some of their conclusions and illustrate the similarities between the fields produced by a TEM coil and a birdcage coil. In contrast to the model of the birdcage coil introduced in the previous

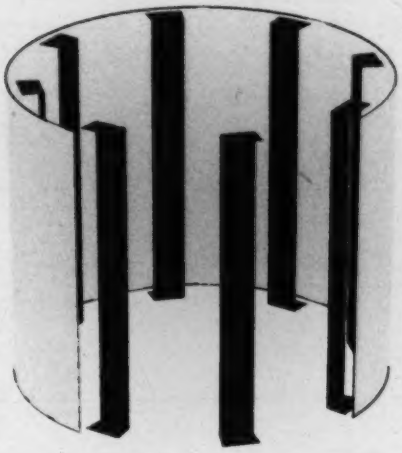

(a) TEM resonator structure

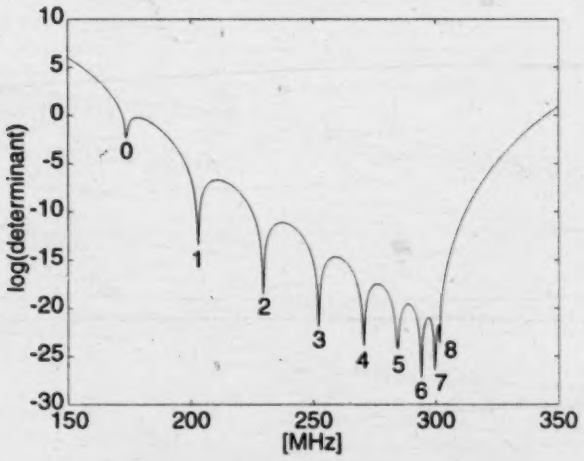

(b) Resonant modes of a 16-element resonator

Figure 1.11: a) Structure of the TEM resonator and b) its resonant modes, labelled according to their spatial frequency. The longitudinal elements may be flat strips, as illustrated, or cylindrical rods. Gaps between the ends of the longitudinal elements and the shield (shown with a sector removed for better viewing) are capacitively loaded.

section, which is valid only if the wavelength is much larger than the dimensions of the coil, multiconductor transmission line theory does not suffer from this limitation and is readily applied to situations where the wavelength is comparable to the dimensions of the structure.

The analysis begins by realising that the TEM resonator can be viewed as a section of transmission line consisting of multiple longitudinal conductors within a circularly cylindrical shield. The fundamental propagation modes of this line have both transverse electric and magnetic fields, as implied by the TEM acronym. Higher order modes are not considered in this analysis, as experimental evidence shows that they play only a minor role in the resonant behaviour of the TEM coil. This transmission line is terminated at both ends with reactive loads and therefore is able to support standing waves in its interior. The objective is to determine the frequency of resonance and respective current patterns on the longitudinal conductors.

We define $\mathbf{Z} = \mathbf{R} + i\omega\mathbf{L}$ and $\mathbf{Y} = \mathbf{G} + i\omega\mathbf{C}$ to be the impedance and admittance matrices per unit length of the transmission line, where the matrices on the right of the equal signs have the usual meanings of resistance, inductance, conductance and capacitance per unit length, respectively. For all the matrices, the elements off the diagonal indicate mutual quantities and the elements on the diagonal refer to self quantities. An initial simplification is to consider the line to be lossless, thus eliminating the resistance, $\mathbf{R}$, and conductance, $\mathbf{G}$, matrices that in practice account for losses in the conductors and biological sample, respectively. Derivation of the Helmholtz equation for such a system of coupled transmission lines yields the product $\mathbf{YZ}$, whose eigenvalues are the squares of the propagation constants. Under the assumption of TEM fields, and in the case of an empty coil, the constants must all be equal to the free-space propagation constant, $\gamma = i\omega/c$. Consequently, the capacitance and inductance matrices will be related by $c^2\mathbf{LC} = \mathbf{1}_N$, where $\mathbf{1}_N$ is the identity matrix of order N, and c is the speed of light in a vacuum. Thus only one of the matrices $\mathbf{L}$ or $\mathbf{C}$ will need to be determined.

While the propagation constants do not enable us to identify any differences in the modes of propagation of the line that can be used to produce the desired current distribution, the *characteristic* impedance or admittance matrix does. These matrices relate the amplitudes of the voltages $\mathbf{V}^{\pm}$ and currents $\mathbf{I}^{\pm}$ on the line, where the signs indicate a wave propagating in the positive or negative direction, respectively. The characteristic admittance matrix $\mathbf{Y}_0$ is defined by

$$\mathbf{I}^{+} = \mathbf{Y}_0\mathbf{V}^{+} \text{ and } \mathbf{I}^{-} = -\mathbf{Y}_0\mathbf{V}^{-}, \tag{1.6a}$$

and, equivalently, the characteristic impedance, $\mathbf{Z}_0 = \mathbf{Y}_0^{-1}$, by

$$\mathbf{V}^{+} = \mathbf{Z}_0\mathbf{I}^{+} \text{ and } \mathbf{V}^{-} = \mathbf{Z}_0\mathbf{I}^{-}. \tag{1.6b}$$

We now introduce a transformation matrix, $\mathbf{T}$, that will diagonalise $\mathbf{Z}_0$. Since we have assumed that the line is lossless and that the medium is linear, $\mathbf{Z}_0$ will be real and symmetric, therefore $\mathbf{T}$ will be orthogonal. This new basis will be called the *modal* basis, with modal quantities indicated with a subscript m, because the eigenvectors represent patterns of current and voltage that propagate with a scalar characteristic impedance (i.e., currents and voltages have the same distribution on the elements). Given that $\mathbf{Z}_0 = \gamma^{-1}\mathbf{Z}$, the modal characteristic impedance becomes

$$\mathbf{Z}_{0,m} = c\mathbf{T}^{-1}\mathbf{L}\mathbf{T}, \tag{1.7}$$

and therefore the modal basis is that which diagonalises the inductance matrix.

If each element is connected at both ends to the shield by equal capacitive loads whose admittances are the elements of the diagonal load matrix $\mathbf{Y}_L$, the modal voltage reflection matrices at the ends become

$$\mathbf{\Gamma}_m = (\mathbf{1}_N - \mathbf{Z}_{0,m}\mathbf{Y}_{L,m})(\mathbf{1}_N + \mathbf{Z}_{0,m}\mathbf{Y}_{L,m})^{-1}, \tag{1.8}$$

where $\mathbf{Y}_{L,m} = \mathbf{T}^{-1}\mathbf{Y}_L\mathbf{T}$ is the load or termination admittance matrix in modal coordinates. The condition for resonance is that a wave that is reflected, and travels

the length l of the line twice, return to the starting point in phase and with minimal attenuation, i.e., the determinant

$$\left|\mathbf{1}_N - \mathbf{\Gamma}_m^2 e^{-2i\omega l/c}\right| \tag{1.9}$$

is at a minimum as a function of $\omega = 2\pi f$.

In contrast to the lumped-element model of the birdcage coil presented in the previous section, Eq. (1.9) has an infinite number of solutions, a consequence of having used a model with distributed parameters. Normally, however, only the modes having frequencies less than the line's resonant frequency if it were shorted at both ends ($f_0 = c/2l$) are considered. Modes of higher frequency would have large longitudinal variations of current amplitude resulting in axially inhomogeneous fields.

A TEM coil constructed with perfect symmetry will have a circulant inductance matrix [43, 44] and, with the above restriction in frequency, $N/2 - 1$ pairs of degenerate modes, plus one whose currents are all equal and one whose currents are equal in amplitude but alternate in phase. Again, only the two modes that have a (co)sinusoidal current distribution are used in NMR applications.

A plot of a typical resonance spectrum of a TEM coil simulated using the above method is shown in Fig. 1.11(b), where the modes are labelled according to their spatial frequency (1/2 the number of sign changes in the currents on the elements for one rotation). The two useful modes are degenerate and correspond to the second dip from the left.

1.3.3 High-Frequency Effects on Field Homogeneity

The uniform RF field described in §1.3.1 is most easily produced when propagation delays along the largest dimensions of the coil and sample volume can be neglected. Typically this translates into dimensions of one tenth of a wavelength or less, taking care to account for the wavelength-shortening effects of the high permittivity of water in biological samples. These wavelength effects are the predominant cause of the field

focussing effect [27] which creates regions of high $\mathbf{B_1}$ field where there is constructive interference (typically at the centre of the sample) and low field where the interference is destructive (at the edges). This effect cannot be totally eliminated because it is due largely to the sample itself, but it can be manipulated to provide high sensitivity to interior regions by placing flexible bags filled with water around the sample or patient in order to position the sensitivity peak where it is required (e.g., in a particular lobe of the brain) [25, 57].

Another cause of field inhomogeneity is the finite resistivity of biological media, which leads to the skin effect, a decay in field amplitude as depth inside the patient increases. This effect therefore tends to counter the field focussing effect. Twenty years ago it was believed that proton imaging would not be possible above frequencies of 10 MHz because of the skin effect calculated for a model of a homogeneous phantom [58]. Subsequent technical innovations [27] and anatomically-accurate modelling [59], however, have proven the contrary and today in-vivo proton NMR is possible at frequencies well above 200 MHz. The fact that the human body is highly heterogeneous may explain why the effects of field focussing and skin depth are not as evident as they are in homogeneous phantoms at the same frequency.

At high frequencies even empty coils exhibit field inhomogeneities due to propagation effects. In the ladder coils of the previous section the current distribution along any single leg is not constant but tapers off at the ends, leading to a reduction in magnetic field strength at the top and bottom openings of the coil (c.f. Chapter 5). One method to mitigate this effect is to capacitively shorten the legs [50].

1.3.4 The Signal-to-Noise Ratio in the NMR Experiment

All measurement techniques are subject to measurement errors, or noise, and NMR is no exception. While careful construction and shielding are commonly used to decouple the system from external sources of electrical noise such as radio broadcasts and telecommunications equipment, noise can also originate in all stages of a signal

acquisition system, including the detection, amplification and processing stages.

In a properly designed system, however, it is the radio frequency probe that determines the available signal-to-noise ratio (SNR) [17]. The probe is therefore a critical component of the NMR system because in in-vivo NMR experiments, noise is generated by the thermal excitation of charge carriers within the body as well as in the coil itself. Although cooling to reduce sample-noise amplitude is impossible in in-vivo applications, cryogenic probes have been utilised [60, 61] in particular applications.

Strategies are also available to maximise the signal amplitude. For example, most NMR probes are actually resonant circuits tuned to the Larmor frequency of interest to produce the largest possible signals. Increases in signal amplitude can also be obtained by taking advantage of the quadratic dependence of signal amplitude on the amplitude of the static $\mathbf{B_0}$ field [62]. The drawbacks associated with this solution are the high cost of high-field, superconducting, whole body magnets, in addition to the difficulty of producing homogeneous, circularly polarised (CP) RF magnetic fields when the RF wavelength becomes comparable to the dimensions of the coil and anatomical region. Furthermore, high frequencies and large differences in dielectric constant between air and human flesh give rise to dielectric resonance and field focussing, [27] which are best avoided because of their contribution to field inhomogeneity and to the damaging effects of tissue heating [63, 64, 59] brought about by localised intense electric fields. Currently, field strengths above 3 Tesla are considered experimental only, and the highest field strength of a whole-body system is 8 Tesla [65].

Enhancements in signal are also possible through careful sequence design and optimisation of its parameters, but ultimately it is the reception quality of the RF probe that determines SNR. The reception properties of any NMR probe are related to its transmission properties and to its circuit parameters which are readily measured on the workbench. In fact, as seen from its ports, and at frequencies near the resonant frequency, any resonator may be modelled by an equivalent LC network such as that

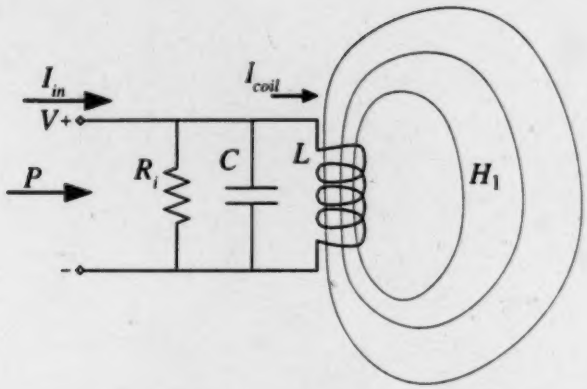

Figure 1.12: Equivalent circuit for an NMR probe exhibiting parallel resonant characteristics.

of Figure 1.12, or in some cases its series-resonant counterpart [66]. To describe the ability of a coil to produce the desired magnetic field H_1 at a given point, we define the geometric sensitivity,

$$\mathcal{S}_G \triangleq \frac{H_1}{I_{coil}}, \tag{1.10a}$$

and the input sensitivity,

$$\mathcal{S}_I \triangleq \frac{H_1}{\sqrt{P}}, \tag{1.10b}$$

where I_{coil} is the peak current flowing in the part of the coil that produces the useful field, and P is the real power input at the coil terminals. Bear in mind that in general I_{coil} is not equal to the current in the inductive portion of the equivalent circuit, and in coils with complex topologies I_{coil} is not defined uniquely. We also need to define the current gain,

$$\alpha \triangleq \frac{I_{coil}}{I_{in}}, \tag{1.10c}$$

which is a function of coil topology as well as the matching circuitry that is required to connect the coil to the amplifier and/or receiver portions of the NMR system.

We may now follow references [67, 68] and apply Faraday's law of magnetic induction and the principle of reciprocity to obtain an expression for the signal amplitude

due to a point source M of magnetic moment. The voltage at the terminals is therefore

$$V_s = \omega_0 \mu \alpha \mathcal{S}_G M, \tag{1.11}$$

where μ is the magnetic permeability and if M is a magnetic moment per unit volume (A/m/ml) V_s will be in V/ml.

The amplitude of the noise is described by the standard deviation, σ_n, of the noise voltage, and if all sources other than thermal noise can be neglected it is given by [69]

$$\sigma_n = \sqrt{4kTR_t\Delta f}, \tag{1.12}$$

where k is Boltzmann's constant, T is the absolute temperature, R_t is the resistance seen at the coil's inputs and Δf is the receiver bandwidth.

Taking the ratio of the previous expressions we obtain the signal-to-noise ratio (SNR),

$$\Psi \triangleq \frac{V_s}{\sigma_n} = \frac{\omega_0 \mu \alpha \mathcal{S}_G M}{\sqrt{4kTR_t\Delta f}}, \tag{1.13}$$

which is maximal with respect to the coil parameters α, $\mathcal{S}_G$ and R_t when the input sensitivity,

$$\mathcal{S}_I = \frac{\sqrt{2}\alpha \mathcal{S}_G}{\sqrt{R_t}}, \tag{1.14}$$

is maximal. This relationship is obtained from Eqs. (1.10) and $P = \frac{1}{2}|I_{in}|^2 R_t$ at resonance. It should also be emphasised that enhancements of α by using a lossless transformer, for example, are counterbalanced by a change in input resistance R_t and therefore bring no net benefit. Conversely, it also means that impedance matching the coil using low-loss components can be accomplished without degrading the available SNR.

1.3.5 Improvements in Signal-to-Noise Ratio from Anatomical Tailoring of RF Coils

Improvements in SNR are possible by enabling a closer coupling between the coil and the sample, thereby improving the geometric sensitivity defined in Eq. (1.10a). In

small solenoidal coils, this is often expressed as an increase in filling factor (the ratio of magnetic energy stored in the sample to the total RF magnetic energy), and has long been known to bring about an increase in SNR [8, §III.IV.B]. For coils used in in-vivo applications (c.f. §1.3.2), although analytical expressions for the sensitivity are not always available, similar results can be expected. This can be explained qualitatively by noticing that closer-coupling coils require less current to produce a given field amplitude. If coil losses remain unchanged (this assumption is plausible if there is a minor deformation from the circular cross section) an increase in SNR results. Thus, coils having tailored geometry are expected to be more efficient than coils with the standard circular cross section which need to be larger than the corresponding anatomy to accommodate most parts of the human body. This property forms the basis for the work illustrated in this thesis.

Bibliography

[1] C.-N. Chen, David I. Hoult, and V.J. Sank. Quadrature coils: A further $\sqrt{2}$ improvement in sensitivity. *Journal of Magnetic Resonance*, 54:324–327, 1983.

[2] Qin Liu, D.G. Hughes, and Peter S. Allen. Improved, minimum-inductance, elliptic-cylinder z-gradient coil using axial and azimuthal current flow. *Journal of Magnetic Resonance, Series B*, 113:228–235, 1996.

[3] F. Bloch, W.W. Hansen, and M. Packard. The nuclear induction experiment. *Physical Review*, 70:474–485, 1946.

[4] E.M. Purcell, H.C. Torrey, and R.V. Pound. Resonance absorption by nuclear magnetic moments in a solid. *Physical Review*, 69:37, 1946.

[5] C.P. Slichter. *Principles of Magnetic Resonance*. Springer-Verlag, New York, third edition, 1989.

[6] *The Bruker Almanac*, 1995.

[7] Hans-Ulrich Kauczor, Michael Ebert, Karl-Friedrich Kreitner, Helge Nilgens, Reinhard Surkau, Werner Heil, Dirk Hofmann, Ernst W. Otten, and Manfred Thelen. Imaging of the lungs using ^{3}He MRI: Preliminary clinical experience in 18 patients with and without lung disease. *Journal of Magnetic Resonance Imaging*, 7:538–543, 1997.

[8] A. Abragam. *The Principles of Nuclear Magnetism*. Clarendon Press, Oxford, 1961.

[9] Michael J. Bronskill and Simon J. Graham. NMR characteristics of tissue. In Michael J. Bronskill and Perry Sprawls, editors, *The Physics of MRI: 1992 AAPM Summer School Proceedings*, pages 32–55. American Institute of Physics, Woodbury, NY, 1993.

[10] Paula T. Beall, Sharad R. Amtey, and Sitapati R. Kasturi. *NMR Data Handbook for Biomedical Applications*. Pergamon Press, New York, 1984.

[11] S. Ramo, J.R. Whinnery, and T. Van Duzer. *Fields and Waves in Communication Electronics*. John Wiley, New York, third edition, 1994.

[12] David I. Hoult, C.-N. Chen, and V.J. Sank. Quadrature detection in the laboratory frame. *Magnetic Resonance in Medicine*, 1:339–353, 1984.

[13] P.B. Roemer, W.A. Edelstein, Cecil E. Hayes, S.P. Souza, and O.M. Mueller. The NMR phased array. *Magnetic Resonance in Medicine*, 16:192–225, 1990.

[14] D.J. Schaefer, J.D. Bourland, and J.A. Nyenhuis. Review of patient safety in time-varying gradient fields. *Journal of Magnetic Resonance Imaging*, 12:20–29, 2000.

[15] Erwin L. Hahn. Spin echoes. *Physical Review*, 80:580–594, 1950.

[16] Zhi-Pei Liang and Paul C. Lauterbur. *Priciples of Magnetic Resonance Imaging: A Signal Processing Perspective*. IEEE Press Series on Biomedical Engineering. IEEE Press, 2000.

[17] W.A. Edelstein, G.H. Glover, C.J. Hardy, and R.W. Redington. The intrinsic signal-to-noise ratio in NMR imaging. *Magnetic Resonance in Medicine*, 3:604–618, 1986.

[18] S. Ogawa, T.-M. Lee, A.S. Nayak, and P. Glynn. Oxygenation-sensitive contrast in magnetic resonance image of rodent brain at high magnetic fields. *Magnetic Resonance in Medicine*, 14:68–78, 1990.

[19] Jens Frahm, Klaus-Dietmar Merboldt, and Wolfgang Hänicke. Localized proton spectroscopy using stimulated echoes. *Journal of Magnetic Resonance*, 72:502–508, 1987.

[20] V.A. Cwik, C.C. Hanstock, P.S. Allen, and W.R.W. Martin. Estimation of brain-stem neuronal loss in amyotrophic lateral sclerosis with in-vivo proton magnetic resonance spectroscopy. *Neurology*, 50:72–77, 1998.

[21] Peter H. Silverstone, Susan Rotzinger, Andrew Pubkhovsky, and Christopher C. Hanstock. Effects of lithium and amphetamine on inositol metabolism in human brain as measured by ^{1}H and ^{31}P MRS. *Biological Psychiatry*, 46(12):1634–41, 1999.

[22] Varanavasi Govindaraju, Karl Young, and Andrew A. Maudsley. Proton NMR chemical shifts and coupling constants for brain metabolites. *NMR in Biomedicine*, 13:129–153, 2000.

[23] Richard B. Thompson. *Coupled Proton MRS: In-Vivo Applications*. PhD thesis, University of Alberta, 1999.

[24] John F. Schenck. Radiofrequency coils: Types and characteristics. In Michael J. Bronskill and Perry Sprawls, editors, *The Physics of MRI: 1992 AAPM Summer School Proceedings*, pages 98–134. American Institute of Physics, Woodbury, NY, 1993.

[25] David C. Alsop, Thomas J. Connick, and Gabor Mizsei. A spiral volume coil for improved RF field homogeneity at high static magnetic field strength. *Magnetic Resonance in Medicine*, 40:49–54, 1998.

[26] David I. Hoult. The NMR receiver: A description and analysis of design. *Progress in NMR Spectroscopy*, 12:41–77, 1978.

[27] David I. Hoult. Sensitivity and power deposition in a high-field imaging experiment. *Journal of Magnetic Resonance Imaging*, 12:46–67, 2000.

[28] Max Born and Emil Wolf. *Principles of Optics*. Cambridge University Press, Cambridge, UK, seventh edition, 1999.

[29] J.R. Keltner, J.W. Carlson, M.S. Roos, S.T.S. Wong, T.L. Wong, and T.F. Budinger. Electromagnetic fields of surface coil *in vivo* NMR at high frequencies. *Magnetic Resonance in Medicine*, 22:467–480, 1991.

[30] Jianming Jin. *Electromagnetic Analysis and Design in Magnetic Resonance Imaging*. CRC Press, New York, 1999.

[31] D.W. Alderman and D.M. Grant. An efficient decoupler coil design which reduces heating in conductive samples in superconducting spectrometers. *Journal of Magnetic Resonance*, 36:447–451, 1979.

[32] H.J. Schneider and P. Dullenkopf. Slotted tube resonator: A new NMR probe head at high observing frequencies. *Review of Scientific Instruments*, 48:68–73, 1977.

[33] V.J. Sank, C.-N. Chen, and David I. Hoult. A quadrature coil for the adult human head. *Journal of Magnetic Resonance*, 96:236–242, 1986.

[34] D.M. Ginsberg and M.J. Melchner. Optimum geometry of saddle shaped coils for generating a uniform magnetic field. *Review of Scientific Instruments*, 41:122, 1970.

[35] Waldo S. Hinshaw and Robert C. Gauss. Distributed phase RF coil. U.S. Patent 4439733, March 1984.

[36] A. Sotgiu, G. Gualtieri, and R. Passariello. Highly homogeneous circularly polarized RF field for whole body NMR imaging. *Magnetic Resonance Imaging*, 6:249–254, 1988.

[37] C.E. Hayes, W.A. Edelstein, J.F. Schenck, O.M. Mueller, and M. Eash. An efficient, highly homogeneous radiofrequency coil for whole-body NMR imaging at 1.5T. *Journal of Magnetic Resonance*, 63:622–628, 1985.

[38] Peter M. Joseph and Dongfeng Lu. A technique for double resonant operation of birdcage imaging coils. *IEEE Transactions on Medical Imaging*, 8(3):286–294, September 1989.

[39] James Tropp. The theory of the bird-cage resonator. *Journal of Magnetic Resonance*, 82:51–62, 1989.

[40] Michael D. Harpen. Harmonic structure of cylindrical imaging coils. *Medical Physics*, 17(4):686–690, Jul/Aug 1990.

[41] Mark C. Leifer. Resonant modes of the birdcage coil. *Magnetic Resonance in Medicine*, 124:51–60, 1997.

[42] Richard Bronson. *Matrix Methods: An Introduction.* Academic Press, Inc., New York, New York, 1970.

[43] Louis A. Pipes. Circulant matrices and the theory of symmetrical components. *The Matrix and Tensor Quarterly*, pages 35–50, December 1966.

[44] Philip J. Davis. *Circulant Matrices*. Chelsea Publishing, New York, second edition, 1994.

[45] James Clerk Maxwell. *A Treatise on Electricity & Magnetism*. Dover, New York, third edition, 1954.

[46] Hiroyuki Fujita, William O. Braum, and Michael A. Morich. Novel quadrature birdcage coil for a vertical B_0 field open MRI system. *Magnetic Resonance in Medicine*, 44:633–640, 2000.

[47] Hiroyuki Fujita, William O. Braum, and Gordon D. DeMeester. Open-face quadrature "birdcage" head coil. In *Proceedings of the International Society for Magnetic Resonance in Medicine, Ninth Annual Meeting*, page 14, April 2001.

[48] Norbert Krause. High-frequency field system for nuclear magnetic resonance. U.S. Patent 4506224, Mar. 19 1985.

[49] H. Bomsdorf, T. Helzel, D. Kunz, P. Röschmann, O. Tschendel, and J. Wieland. Spectroscopy and imaging with a 4 tesla whole-body MR system. *NMR in Biomedicine*, 1(3):151–158, 1988.

[50] H. Barfuss, H. Fischer, D. Hentschel, R. Ladebeck, A. Oppelt, R. Wittig, W. Duerr, and R. Oppelt. In vivo magnetic resonance imaging and spectroscopy of humans with a 4T whole-body magnet. *NMR in Biomedicine*, 3(1):31–45, 1990.

[51] Peter Röschmann. High-frequency coil system for a magnetic resonance imaging apparatus. U.S. Patent 4746866, May 1988.

[52] James F. Bridges. Cavity resonator with improved magnetic field uniformity for high frequency operation and reduced dielectric heating in NMR imaging devices. U.S. Patent 4751464, June 1988.

[53] John Thomas Vaughan Jr. Radio frequency volume coils for imaging and spectroscopy. U.S. Patent 5557247, Sept. 17 1996.

[54] John Thomas Vaughan Jr. Radio frequency volume coils for imaging and spectroscopy. U.S. Patent 5886596, Mar. 23 1999.

[55] J.A. Brandão Faria. *Multiconductor Transmission-Line Structures: Modal Analysis Techniques.* John Wiley & Sons, Inc., New York, NY, 1993.

[56] Brian A. Baertlein, Ö. Özbay, T. Ibrahim, R. Lee, Y. Yu, A. Kangarlu, and P.-M. L. Robitaille. Theoretical model for an MRI radio frequency resonator. *IEEE Transactions on Biomedical Engineering*, 47(4):535–546, 2000.

[57] Qing X. Yang, Michael B. Smith, Haiying Liu, Xiaoliang Zhang, Jinghua Wang, Kamil Ugurbil, and Wei Chen. Manipulation of signal intensity distribution with dielectric loading at 7.0T. In *Proceedings of the ISMRM/ESMRMB, Joint Annual Meeting*, page 1096, 2001.

[58] David I. Hoult and Paul C. Lauterbur. The sensitivity of the zeugmatographic experiment involving human samples. *Journal of Magnetic Resonance*, 34:425–433, 1979.

[59] Christopher M. Collins. *Calculations of RF Magnetic Fields and SAR Experienced by the Human Body During MRI.* PhD thesis, University of Pennsylvania, 1999.

[60] Michael Jerosch-Herold and Randall K. Kirschman. Potential benefits of a cryogenically cooled NMR probe for room-temperature samples. *Journal of Magnetic Resonance*, 85:141–146, 1989.

[61] Markus Vester, Florian Steinmeyer, Bernhard Roas, Günther Thummes, and Kai Klundt. High-temperature superconducting surface coils with liquid nitrogen or pulse tube refrigeration. In *Proceedings of the ISMRM 5th Annual Meeting*, volume 3, page 1528, 1997.

[62] David I. Hoult and R.E. Richards. The signal-to-noise ratio of the nuclear magnetic resonance experiment. *Journal of Magnetic Resonance*, 24:71–85, 1976.

[63] John M. Osepchuk and Ronald C. Petersen. Safety standards for exposure to RF electromagnetic fields. *IEEE Microwave Magazine*, 2(2):57–69, June 2001.

[64] Christopher M. Collins and Michael B. Smith. Calculations of B_1 distribution, SNR, and SAR for a surface coil adjacent to an anatomically-accurate human body model. *Magnetic Resonance in Medicine*, 45:692–699, 2001.

[65] P.-M.L. Robitaille, A.M. Abduljalil, A. Kangarlu, X. Zhang, Y. Yu, R. Burgess, S. Bair, P. Noa, L. Yang, Hui Zhu, B. Palmer, Z. Jiang, D.M. Chakeres, and D. Spigos. Human magnetic resonance imaging at 8 T. *NMR in Biomedicine*, 11(6):263–265, October 1998.

[66] Axel Haase, Florian Odoj, Markus Von Kienlin, Jan Warnking, Florian Fidler, Alexander Weisser, Mathias Nittka, Eberhard Rommel, Titus Lanz, Bernhard Kalusche, and Mark Griswold. NMR probeheads for *in vivo* applications. *Concepts in Magnetic Resonance*, 12(6):361–388, 2000.

[67] Hubert Vesselle and Robert É. Collin. The signal-to-noise ratio of nuclear magnetic resonance surface coils and application to a lossy dielectric cylinder model Part I: Theory. *IEEE Transactions on Biomedical Engineering*, 42(5):497–506, May 1995.

[68] Ogan Ocali and Ergin Atalar. Ultimate intrinsic signal-to-noise ratio in MRI. *Magnetic Resonance in Medicine*, 39:462–473, 1998.

[69] J.B. Johnson. Thermal agitation of electric charge in conductors. *Physical Review*, 32:97–109, 1934.

Chapter 2

Elliptical Birdcage Coils[1]

2.1 Introduction

Because sections of the human anatomy are not always circular in cross section, improvements in radio frequency (RF) coil performance can be sought by tailoring coil shape to that of a specific body part, thus improving the geometric match. One such non-circular cross section is the ellipse, to which numerous approaches have been applied to determine first the conductor placement that optimizes field homogeneity (for both linear and quadrature excitations) and secondly the capacitance values required for resonance at a given frequency [2, 3, 4, 5, 6, 7]. In the practical implementation of the birdcage coil, however, it is often desirable to use a conductive shield to limit both the interaction with other parts of the NMR system and the far-field radiation. In the case of the circular-section coil, the shield is usually a coaxial circular cylinder having any diameter larger than that of the coil former. For non-circular cylinders it is, however, necessary to identify the shield cross-section, appropriate to that of the former, that will give the best field homogeneity in quadrature operation. In the case of elliptical-section coils, two reports, one using an approximate method [6], and the other using numerical methods [7], have already suggested that optimal homogeneity is achieved by using a continuous shield constructed on a cylinder whose

[1] A version of this chapter has been accepted for publication in *Magnetic Resonance in Medicine* [1].

cross section is any ellipse that is larger than and *confocal* with the elliptical coil former. Nevertheless, another report [4], which included the effects of propagation and non-uniform current distribution on flat ribbon conductors, arrived at a conflicting conclusion, namely that the distance between coil and shield should be as uniform as possible. The apparent conflict most likely arises because the individually isolated shield elements, introduced to minimize gradient-switching eddy currents, give rise to a different shield current distribution from that of a continuous shield, and hence a different effect on the homogeneity. By applying conformal mapping to calculate the fields produced by a confocally-shielded elliptical birdcage, the analytical framework presented in this chapter provides a formal proof of the relationship between the elliptical coil and its shield to produce optimal homogeneity. It goes further by also evaluating the *geometric sensitivities* (c.f. §2.3.1) of the two orthogonal field modes as simple algebraic functions of the coil and shield dimensions. This enables the *input* sensitivity of a loaded elliptical coil to be estimated and compared with that of other coils having similar dimensions, thereby providing a guide to potential improvements in coil performance before a detailed numerical simulation is undertaken. Knowledge of the mismatch in sensitivity between the two modes is also essential for the prospective design of an appropriate feed system that will produce the desired circular polarisation. The methods presented here are equally applicable to other resonator designs, such as the TEM coil [8], that operate by creating longitudinal currents on a cylindrical surface. A preliminary account of this work was presented at the 7th annual meeting of the ISMRM, 1999 [9].

2.2 Mathematical Analysis

The analysis of the fields produced by the shielded elliptical coil system is greatly simplified by exploiting the circular geometry as a template from which to derive some important relationships between the coil and shield currents. The representation of the shielded, circular birdcage so obtained is then applied to the elliptical geometry

using conformal mapping tools [10]. These tools, while allowing one to maintain the use of analytic functions, also maintain the implicit assumptions of the original birdcage design, namely, two-dimensional geometry and quasi-static fields. While the neglect of the end-ring currents and of the comparable dimensions of the coil to the wavelength are not entirely realistic, these overall assumptions facilitate a predictive mathematical model based on the discrete approximation of a sinusoidal current distribution on the surface of a cylinder. The predictions of that model can be more finely tuned using numerical methods accomodating specific operating conditions.

The first step in this analysis is to recall [11] that a Laplacian field (in this case magnetic, in a current-free region) can be represented, using a two-dimensional complex notation, by a complex function $H(w) = H_y + iH_x$, where $w = x + iy$ is the complex spatial coordinate. The x and y components of the field are exchanged, compared to w, in order to ensure that H be an *analytic* function [10]. It is, moreover, always possible to define a complex representation of the potential, $W(w)$, whose derivative gives the field, i.e., $H = \frac{d}{dw}W$, and where the constant amplitude contours of its real part (the z component of the magnetic vector potential) will give the field lines [11, 12, §4.10]. For example, the complex magnetic field produced by a filamentary current of infinite length, flowing parallel to the z-axis, having intensity I and intersecting the xy plane at the location w_0, can be written, in SI units, as

$$H(w) = \frac{I}{2\pi(w - w_0)}. \tag{2.1}$$

Its complex potential (except for an additive constant) is therefore

$$W(w) = \frac{I}{2\pi}\log(w - w_0). \tag{2.2}$$

2.2.1 The Circular Birdcage Coil (Discrete Implementation)

Assuming the medium to be linear, the field resulting from multiple current elements, such as the elements of a birdcage coil, can be obtained simply by superposition [12].

For a circular-section birdcage coil having radius r and N elements of small cross section, the linear horizontal-mode field is

$$H(w) = \frac{I_0}{2\pi} \sum_{n=0}^{N-1} \frac{\sin\theta_n}{w - re^{i\theta_n}}, \tag{2.3}$$

where $\theta_n = 2\pi\frac{n}{N}$, $n = 0, 1, ...(N-1)$ are the angular positions of the elements, I_0 is the maximum amplitude of the linear-mode currents, and where each element carries a current that is proportional to the *sine* of its angular position. The analogous expression for the vertical mode is obtained by changing the angular dependence to a *cosine* distribution. At the center of the coil ($w = 0$), this summation can be evaluated easily by referring to tables of known sums [13], and both modes result in a field having an amplitude

$$H_1 = \frac{I_0 N}{4\pi r}. \tag{2.4}$$

If this coil is now shielded using an ideal cylindrical conducting surface of radius R, coaxial with the coil former, the method of images [14] may be applied to calculate the resulting field. Each element of the birdcage coil will produce an image current of equal but opposite intensity, located on a third (virtual) coaxial cylinder of radius R^2/r. The field at the origin due to the effects of real and image currents now has an amplitude,

$$H_1 = \frac{I_0 N}{4\pi}\left(\frac{1}{r} - \frac{r}{R^2}\right). \tag{2.5}$$

By rearranging the field equation we obtain the coil's *geometric sensitivity*, $\mathcal{S}_G$, defined as the field at the origin produced by mode currents of unit amplitude (c.f. eq. (1.10a)). Note that this definition does not anticipate the effects of losses in the coil and/or sample (discussed in §2.3.1) but expresses a strictly geometric relationship between coil currents and field amplitude. For an unshielded coil it is given by

$$\mathcal{S}_G = \frac{H_1}{I_0} = \frac{N}{4\pi r}, \tag{2.6}$$

but when the coil is shielded it decreases by a factor $\left(1 - \frac{r^2}{R^2}\right)$. A sample field-line

plot is shown in Figure 2.1(a) to illustrate the homogeneity of the field in the central region of a shielded coil and the boundary conditions that the shield imposes.

2.2.2 Circular Birdcage (Continuous Current Distribution)

Analysis of the idealised circular birdcage coil allows us to infer some important relationships between the coil currents and the shield currents that will be shown to be correspondingly valid for the elliptical geometry. This idealisation is obtained by letting the number of birdcage elements, N, tend to infinity, leading to a surface current density, J, around the coil former. For uniform transverse fields of amplitude H_1 within the cylinder, the current densities have their familiar expressions [15]

$$J_{sin}^{coil}(\theta) = 2H_1 \sin\theta \tag{2.7a}$$

$$J_{cos}^{coil}(\theta) = 2H_1 \cos\theta, \tag{2.7b}$$

for horizontal or vertical polarisation, respectively. Equations (2.7) also emphasize the equivalence of the dimensions of the surface current density and the field that it produces, namely, A/m, therby enabling H_1 to be used as representative of the amplitude of the field or of the amplitude of the current density.

The presence of a coaxial conducting shield can again be accounted for using the method of images. By applying it to each infinitesimal current element, the resulting image current density, on the virtual cylinder of radius R^2/r, will be

$$J_{sin}^{image}(\theta) = -2H_1 \frac{r^2}{R^2} \sin\theta \tag{2.8a}$$

$$J_{cos}^{image}(\theta) = -2H_1 \frac{r^2}{R^2} \cos\theta. \tag{2.8b}$$

By analogy with Eq. (2.3), the resulting field distribution can then be expressed as an integration over all infinitesimal line current elements on the first and virtual cylinders,

$$H(w) = \frac{1}{2\pi} \int_0^{2\pi} \frac{J^{coil}(\theta) r}{w - re^{i\theta}} d\theta - \frac{1}{2\pi} \int_0^{2\pi} \frac{J^{image}(\theta) \frac{R^2}{r}}{w - \frac{R^2}{r} e^{i\theta}} d\theta. \tag{2.9}$$

These difficult integrals need not be evaluated directly, however. In fact, the complex potentials arising from the current densities of Eq. (2.7) may be inferred directly from reference [11, §4.03]. In [11, §4.03], an equation is given (Eq. (11)) that represents the (scalar) electric potential outside a perfectly conducting cylinder that has been placed perpendicular to a uniform electric field directed along the x axis. To obtain a complex potential, its imaginary part can be obtained uniquely, except for an arbitrary constant, by direct application of the Cauchy-Riemann equations [10], or by inspection by realising that $r\cos\theta = \Re\{re^{i\theta}\}$. The resulting complex potential coincides with the complex potential of a uniform magnetic field directed along the y axis in which a cylinder having permeability μ has been placed. However, the resulting expression retains a contribution from the original uniform polarising field of reference [11, §4.03] (the linear term), that must be subtracted to leave those terms due solely to the currents induced on the surface of the cylinder. The orthogonal magnetic field orientation can be obtained in a similar manner by rotating the spatial coordinate w by $-90°$ with the substitution $w \to iw$. The resulting potentials, in the two source-free regions bounded by the coil former, therefore follow

$$W_{sin}^{coil}(w) = \begin{cases} -iH_1\frac{r^2}{w} & |w| > r \\ iH_1 w & |w| < r \end{cases} \tag{2.10a}$$

for the horizontal mode, and

$$W_{cos}^{coil}(w) = \begin{cases} -H_1\frac{r^2}{w} & |w| > r \\ -H_1 w & |w| < r \end{cases} \tag{2.10b}$$

for the vertical mode. Analogous relations, accounting for the effects of the shield, hold for the potentials due to the current densities expressed in Eq. (2.8).

By superimposing the effects of the current densities flowing on the coil and on the virtual cylinder ($|w| = R^2/r$) it may be shown that the boundary conditions of zero normal magnetic field and a tangetial component of magnetic field that equals the conduction current density are satified at the shield ($|w| = R$), which is assumed to be ideal. The tangential boundary condition also allows us to verify that the current

density induced on the shield has the same expression as Eq. (2.8), i.e.,

$$J^{shield}(\theta) = J^{image}(\theta). \tag{2.11}$$

The effects of coil and shield currents can now be combined in the three distinct regions delineated by the two circles that correspond to coil and shield. Within the circular region inside the coil former ($|w| < r$) the complex potential reflects the perfectly uniform resultant field obtained by superposition. Both modes have an amplitude $H_1(1 - \frac{r^2}{R^2})$, as indicated by the potentials

$$W_{sin}(w) = iH_1\left(1 - \frac{r^2}{R^2}\right)w \tag{2.12a}$$

$$W_{cos}(w) = -H_1\left(1 - \frac{r^2}{R^2}\right)w. \tag{2.12b}$$

The cancelling effects of the shield currents on the field's amplitude are accounted for by the term in brackets, which is the same as that in Eq. (2.5). Within the annular region between the coil and shield ($r < |w| < R$) the potential can be written as

$$W_{sin}(w) = -iH_1r^2\left(\frac{w}{R^2} + \frac{1}{w}\right) \tag{2.13a}$$

$$W_{cos}(w) = H_1r^2\left(\frac{w}{R^2} - \frac{1}{w}\right) \tag{2.13b}$$

whereas in the rest of the plane outside the shield ($R < |w|$), the contributions of the two current distributions cancel exactly, thus demostrating the ideal nature of the shield. A complete field line plot (equally spaced contours of the real part of W) is shown in Figure 2.1(b), in juxtaposition with the more realizable field in Fig. 2.1(a) which seeks to approximate it.

2.2.3 Conformal Transformations

Conformal transformations, and their equivalent complex analytic representation, have the ability to transform one Laplacian field into another Laplacian field. In previous designs of *unshielded* elliptical birdcage coils, one such transformation (Eq. (7)

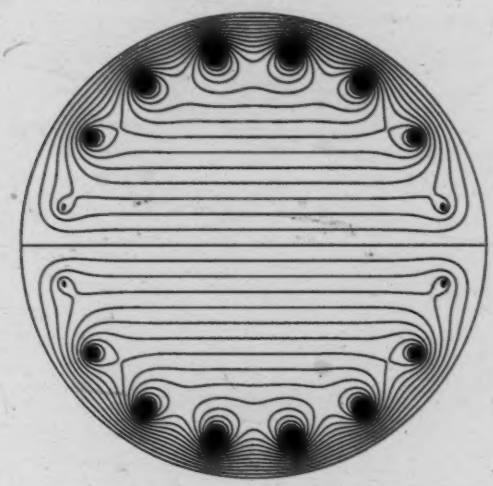

(a) Discrete Implementation

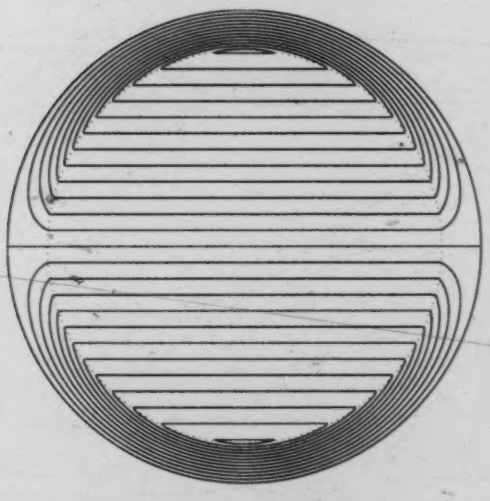

(b) Continuous Idealisation

Figure 2.1: Transverse magnetic field lines (quasi-static approximation) produced by shielded circular coils a) in a realistic implementation such as a birdcage coil or TEM coil with 16 elements and b) the ideal field which it seeks to approximate.

of reference [6]) allows the results that are available for the circular coil to be mapped into the modal current densities for the ellipse. This transformation (sometimes known as the Zhukovskii or airfoil transform) can be applied directly to the discrete current element *locations* on a circular birdcage to obtain their new locations on the elliptical coil. In relation to the analysis presented here, that transformation can also be applied to the potentials that are obtained as an intermediate step in the calculation of Eqs. (2.10), before subtracting the uniform polarising field. The fundamental property of this transformation is that it must map the region *outside* the circle, where the field is known, into the region *outside* the ellipse, where it is not known.

Letting b be the radius of the circle and $a < 2b$ be one half the focal distance of the ellipse, the Zhukovskii transformation is given by the analytic function

$$w' = f(w) = w + \frac{a^2}{4w} \tag{2.14}$$

where w' is the new complex spatial coordinate. The semi-major and semi-minor axes of the ellipse, m and n, respectively, are related to b and a by

$$m = b + \frac{a^2}{4b} \tag{2.15a}$$

$$n = b - \frac{a^2}{4b} \tag{2.15b}$$

2.2.4 The Elliptical Birdcage Coil (Continuous Current Distribution)

In contrast to the case of the circle, the method of images cannot be used directly when dealing with an elliptical shield because a filamentary source will produce a filamentary image only if the shield is a plane or a circular cylinder. However, it *is* possible to use the complex potential in a similar manner to that employed for the circle to solve for the fields in a confocal elliptical coil/shield system. To do this, one needs to recognise that the inner elliptical surface, $\mathcal{E}_1$, can be defined as the image of a circle of radius b_1, centered at the origin, through the conformal transformation of

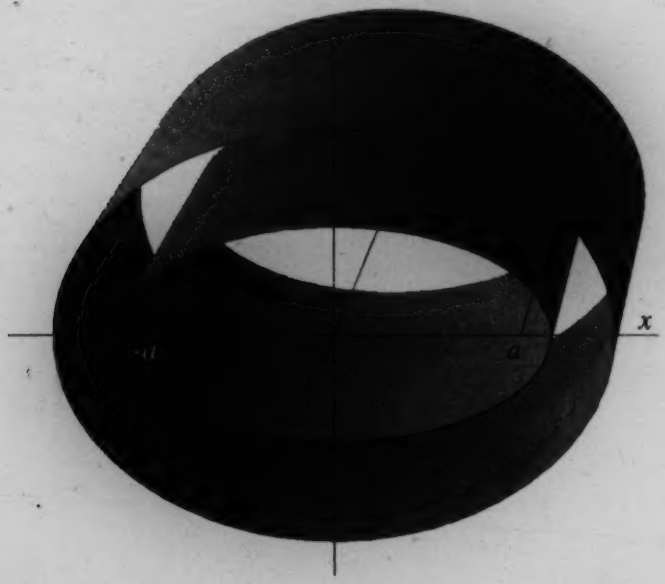

Figure 2.2: An illustration of the geometry of a confocally-shielded elliptical coil having an axial ratio appropriate, for example, for coupling to the pelvic region. The birdcage ladder network is constructed on an elliptically cylindrical surface $\mathcal{E}_1$, while the RF shield is on $\mathcal{E}_2$. The lines $x = \pm a$ are the foci of both cylinders.

Eq. (2.14). A confocal elliptical surface, $\mathcal{E}_2$, on which the shield is to be constructed, may also be defined in the same way by mapping a circle of radius $b_2 > b_1$. This elliptical coil geometry is illustrated in Figure 2.2.

The transformation of Eq. (2.14) can also be used to determine the complex potential of the current-density distribution flowing on $\mathcal{E}_1$ (that was calculated in reference [6]) to generate a uniform magnetic field in the interior of $\mathcal{E}_1$ in the absence of a shield. The potentials in this unshielded case are obtained by adapting the results of reference [11, §4.261], in an manner analogous to that used to derive Eqs. (2.10). This results in a potential

$$\mathcal{W}_{sin}^{coil}(w') = \begin{cases} iH_1^{sin}\left(\frac{1}{2} - 2\frac{b_1^2}{a^2}\right)\left[w' - \sqrt{w'^2 - a^2}\right] & \text{outside} \\ iH_1^{sin}w' & \text{inside} \end{cases} \tag{2.16a}$$

for the horizontal mode, and

$$\mathcal{W}_{cos}^{coil}(w') = \begin{cases} -H_1^{cos}(\frac{1}{2} + 2\frac{b_1^2}{a^2})\left[w' - \sqrt{w'^2 - a^2}\right] & \text{outside} \\ -H_1^{cos} w' & \text{inside} \end{cases} \tag{2.16b}$$

for the vertical mode, where *inside* and *outside* refer to the location of w' with respect to the ellipse, and where the amplitudes of the excitation of the coil's two modes (represented by field amplitudes H_1^{sin} and H_1^{cos}) may, in general, be unequal.

In the case of the confocally-shielded elliptical coil, it is appropriate to assume for the moment, by analogy with the circular case, that the currents induced on the shield will themselves produce uniform fields within the shield, while outside cancelling the field that induced them. If this assumption be true, then the potentials for the shielding currents would have the same expressions as Eqs. (2.16), with b_1 substituted by b_2 and $H_1^{sin,cos}$ replaced by the shield field amplitudes $H_2^{sin,cos}$. It is therefore necessary to solve for the amplitudes, $H_2^{sin,cos}$, representing the shielding current densities, that will give rise to field cancellation outside the shield. Assuming an equal excitation of both modes, i.e.,

$$H_1^{sin} = H_1^{cos} = H_1, \tag{2.17}$$

the amplitudes giving rise to cancellation,

$$H_2^{sin} = -H_1 \frac{1 - 4b_1^2/a^2}{1 - 4b_2^2/a^2}, \qquad \text{horizontal mode,} \tag{2.18a}$$

$$H_2^{cos} = -H_1 \frac{1 + 4b_1^2/a^2}{1 + 4b_2^2/a^2}, \qquad \text{vertical mode,} \tag{2.18b}$$

are independent of w', confirming that the assumed shield current densities and potentials were correct and that the two fields do indeed cancel completely outside the shield. For this cancellation to occur, the two fields must have the same "shape" outside $\mathcal{E}_2$, i.e., they must be equal except for the multiplicative constants represented by the fractional terms in Eqs. (2.18). If the shield and coil former are not confocal, this exact cancellation cannot occur with the assumed shield current density. In the

non-confocal case, a second conformal transformation would be required to determine the field distribution. Some results for shield shapes other than the confocal ellipse are presented in references [5, 7].

The final expressions for the potentials are given below and the complete field line plots are shown in Fig. 2.3. Specifically, between $\mathcal{E}_1$ and $\mathcal{E}_2$ we have,

$$\mathcal{W}_{sin}(w') = iH_1\left(\frac{2b_1^2}{a^2} - \frac{1}{2}\right)\left[w'\frac{a^2/4 + b_2^2}{a^2/4 - b_2^2} - \sqrt{w'^2 - a^2}\right] \tag{2.19a}$$

$$\mathcal{W}_{cos}(w') = H_1\left(\frac{2b_1^2}{a^2} + \frac{1}{2}\right)\left[w'\frac{a^2/4 - b_2^2}{a^2/4 + b_2^2} + \sqrt{w'^2 - a^2}\right], \tag{2.19b}$$

where the magnetic field boundary conditions are again fully satisfied at the shield. Inside $\mathcal{E}_1$, in agreement with the simulations of reference [7], the field retains perfect uniformity, as indicated by the potential's linear dependence on w',

$$\mathcal{W}_{sin}(w') = iH_1 w'\frac{b_2^2 - b_1^2}{b_2^2 - a^2/4} \tag{2.20a}$$

$$\mathcal{W}_{cos}(w') = -H_1 w'\frac{b_2^2 - b_1^2}{b_2^2 + a^2/4}. \tag{2.20b}$$

The fractional terms on the right-hand side account for the partial cancelling effects of the shield currents on the field amplitude, and are analogous to the bracketed term in Eq. (2.5).

It is important to notice that under the assumption of equal modal excitation (Eq. (2.17)) the resulting field amplitudes (derivable from Eqs. (2.20)) are no longer the same for each mode, contrary to the unshielded case obtained by letting $b_2 \to \infty$. To see how to accommodate the difference in modal field amplitudes, it is appropriate to introduce a new definition of geometric sensitivity, $\mathcal{S}'_G$, for distributed currents, that is analogous to the discrete-case definition (see eq. (1.10a)). For $\mathcal{S}'_G$ the field amplitude within the coil former is divided by the field amplitude, H_1, that would have been produced in absence of a shield. The new sensitivity definition leads to a dimensionless quantity for distributed currents, in contrast to the discrete-case definition which has the dimensions of $length^{-1}$. Nevertheless, it is subsequently

possible to obtain an expression for the relative sensitivity, ξ, which simplifies to the ratio of the semi-axes (m_2, n_2) of the shield, irrespective of the axial ratio of the coil former, so long as that former is a confocal ellipse, i.e.,

$$\xi = \frac{\mathcal{S}'_{G\sin}}{\mathcal{S}'_{G\cos}} = \frac{b_2^2 + a^2/4}{b_2^2 - a^2/4} = \frac{m_2}{n_2} > 1. \tag{2.21}$$

This is a new result and it can be intuitively understood by comparing the proximity of coil and shield at the locations where the current density is maximal. For example, stronger field cancellation takes place near the major axis where shield and coil are closest, thereby causing the minor-axis mode to be weaker. Consequently, to produce a circularly polarised field within $\mathcal{E}_1$, the modes must not only be driven in quadrature, but the different geometric sensitivities need to be compensated by producing unequal excitations, satisfying the condition

$$H_1^{\cos} = \xi H_1^{\sin}. \tag{2.22}$$

Finally, it may be tempting to interpret the result in Eq. (2.21) as though the field lines of a shielded elliptical coil were obtained from those of a circular coil simply by stretching one dimension. However, even though within $\mathcal{E}_1$ the resulting uniform fields have amplitudes that would indeed differ by the axial ratio of the shield, the two ellipses produced by such a stretch would not be confocal, and, more importantly, the fields between coil and shield would no longer satisfy the Laplace equation.

2.2.5 Elliptical Birdcage (Discrete Implementation)

To extend these relationships to a birdcage coil comprising N discrete elements, we first take advantage of prior work. In the *unshielded* case, it was previously shown [6] that the best approximation to the continuous current density could be obtained using the same excitation currents as in the circular birdcage coil (c.f. §2.2.1), but only if the discrete elements were placed at the precise locations on the elliptical former obtained from mapping the (equispaced) element locations of the circular birdcage

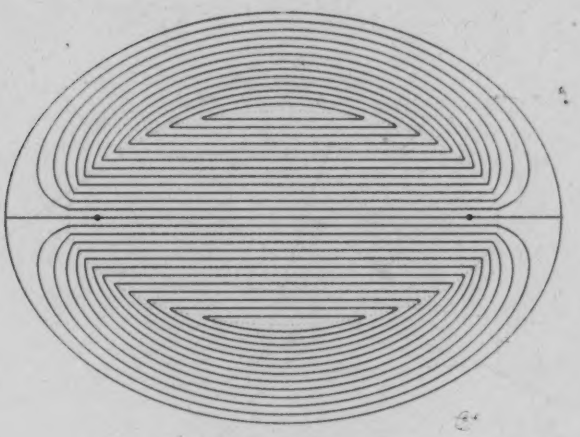

(a) Horizontal Mode

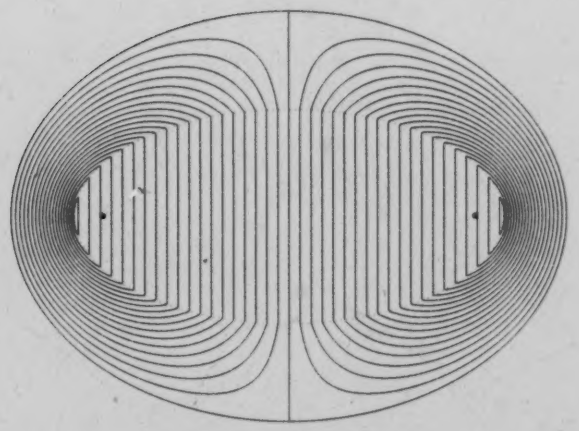

(b) Vertical Mode

Figure 2.3: Magnetic field lines of a) the major-axis and b) the minor-axis field modes of an idealised shielded elliptical coil wherein the inner ellipse is carrying an ideal continuous current density [6]. The outer ellipse is seen to be an ideal shield that limits the RF coil's interaction with the rest of the NMR system, while preserving the ideal field homogeneity achievable without a shield. The difference in field amplitude between the two field orientations is due to the different geometric sensitivity of the two modes.

coil, using the transformation of Eq. (2.14). To obtain fields of amplitude H_1 whose potentials approximate Eqs. (2.16) in the absence of a shield, the maximum amplitude of the excitation currents is obtained by solving for the radius b in Eqs. (2.15) and substituting it for r in Eq. (2.4). After rearranging terms, one obtains

$$I_0 = 2(m_1 + n_1)H_1\frac{\pi}{N}, \tag{2.23}$$

where m_1 and n_1 are the major and minor semi-axes of $\mathcal{E}_1$. The π/N factor of this expression differs from the sinusoidal dependence originally reported in ref. [6], which was derived by approximating the effect of a discrete element by an integral over a larger continuous-current segment. In consequence, it gives results that are numerically more accurate for low values of N.

The practical issue now is to obtain expressions similar to Eq. (2.23) relating current intensity to field amplitude for each of the two modes of the *shielded* discrete elliptical coil. Since the direct application of the method of images (as done in §2.2.1) is not possible with an elliptical shield, the computation of the exact field lines, and hence the degree of inhomogeneity produced by such a coil, would involve a second conformal mapping to determine the distortion of the single element fields due to the presence of the shield. This extension is omitted for brevity, and is not actually required in order to determine the sensitivities. In fact, if the coil elements in the shielded case are positioned in the same manner and are driven by the same excitation currents as in the *unshielded* case, the sensitivities will be obtainable directly from Eqs. (2.20) and (2.23). By analogy with the circular geometry (Eq. (2.6)), the sensitivities of the shielded and unshielded elliptical coils must differ only by a "shielding factor" that is independent of N up to, and including, the continuous current density limit. The shielding factors corresponding to each of the two orthogonal linear modes of excitation of the continuous elliptical coil can therefore be extracted directly from Eq. (2.20), and used to augment the left hand side of Eq. (2.23).

The expression for the relative sensitivity (Eq. (2.21)) will, of course, remain unchanged, and this may be verified by comparing its predictions with the simulations

presented in reference [7], where the relative sensitivity of a 16-element shielded elliptical coil was computed numerically. For a confocal shield having an axial ratio of 34.2cm/26.8cm=1.276, (c.f. Eq. (2.21)) the numerical amplitudes of the two modes were found [7] to be in a ratio of 1:1.274. The difference (0.2%) is of the same order as the error produced by rounding off the shield's dimensions.

2.3 Results and Practical Considerations

2.3.1 Comparison of Circular and Elliptical Birdcage Coils

The geometric sensitivities of the circular and elliptical shielded coils in their two linear excitation modes can finally be summarised as follows,

$$\mathcal{S}_G^{circ} = \frac{N}{4\pi}\left(\frac{1}{r} - \frac{r}{R^2}\right) \tag{2.24a}$$

$$\mathcal{S}_{Gsin,cos}^{ellip} = \frac{N}{2\pi(m_1 + n_1)}\left(\frac{b_2^2 - b_1^2}{b_2^2 \mp a^2/4}\right), \tag{2.24b}$$

where the $-$ $(+)$ sign is taken for the major (minor) axis field mode excitation. We can use these equations to predict the undamped performance of a shielded elliptical coil relative to a shielded circular coil having the same number of elements and whose circular cylinders have the same diameters as the major diameters of the two corresponding ellipses.

Quantitative comparisons of two examples are provided in Table 2.1, where we have chosen elliptical coils with relative dimensions appropriate for the human head (axial ratio of 1.27 : 1) and appropriate for the thoracic or pelvic region (axial ratio of 2 : 1). As expected, the higher the axial ratio of the elliptical coil and shield, the more pronounced is the improvement in geometric sensitivity, and the greater is the mismatch in the sensitivity of the coil's two modes.

Table 2.1 also contrasts the undamped performance of shielded and unshielded coils, where it can be seen that the presence of a shield actually *enhances* the improvement in geometric sensitivity obtainable by using an elliptical coil section. This

Coil section	Sensitivity normalized to circular			Axial Ratio	
	Unshielded coil	Shielded coil		Coil	Shield
Head	1.12	1.44 (hor.) 1.22 (vert.)	1.33 (mean)	1.27	1.18
Body	1.33	2.17 (hor.) 1.61 (vert.)	1.89 (mean)	2	1.35

Table 2.1: Geometric sensitivities of elliptical birdcage coils appropriate for the head (major access diameter $2m_1 = 28$ cm, minor access diameter $2n_1 = 22$ cm) and the body ($2m_1 = 55$ cm, $2n_1 = 27.5$ cm) relative to those of corresponding circular coils having the same diameter as the major diameter of the ellipse. In the shielded case, the diameters of the shields are $2m_2 = 33$ cm and $2n_2 = 28$ cm for the head coil, and $2m_2 = 71$ cm and $2n_2 = 52.5$ cm for the body coil. Again the diameter of the corresponding circular shield is taken equal to the major diameter of the ellipse. For the shielded elliptical coils the improvements in sensitivity for the single modes are tabulated separately, together with their average, which corresponds to the improvement expected in reception when an ideal 90° phase shift is performed on one channel before summation with the other. The ratio of the modal sensitivities is equal to the axial ratio of the shield, as predicted by Eq. (2.21).

property can be qualitatively explained by comparing the proximity of the coil elements to the shield around the circular and elliptical circumferences. Most of the elliptical coil's elements are indeed farther from the shield than are the circular coil's elements, therefore the elliptical shield is responsible for less field cancellation than a circular shield that has the same diameter as the major diameter of the elliptical shield.

2.3.2 Coil Loading and Signal-to-Noise

In order to derive practical usefulness from relations (2.24), we must also include the effects of loss mechanisms that combine to give the resistive component, R_{in} of the coil's input impedance. Such damping is responsible for power deposition during transmission as well as for the generation of noise during signal reception. A detailed discussion of the signal-to-noise ratio (SNR) of the *in-vivo* experiment is found in references [16, 17, 18, 19]. For the loaded coil, it was explained [17] that maximizing

the SNR was equivalent to maximizing an input sensitivity, $\mathcal{S}_I$ (defined in eq. (1.10b)), where $P = 1/2R_{in}|I_{in}|^2$ is the real power fed by the input current I_{in} at resonance to produce a field, H_1, which in turn can be evaluated from the length of a 90° pulse. The measured $\mathcal{S}_I$ can be used to obtain the geometric sensitivity by taking the ratio of definitions (1.10b) and (2.6), which results in

$$\frac{\mathcal{S}_I}{\mathcal{S}_G} = \alpha\sqrt{\frac{2}{R_{in}}} = \frac{I_0}{\sqrt{P}} \simeq \text{constant}, \tag{2.25}$$

where $\alpha = I_0/I_{in}$ is the ratio of the maximum rung current amplitude, I_0, to the input current, I_{in}, and can be calculated from the coil's circuit equations. In this analysis, α and $\mathcal{S}_G$ are used to separate the effects of circuit topology and geometric sensitivity that in the literature are often lumped into the single quantity, $\mathbf{H}$ [19] or $\mathbf{B_1}$ [16], to which they are related by $\mathbf{H} = \alpha\mathcal{S}_G$ or $\mathbf{B_1} = \mu_0\alpha\mathcal{S}_G$, respectively. By virtue of this separation, improvements in $\mathcal{S}_G$, such as those of Table 2.1, are likely to be translated directly into increases in SNR, since it is plausible to assume that for the minor ellipticity appropriate to the human anatomy, the ratio $\alpha/\sqrt{R_{in}}$ should be not too dissimilar to that of a circular coil of similar dimensions and construction. This ratio is also independent of any lossless network that is used to match the coil's impedance to that of the cables used. Recent experimental results for the human head [20] have reported a $\sim 10\%$ improvement in SNR over circular coils for proton imaging at 1.5T, slightly less than the 14% value that would be predicted by Eqs. (2.24) for their coil dimensions. One might expect improvements in SNR to be closer to ideal the lower the field strength, as sample losses contribute progressively less to the noise compared with coil losses.

2.3.3 Port Imbalance and Noise Performance in Quadrature Operation

To compensate appropriately for the imbalance between the driving ports a knowledge of the input sensitivity of each coil port is required. Port imbalance is not restricted

to oval coils, but can also be observed in circular coils when they are loaded by objects that do not conform to the symmetry of the coil. In such situations a standard 3dB quadrature hybrid will not ensure perfect quadrature RF operation and an elliptically polarized B_1 field will result. Although other authors have pointed out that it *is* possible to construct a shielded elliptical birdcage coil that has equal sensitivities, the solutions adopted [6, 7] pay a price either in elliptically polarized RF if the driving currents are in phase quadrature [6] or a degraded RF field homogeneity [7]. The preferred method is to compensate for differences in input sensitivity, while still maintaining a quadrature phase relationship, by employing a hybrid that splits the input power between the ports in an uneven but controlled way. Such a circuit has been demonstrated [21, §13.09] at microwave frequencies (the branch-line coupler), where the characteristic impedances of four quarter-wavelength transmission line sections in a rectangular configuration were set to determine the coupling coefficient. Given the lower frequencies and the small relative bandwidth of MR, quarter-wavelength sections constructed from discrete components can be substituted for this application.

The same feed configuration can also be shown, by applying the principle of reciprocity [16, 22], to provide correct compensation for the different port sensitivities on reception. The hybrid combination will contain equal contributions from both ports, and the SNR of the output signal will be given by the Pythagorean sum of the single SNR's [23],

$$SNR_{tot} = \sqrt{SNR_{cos}^2 + SNR_{sin}^2}, \tag{2.26}$$

where the *cos* and *sin* subscripts denote the SNR's available from each of the single ports. This result assumes that the noise from the two ports is uncorrelated [24], and that they are matched to the same impedance (usually 50 ohms). In the case of a balanced coil, Eq. (2.26) reduces to the well-known factor of $\sqrt{2}$.

Conclusion

This chapter has demonstrated that because of the intimate relationship that exists between coil currents and shield currents in shielded birdcage coils of both circular and elliptical cross sections, the calculation of magnetic field lines and coil sensitivity can be made without resorting to numerical or approximate solutions. The fundamental result of this work has been to show that for the elliptical coil, not only must a shield be a confocal ellipse to minimize field inhomogeneities (as pointed out earlier [6, 7]), but, to ensure optimal quadrature operation, the quadrature excitation currents to the birdcage elements must also be adjusted according to Eq. (2.22) to compensate for the different geometric sensitivities of the two orthogonal modes. Bringing about this compensation by means of an unbalanced quadrature hybrid also gives rise to properly combined output signals on reception and the SNR's will combine according to Eq. (2.26).

The results can also be applied to compare the sensitivities of circular and elliptical birdcage coils of similar dimensions, in order to predict the potential gain in SNR. In a low-field imaging situation, where the noise is due primarily to the resistive losses in the coil conductors, the estimated gain in SNR is given by comparing the geometric sensitivities (Eqs. (2.24)). At higher fields, where the noise due to the physiological milieu increasingly dominates, the potential performance gain of using anatomically-tailored elliptical coils not as great.

Bibliography

[1] Nicola De Zanche and Peter S. Allen. Sensitivity calculations and comparisons for shielded elliptical and circular birdcage coils. *Magnetic Resonance in Medicine*, 2002.

[2] W.E. Bimson, P.A. Martin, R.D. Griffiths, and R.H.T. Edwards. An elliptical cross section birdcage coil. In *Proceedings of the SMRM 11th Annual Meeting*,

page 272. Society for Magnetic Resonance in Medicine, 1992.

[3] R. Kurczewsky, R. Pavlovich, J.W. Steidly, and N.K. Rollins. Design of elliptically shaped quadrature pediatric body coils. In *Proceedings of the SMRM 11th Annual Meeting*, page 4025. Society for Magnetic Resonance in Medicine, 1992.

[4] L.K. Forbes, Stuart Crozier, and D.M. Doddrell. An analysis and optimization of elliptical RF probes used in magnetic resonance imaging. *Measurement Science and Technology*, 7:1281-1290, 1996.

[5] C.S. Li, C.M. Collins, B.J. Dardzinsky, C. Chin, and M.B. Smith. A method to create an optimum current distribution and homogenous B_1 field for elliptical birdcage coils. *Magnetic Resonance in Medicine*, 37:600-607, 1997.

[6] Mark C. Leifer. Theory of the quadrature elliptic birdcage coil. *Magnetic Resonance in Medicine*, 38:726-732, 1997.

[7] Jeffery S. Keller, Mark L. Leifer, Joe Lo Vetri, Enzo A. Barberi, and Brian K. Rutt. Optimal shield shape for quadrature elliptic birdcage coils. In *Proceedings of the ISMRM 6th Annual Meeting*, page 2038. International Society for Magnetic Resonance in Medicine, 1998.

[8] J. Thomas Vaughan, H.P. Hetherington, J.O. Otu, J.W. Pan, and G.M. Pohost. High frequency volume coils for clinical NMR imaging and spectroscopy. *Magnetic Resonance in Medicine*, 32:206-218, 1994.

[9] Nicola De Zanche and Peter S. Allen. Confocal elliptical birdcage shielding: Calculation of mode sensitivities. In *Proceedings of the ISMRM 7th Annual Meeting*, page 2055, 1999.

[10] R.V. Churchill. *Complex Variables and Applications*. McGraw-Hill, New York, second edition, 1960.

[11] W.R. Smythe. *Static and Dynamic Electricity.* McGraw-Hill, New York, third edition, 1968.

[12] R.A. Beth. Complex representation and computation of two-dimensional magnetic fields. *Journal of Applied Physics*, 37:2568–2571, 1966.

[13] I.S. Gradshteyn and I.M. Ryzhik. *Tables of Integrals, Series, and Products.* Academic Press Inc., New York, 1980.

[14] James Clerk Maxwell. *A Treatise on Electricity & Magnetism.* Dover, New York, third edition, 1954.

[15] Jianming Jin. *Electromagnetic Analysis and Design in Magnetic Resonance Imaging.* CRC Press, New York, 1999.

[16] David I. Hoult and R.E. Richards. The signal-to-noise ratio of the nuclear magnetic resonance experiment. *Journal of Magnetic Resonance*, 24:71–85, 1976.

[17] David I. Hoult and Paul C. Lauterbur. The sensitivity of the zeugmatographic experiment involving human samples. *Journal of Magnetic Resonance*, 34:425–433, 1979.

[18] W.A. Edelstein, G.H. Glover, C.J. Hardy, and R.W. Redington. The intrinsic signal-to-noise ratio in NMR imaging. *Magnetic Resonance in Medicine*, 3:604–618, 1986.

[19] Ogan Ocali and Ergin Atalar. Ultimate intrinsic signal-to-noise ratio in MRI. *Magnetic Resonance in Medicine*, 39:462–473, 1998.

[20] Jeffery S. Keller. Design and performance of a quadrature elliptic birdcage resonator for magnetic resonance imaging. Master's thesis, University of Western Ontario, London, Ontario, Canada, May 1999.

[21] G.L. Matthaei, L. Young, and E.M.T. Jones. *Microwave Filters, Impedance-Matching Networks and Coupling Structures.* Artech House Inc., Norwood, 1980.

[22] E.K. Insko, M.A. Elliott, J.C. Schotland, and J.S. Leigh. Generalized reciprocity. *Journal of Magnetic Resonance*, 131:111–117, 1998.

[23] J. Wang, A. Reykowski, and J. Dickas. Calculation of the signal-to-noise ratio for simple surface coils and arrays of coils. *IEEE Transactions on Biomedical Engineering*, 42:908–917, 1995.

[24] J.W. Carlson. Power deposition and noise correlation in NMR samples. *Magnetic Resonance in Medicine*, 10:399–403, 1989.

Chapter 3

Birdcage Coils on Oval Cylinders

This chapter illustrates a general method for the design of birdcage coils having a non-circular access bore intended to mimic the oval cross-section of specific areas of the human anatomy and thus to improve probe sensitivity. The resulting coils preserve the excellent characteristics of field homogeneity and circular polarisation obtainable with circular-section coils by placing longitudinal conductors at optimal locations on an oval former, and employing a conductive shield whose shape is appropriate to that of the coil former.

3.1 General Theory of Optimal Current Distributions

The following sections will recall and generalise the methodology introduced in refs. [1, 2] and Chapter 2, which utilises the formalism of complex analytic functions and conformal mapping. Two-dimensional magnetic fields are therefore represented by the complex field, H, or by the complex potential, W (c.f. §2.2).

3.1.1 Unshielded Coils on a General Cross Section

Following the methods of §2.2.3 and 2.2.4, the continuous current density required to produce a uniform field, or its approximation using a discrete number of filamentary

currents on the surface of a cylinder of arbitrary cross section, is obtained by utilising a conformal transformation or mapping. Such a transformation can be represented by an analytic function, $f(w)$, which must map the region outside the circular cylinder of radius r, on which the optimal current distributions are known, to the region outside the new former cross section. In order for the mapping's distortion to tend to zero at infinity, and the field's amplitude to be preserved in the transformation, the mapping must satisfy the following condition:

$$\lim_{w\to\infty} \frac{f(w)}{w} = 1. \tag{3.1}$$

This condition imposes the physical constraint that the polarising field, used in §2.2.2 as an intermediate step in the calculation of the current density, be uniform at infinity. The existence of such a mapping is guaranteed, for any closed curve of practical use, by the Riemann mapping theorem (see refs. [3, p. 38] and [4, §2.4]).

Analytic functions can always be expressed as power series [5, §61]. For a coil cross-section having two axes of symmetry the even terms of the series are null and therefore the general expression for the transformation becomes

$$f(w) = w + \sum_{n=1}^{\infty} \frac{c_{2k-1}}{w^{2k-1}}, \tag{3.2}$$

where the coefficients c_{2k-1} are chosen to give the desired shape and they must be such that the series converge for all w of sufficiently large absolute value. In Eq. (2.14), all coefficients are zero except for c_1, and the resulting transformation is appropriate for the ellipse.

To obtain f for other shapes one may search in tables of known transformations [3] or optimise the coefficients of the power series to approximate the required curve [4, §4.2].

Continuous Current Density

To calculate fields in the idealised case where the current distribution is continuous, the inverse transformation $g \triangleq f^{-1}$ is also required, although in general its derivation

is not a trivial task (e.g., it is not possible to invert the transformation of Eq. (3.2) in closed form). Following the same procedure in §2.2.4 the following expressions are obtained for the complex potentials of the magnetic field produced by the ideal current densities on the coil former:

$$W_{sin}^{cont}(z) = \begin{cases} iH_1^{sin}\left[z - \left(g(z) + \frac{r^2}{g(z)}\right)\right] & \text{outside} \\ iH_1^{sin} z & \text{inside} \end{cases} \tag{3.3a}$$

for a field orientation parallel to the real or horizontal axis, and

$$W_{cos}^{cont}(z) = \begin{cases} -H_1^{cos}\left[z - \left(g(z) - \frac{r^2}{g(z)}\right)\right] & \text{outside} \\ -H_1^{cos} z & \text{inside} \end{cases} \tag{3.3b}$$

for the vertical field orientation, where *inside* and *outside* refer to the location of z with respect to the coil former, and where the amplitudes of the excitation of the coil's two modes (represented by field amplitudes H_1^{sin} and H_1^{cos}) may, in general, be unequal. The constant amplitude contours of the real part of the complex potential (the z-component of the magnetic vector potential) will give the magnetic field lines [6, §4.10].

Discrete Approximation Using Filamentary Currents

As pointed out in refs. [1, 2], the optimal placement of the birdcage coil's longitudinal conductors on the new cross section is achieved by mapping the uniformly-distributed conductors on the circular birdcage using the conformal mapping, f. Assuming these N currents to be filamentary, and varying in intensity as the *sine* of their index as in §2.2.1, the magnetic field produced will approximate the field of the potential of Eq. (3.3a), and is given, similarly to Eq. (2.3), by

$$W_{sin}^{disc}(z) = \frac{I_0}{2\pi} \sum_{n=0}^{N-1} \sin\theta_n \log(z - f(re^{i\theta_n})), \tag{3.4}$$

where r is the radius of the circle that maps to the desired curve, $\theta_n = 2\pi\frac{n}{N}$, $n = 0, 1, ...(N-1)$, and the second term in the logarithm represents the new spatial

locations of the birdcage coil's longitudinal conductors. The analogous expression for the vertically-oriented field mode is obtained by changing the angular dependence in the numerator to a *cosine* distribution.

To obtain the geometric sensitivity (defined by Eq. (1.10a)) of the unshielded coil, Eq. (3.4) need not be evaluated directly because at the centre of the discrete coil the field amplitude will closely approximate the amplitude, H_1, produced by the continuous current distribution, even for values of N as low as 8. Furthermore, since the amplitude of the magnetic field is not altered if the condition of Eq. (3.1) is satisfied, it is equal to the amplitude of the field produced by the circular coil of radius r. Consequently the geometric sensitivity is still given by Eq. (2.6), and its calculation reduces to the calculation of r for the desired former shape and dimensions once the transformation f has been determined.

3.1.2 Shielded Birdcage Coils

The issue of designing a shielded quadrature birdcage coil will be approached by maintaining the element positioning as determined in the previous section for the unshielded coil, while searching for a shape of the conducting shield that preserves as much as possible the field homogeneity that is obtainable without a shield. This requires that the currents induced on the shield produce a field that is essentially uniform, so that its superposition with the coil's original field will remain uniform. As a starting point, the idealised case of continuous current distributions will be considered in order to neglect the inhomogeneities due to a finite number of conductors.

Since by definition an ideal shield must be tangent at all points to the magnetic field, it must coincide with a field line and therefore the shield shape can be determined by letting the real part of the complex potential (i.e., the vector potential) be constant. This constant is zero because the shield currents produce an exact cancellation of the original field in the region outside the shield. If $H_2^{sin,cos} \leq H_1^{sin,cos}$ are the amplitudes, for horizontal and vertical field orientations, respectively, of the uniform

fields produced by the shield currents (whose directions will be opposite to those of the fields produced by the coil), the shield contours will then be given by the points that satisfy the following conditions:

$$\Re\left\{iz\left(1-\frac{H_2^{sin}}{H_1^{sin}}\right)-i\left(g(z)+\frac{r^2}{g(z)}\right)\right\}=0 \tag{3.5a}$$

$$\Re\left\{z\left(1-\frac{H_2^{cos}}{H_1^{cos}}\right)-\left(g(z)-\frac{r^2}{g(z)}\right)\right\}=0, \tag{3.5b}$$

for the horizontal and vertical field orientations, respectively, and where $\Re$ is the real operator and z is limited to the region outside the contour of the coil former. The amplitude, $H_2^{sin,cos}$, of the field produced by the shield, can be varied to adjust the size of the resulting shield; values close to H_1 produce shields that closely approximate the shape and size of the coil former, while values close to zero produce large shields of roughly circular shape.

Interestingly, the two shield contours that are obtained from Eqs. (3.5) in general will not coincide, even if H_2^{sin} and H_2^{cos} are chosen independently so that the two curves are approximately the same size. For a quadrature coil, which must produce both field orientations, some intermediate contour must therefore be chosen. Furthermore, for most choices of coil formers H_2^{sin} and H_2^{cos} will be different even if H_1 is the same for both field orientations, a reflection of the fact that the geometric sensitivities of shielded coils on oval shapes are not the same, as has been pointed out in refs. [2, 7] and Chapter 2 for the special case of the ellipse.

The following examples have practical significance and illustrate some of the general properties of the coils obtained by this method.

Four-fold Symmetry

If the coil former contour has four axes of symmetry (e.g., a square), the shield contours for the two field orientations will be the same as will the ratios of the field amplitudes, $H_2^{sin,cos}/H_1^{sin,cos}$. In fact for such a shape the additional symmetry $g(iz) = ig(z)$ reduces Eqs. (3.5) to the same equation if the same H_2 is used for

both field orientations, and only coefficients having indices 3, 7, 11, ... will be finite in Eq. (3.2).

The Ellipse

The previous symmetry condition is a sufficient condition for the shield contours to be the same; however it is not necessary. Another situation in which shield contours coincide is for the elliptical cross section, where the ideal shield contour for both field orientations is an ellipse that is larger and confocal with the coil former. In the appendix (§3.5) it is also shown that the ellipse is the *only* shape not having four-fold symmetry for which the two shield contours coincide. A detailed discussion of the field distributions and consequent improvements in sensitivity that are achievable with elliptical coils is given in Chapter 2 and ref. [2].

The Quartic Section Revisited

The quartic cross section considered in a previous investigation [8] is a surface defined by an equation of fourth degree,

$$\left(\frac{x}{m}\right)^4 + \left(\frac{y}{n}\right)^4 = 1, \tag{3.6}$$

where m and n are the semi-axes of the curve.

A prototype quartic birdcage coil has been discussed in detail in ref. [8], and here we note that in retrospect the shield that was chosen for the prototype is not optimal with regards to field homogeneity, although the particular shape chosen has simplified the tuning procedure somewhat by reducing the differences in the self-inductance of the coil's meshes. Figure 3.1 illustrates the two different shield shapes that would result in perfectly uniform fields parallel to the axes of the coil, compared to the shield section that was actually used.

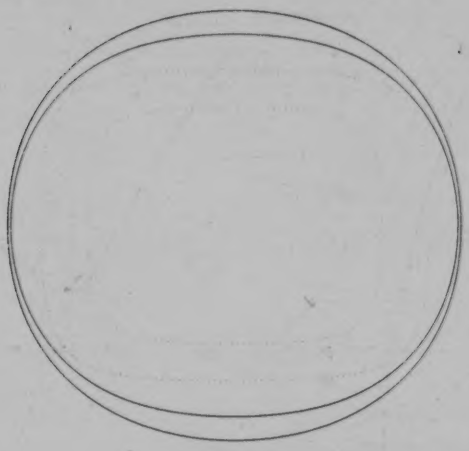

Figure 3.1: The quartic section coil (inner dotted curve) and shield contours. The continuous lines represent shield countours (calculated from Eqs. (3.5) using the same value of H_2 for both modes) that allow the production of perfectly uniform linearly-polarised fields. The actual shield shape that was used for the prototype coil is the larger dotted curve.

Discrete Coils

The discrete equivalents of Eqs. (3.5) are obtained by subtracting the uniform field of amplitude $H_2 < \frac{I_0 N}{4\pi r}$ from Eq. (3.4), and its analog for the *cosine* distribution, and taking the real part:

$$\Re\left\{\frac{I_0}{2\pi}\sum_{n=0}^{N-1}\sin\theta_n \log(z - f(re^{i\theta_n})) - izH_2^{sin}\right\} = 0 \tag{3.7a}$$

$$\Re\left\{\frac{I_0}{2\pi}\sum_{n=0}^{N-1}\cos\theta_n \log(z - f(re^{i\theta_n})) + zH_2^{cos}\right\} = 0. \tag{3.7b}$$

Notice that, in contrast to Eqs. (3.5), it is not necessary to have the inverse transformation, g, to calculate the shield contours using Eqs. (3.7). Also, shields chosen in this manner cannot *compensate* for non-uniform field components that are already present without the shield because they are designed simply to produce a uniform field which is subtracted from that produced by the coil elements. The inhomogeneities

due to the finite number of discrete currents, for example a dipole field component due to an incorrect placement of the elements, will still be present with the shield in place. The contours produced will depend on N as well as H_2, and in general they will exhibit similar overall differences in shape between the two orthogonal field orientations as for the idealised case of continuous current distributions.

The example shown in Figure 3.2, is obtained using the first three terms of the series expansion of Eq. (3.2). The values of H_2 needed to produce shields of approximately the same size for the two field orientations were 15% different, illustrating once again that the linear modes of shielded oval coils have different geometric sensitivities. The figure also shows that the shield contours obtained from Eqs. (3.7) will be somewhat corrugated in correspondence to the coil's elements, although this effect is reduced as the shield is moved away from the elements by decreasing H_2. Similarly to the idealised continuous current distributions, the two contours are somewhat different in shape, therefore a practical intermediate shield shape must be employed for the construction of quadrature coils.

3.1.3 The Cassinian Head Coil Prototype

To verify the theory presented above a prototype coil having $N = 16$ elements was designed with dimensions adequate for the dimensions of the average adult human head [9]. An oval shape known as the oval of Cassini having access diameters of 22 cm and 28 cm was chosen due to its regular curvature even for high axial ratios. The ovals of Cassini are defined, similarly to the ellipse, as the locus of a point such that the *product* of its distances from two fixed points (foci) is constant, and are obtained by transforming a circle of radius r_1 using the transformation [3, §1.10.2]

$$z = w\sqrt{1 + \frac{c^2}{w^2}}, \tag{3.8}$$

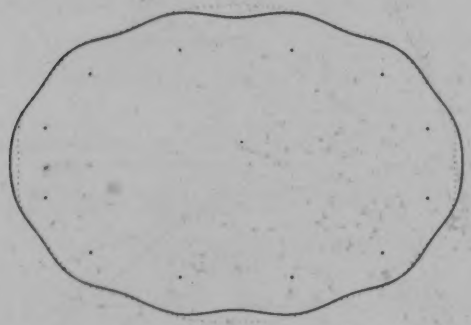

Figure 3.2: Elemental placement for a three-term truncation of the transformation function of Eq. (3.2) and the corresponding shield contours appropriate for fields oriented parallel to the coil axes (solid line for the major-axis field orientation and dotted line for the minor-axis orientation. The contours obtained for discrete current distributions are seen to be dependent on field orientation like their counterparts for continuous distributions, but also exhibit corrugations in correspondence to each filamentary current.

where $c < r_1$ is 1/2 the focal distance and is related to the major and minor radii of the Cassinian, respectively m_1 and n_1, by

$$c = \sqrt{\frac{m_1^2 - n_1^2}{2}} \tag{3.9a}$$

$$r_1 = \sqrt{\frac{m_1^2 + n_1^2}{2}} \tag{3.9b}$$

The ovals of Cassini are better suited than the ellipse for the construction of anatomically-tailored birdcage coils because they maintain a regular curvature even when the aspect ratio is relatively high. A further advantage is that the inverse transformation, $g(z)$, required to calculate the shield contours, is given by the simple expression

$$w = \sqrt{z^2 - c^2}. \tag{3.10}$$

Shield contours for the two linear modes were obtained using equations (3.5) instead of the more exact version for discrete current distributions (Eqs. (3.7)) because

the consequent shield corrugations would affect the field mainly in the region between the shield and the coil elements rather than in the useful region inside the coil. Construction of the shield is therefore simplified. As expected, the shield contours are not identical but they can be closely approximated by a *confocal* Cassinian, obtained by transforming, using Eq. (3.8), a circle of radius $r_2 > r_1$. A relationship identical to Eq. (3.9b), but with the subscripts 1 replaced by 2, relates r_2 to the major (m_2) and minor (n_2) radii of the shield, which for the prototype head coil were chosen to be 16.4 cm and 13.9 cm, respectively.

The use of a confocal Cassinian shield is also convenient because its effect on the field produced by a discrete coil is accounted for by a second conformal transformation, $\phi(\zeta)$, instead of the more laborious numerical solution of the boundary-value problem that would be required for the ideal contours found using Eqs. (3.5). The relative simplicity of the expression for ϕ is also computationally advantageous over other shapes such as the ellipse, for which elliptic integrals of the first kind must be calculated numerically [3, p.295]. For the Cassinian the expression is [3, p.294]

$$\omega = \phi(\zeta) = \zeta\sqrt{\frac{p}{p+\zeta^2}}, \tag{3.11}$$

where

$$p = \frac{2m_2^2n_2^2}{m_2^2 - n_2^2} \tag{3.12}$$

is a parameter of the transformation that increases as the axial ratio, m_2/n_2, of the shield tends to one (i.e., the shield increases in size and tends to a circle). The transformation maps the *interior* of the Cassinian shield in the ζ plane to the interior of the circle of radius

$$\rho = \sqrt{\frac{2m_2^2n_2^2}{m_2^2 + n_2^2}} = \frac{m_2n_2}{r_2} \tag{3.13}$$

in the ω plane, where the method of images may be used to calculate the fields (c.f. Appendix C). The variables associated with this transformation are Greek letters to distinguish them from those of the other transformation, f.

It is important to notice that at the origin the derivative of ϕ is unity, and therefore at that point the field amplitudes in the two planes are identical. Consequently the calculation of the coil's sensitivities can be done in the ω plane without requiring an inverse transformation. We begin by determining the positions, ω_n, of the elements inside the circular shield by mapping the original equally-spaced positions on the circle of radius r_1 with the transformation of Eq. (3.8) followed by the transformation of Eq. (3.11), resulting in

$$\omega_n = e^{i\theta_n}\sqrt{\frac{p(r_1^2 + c^2 e^{-2i\theta_n})}{r_1^2 e^{2i\theta_n} + c^2 + p}}. \tag{3.14}$$

Now the method of images can be applied to each element (c.f. Appendix C), and by superposition of the corresponding fields the following expression is obtained for the geometric sensitivity at the origin:

$$S_{G,\sin} = \frac{1}{2\pi\rho^2}\left|\sum_{n=0}^{N-1} \sin\theta_n \left(\omega_n^* - \frac{\rho^2}{\omega_n}\right)\right|, \tag{3.15}$$

for the horizontal field mode, where the asterisk indicates complex conjugation. The corresponding expression for the vertical field mode is obtained by changing to a *cosine* dependence on θ_n.

For the dimensions chosen for the prototype head coil, the geometric sensitivities for the major and minor-axis modes are, respectively, 3.47 and 2.95 m^{-1}. By comparison, the sensitivity of a shielded circular coil having the same radii as the major radii of the Cassinians, and the same number of elements ($N = 16$), is 2.47 m^{-1}, an average of 30% lower.

To obtain the complete field lines we must similarly calculate the complex potential in the ω plane, which then needs to be transformed back to the ζ plane by using the inverse of the transformation of Eq. (3.11). The results (equal amplitude contours of the real part of the potential) are shown in Figure 3.3, where it is evident that the fields are highly homogeneous even though the shield contour chosen is not optimal for either mode, nor is it corrugated. In fact, for any practical number N of

discrete conductors, the detrimental effect on homogeneity of using such a "compromise" shield contour is not worse than the effect of using a discretised version of the continuous current density or of truncating the coil to a practical length.

3.2 Modal Analysis and Capacitor Optimisation

Since the theoretical analysis of the previous sections assumes a (co)sinusoidal linear-mode current distribution on the coil's rungs, one must determine the coil topology and distribution of capacitance required to produce these currents at the coil's desired resonance frequency (in the case of our prototype 128 MHz). For maximal flexibility our prototype employs a hybrid birdcage coil topology [10, §4.3.4], whereby capacitors are placed in series with all sections of the end-rings, as well as in series with all of the rungs. This configuration allows enough degrees of freedom (the single capacitance values) to satisfy simultaneously both the requirement of mode degeneracy as well as producing the correct current distributions. The coil's three planes of symmetry reduce the number of unknown capacitances to $N/2 + 1$.

3.2.1 Analytical Method for Calculation of Capacitances

The initial approach used to determine these unknown capacitances was the analytical procedure termed "mesh inductance equalisation" suggested by Leifer in [1], which makes use of a lumped-element model of the birdcage coil. Differences in the self-inductance of the coil meshes, as well as differences in the mutual inductance between adjacent elements, are compensated for by appropriate trim capacitors or inductors in order to mimic the circulant inductance matrix of a circular birdcage. Unfortunately our implementation of this approach failed to produce resonance of the prototype coil's two linear modes at the same frequency, as required for proper quadrature operation. This analytical procedure has also been shown by others to be inadequate [11], and this is probably due to a combination of two factors. Firstly, at the 3T proton imaging frequency (128 MHz) the wavelength effects can no longer be neglected,

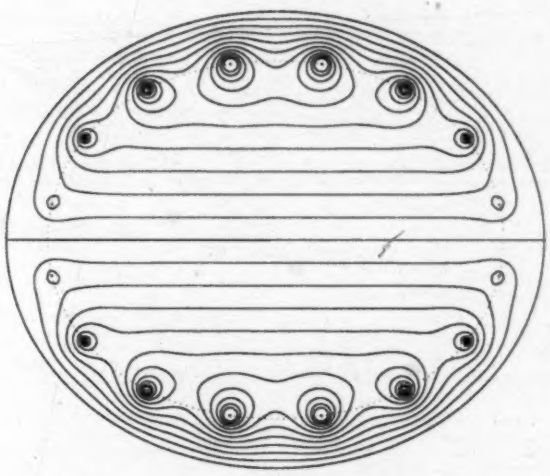

(a) Horizontal Mode

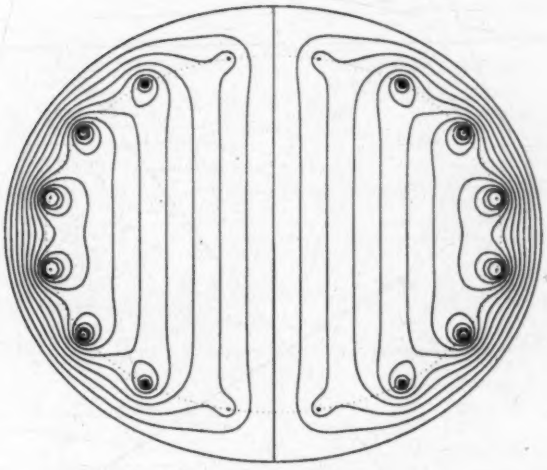

(b) Vertical Mode

Figure 3.3: Magnetic field lines of a) the horizontal and b) the vertical field modes of the Cassinian head coil. The difference in field amplitude between the two field orientations is due to the different geometric sensitivities of the two modes.

and therefore the original lumped-element, low-frequency model becomes inaccurate. Secondly, higher-order mutual couplings between elements are not compensated for by this method, hence the resulting matrices are not perfectly circulant causing, in general, the mode 1 resonant frequencies to split and the modal currents to deviate from the ideal sine and cosine distributions.

3.2.2 Numerical Optimisation of Capacitances

The optimal capacitances needed to produce proper quadrature operation and current distributions were subsequently determined by numerical means. The coil was modelled using numerical method of moments software (NEC-2 [12]) similarly to that of ref. [11], but with the addition of the shield, modelled as a fine mesh of wires (c.f. Figure 3.4). This wire mesh, generated using the WIREGRID utility [13], produced an increase in the number of unknowns by roughly a factor of 4 with respect to the unshielded coil. This increase in model complexity leads to a considerable increase in execution time (a factor of approximately 70) due to the cubic relationship between these variables.

Furthermore, since our prototype was constructed of conducting strips, while the method of moments software can simulate only cylindrical wires, a calibration was required to determine the radius of the cylindrical wires that would produce equivalent resonance properties. A rectangular test mesh having dimensions 20×4 cm of 6mm-wide copper strips was constructed with two 32pF capacitors at each end and its resonant frequency was measured to be 68 MHz. A model of this mesh was implemented in NEC2 and the wire radius was varied until the predicted resonant frequency coincided with the measured value. The equivalent cylindrical wire radius was determined to be 1.53 mm, against a value of 1.42 mm predicted by the equal inductance per unit length rule [10, §A.2].

Capacitor optimisation was then implemented by iteratively calling NEC-2 with the MATLAB® function `fminsearch()` to minimise both the RMS deviation from

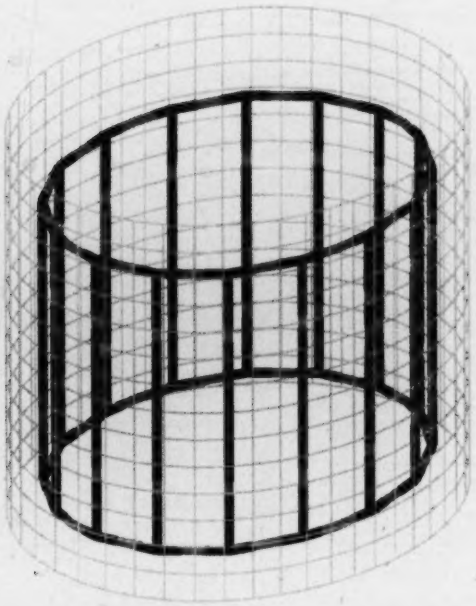

Figure 3.4: The NEC wire model of the shielded Cassinian coil prototype includes thick grey segments to indicate the position of the capacitors on the ladder network and a wire mesh to model the shield.

the ideal current distribution as well as the absolute value of the error in resonant frequency. The complete optimisation of the capacitances for the shielded coil took several days and over 200 iterations on a Pentium III®, 500 MHz. Initial and final capacitance values are given in Table 3.1, and program details are provided in Appendix B.

3.3 Experimental Verification

The performance of the prototype Cassinian head coil was compared to that of a standard circular coil of similar construction and dimensions. In order to permit a comparison based only on the cross section, the two coils have the same element length (20 cm), major access diameter (28 cm), and major shield diameter (33 cm), while the Cassinian coil's minor access diameter is 22 cm and the shield's minor diameter is 28 cm. The length was chosen to maximise the coil's input sensitivity [14] while maintaining axial homogeneity adequate for brain MRS or functional MRI of the occipital cortex.

Initial tests were performed with both coils matched for unloaded conditions. In this manner small samples and lossless oil-filled phantoms could be used to determine the field profiles of the empty coil, consistently with the theory and simulations.

3.3.1 Coil Construction and Tuning

Both the prototype Cassinian coil and the standard circular coil were constructed on polycarbonate plastic frames on which adhesive copper strips forming the ladder networks were attached (c.f. Fig. 3.5). Ceramic chip capacitors were then measured and matched as closely as possible to the values determined by the optimisation, and finally soldered to the copper strips. An aluminum foil shield was installed on the outer portion of the polycarbonate frames, and the final tuning of the coils' resonant frequencies was accomplished by trimming the width of the copper strips on the end

	C_1	C_2	C_3	C_4	C_5	C_{12}	C_{23}	C_{34}	C_{45}
initial	33	33	33	33	33	300	300	300	300
final	35.99	35.44	32.93	29.87	28.19	300.2	276.4	355.0	522.3
actual value	18+18	27+8.2	33	15+15	10+18	150+150	220+56	270+82	470+56
circular coil	33	33	33	33	33	220	220	220	220

Table 3.1: Initial and final values in the optimisation of the capacitances of the Cassinian head coil are shown for comparison with those used in the standard circular coil (last row). Nominal values used in the Cassinian coil are also indicated (the + sign indicates capacitors in parallel). Capacitances labelled C_i are on the end-ring segments, while C_{ij} are on the longitudinal segments of the coil (see Fig. 1.10(a)). The similarities in their capacitance values confirms that the electrical parameters of the two coils are related only by a small perturbation. All values are in picoFarads.

Figure 3.5: The Cassinian coil prototype with shield removed for clarity.

rings to adjust their inductance. Table 3.1 illustrates the resulting electrical similarity of the two coils indicated by the similar values of capacitance used.

After matching networks were connected across end-ring capacitors on two orthogonal ports on the axes of the coil, the isolation was measured to be better than 20 dB, and return loss better than 25 dB with the coil unloaded. A standard 3dB quadrature hybrid is used for quadrature operation, since the input sensitivities (Eq. (1.10b)) of the two ports were found to be approximately the same (c.f. §3.3.3). In cases where the input sensitivities are unequal, such as for high aspect ratios, a custom hybrid (c.f. §2.3.3) may be constructed to compensate for the difference.

Port Number	Cassinian Coil				Circular Coil			
	Unloaded	Loaded	Ratio	η [%]	Unloaded	Loaded	Ratio	η [%]
1	247	24	10.3	90	250	56	4.5	77
2	251	30	8.4	88	246	58	4.2	76

Table 3.2: Comparison of the loaded and unloaded quality factors and damping ratios of the Cassinian and circular head coils. The Cassinian's higher damping ratios are indicative of better noise performance and higher efficiency (losses in the patient relative to the total losses).

3.3.2 Probe Quality Factor

The quality factor, Q, is an important parameter that can be measured on the workbench and can be indicative of the noise performance of an NMR probe (c.f. §6.4.3). Measurements of Q were performed on both coils according to the method indicated in §6.4.2, with the coil unloaded as well as loaded by a head-size saline phantom (3.8 l, 0.07M NaCl, 0.01M $CuSO_4$). Results are given in Table 3.2, where the higher Q-damping factors indicate that the Cassinian coil is more sensitive to the load, and therefore more efficient [15], than the standard circular coil.

3.3.3 Field and SNR Measurements

Magnetic field polarisation and homogeneity measurements were performed to compare the quadrature operation of the two coils and to verify the RF field uniformity. To obtain quantitative field amplitude measurements, we chose to use a small sample of water (1.4 ml) and determine the 180° pulse duration [16]. The RF magnetic field is therefore altered minimally with respect to the empty coil and is effectively sampled at the point in the coil where the sample is located.

The relative input sensitivity of each port was measured by connecting the coil to both transmit and receive from a single port, while the other port is damped using a dummy load. Consequently, the coil operates in linear mode, and the field amplitudes calculated from the 180° pulse length are actually one half the linear-field amplitudes. The linear polarisation ratio, defined as the ratio of the two linear-

Coil type	Polarisation Ratio	
	Linear	Circular
Circular	1.1828	0.090
Cassinian	1.0141	0.041

Table 3.3: Field polarisation ratios measured at coil centre: comparison of circular and Cassinian coil. An ideal circularly polarised field has a circular polarisation ratio of zero or equivalently a linear polarisation ratio of 1.

field amplitudes [17, §2.5] produced by equal power into the two ports, was closer to the ideal unitary value for the Cassinian coil, which indicates that even for circular coils the constructive tolerances of the matching networks and other factors that are difficult to control inevitably contribute to creating an unbalanced coil.

The circular polarisation ratio was then measured in quadrature operation with a 3dB hybrid by transmitting with the primary circular component of the field, and receiving initially with the counter-rotating mode. The connections to the hybrid were then changed to a normal connection where reception is with the circular component that rotates in the same sense as the nuclear spins, and the signal amplitudes obtained from the same flip angle (90°) were compared. By reciprocity, the ratios of the signal amplitudes coincide with the circular polarisation ratio of the field in transmission, and the results are tabulated in Table 3.3 for both coils. Again we see that the Cassinian coil performs better than the circular coil, achieving a lower circular polarisation ratio. The linear and circular polarisation ratios ideally are related by a bilinear transformation [17, §2.7]; however, the discrepancies that are observed between these two measurement methods can be accounted for by factors such as the imperfect power splitting of the 3dB hybrid, and the insertion loss of the receiver's T/R switch in the linear-field measurements.

The RF magnetic field profiles along the z-axis, shown in Figure 3.6 for both coils, were then measured by moving the small water sample along the axis by 2cm increments for each successive field measurement (c.f. §6.5.1). It is seen that the Cassinian coil's $\mathbf{B_1}$ field distribution is quite similar to that of the standard circular

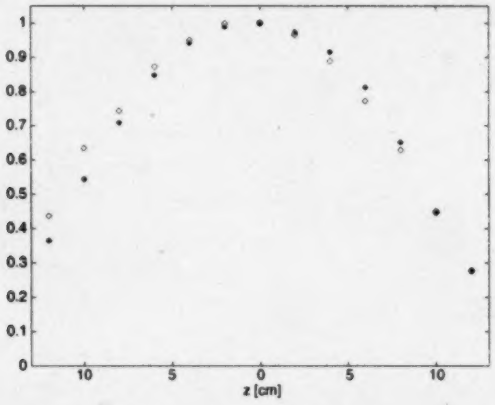

Figure 3.6: Field amplitude plots normalised to maximum at coil centre: the circles (o) indicate field samples along the circular coil's axis obtained with a small spherical sample of water moved by 2cm intervals; the asterisks (*) indicate the field amplitudes along the Cassinian coil's axis. Axial field homogeneity is seen to be essetially identical for the two prototype coils.

coil. At the edges of both coils (at the end-rings, $z = 10$ cm) the RF field drops to about one half its value at the centre, and the useful region is roughly 10 cm in axial length, adequate for functional imaging of cortical regions of the brain, for example.

In addition to field mapping, some qualitative field profiles, shown in Figure 3.7, were obtained from transverse and coronal spin-echo images ($T_E = 30$ ms, $T_R = 1$ s) of a spherical flood-field phantom containing transformer oil (Voltesso 35, nominal relative permittivity $\epsilon_r = 2.2$). The similarity of the curves obtained using the two coils confirms that the field produced by the Cassinian coil closely approximates the gold-standard achievable with the circular birdcage, and therefore the excellent field homogeneity has been preserved.

The matching circuits of both coils were subsequently modified to utilise the coils under realistic loading conditions, and data from in-vivo imaging and spectroscopy experiments were compared. Brain images were acquired using a gradient-echo sequence ($T_E = 22$ ms, $T_R = 500$ ms) and the SNR was calculated as the ratio of the

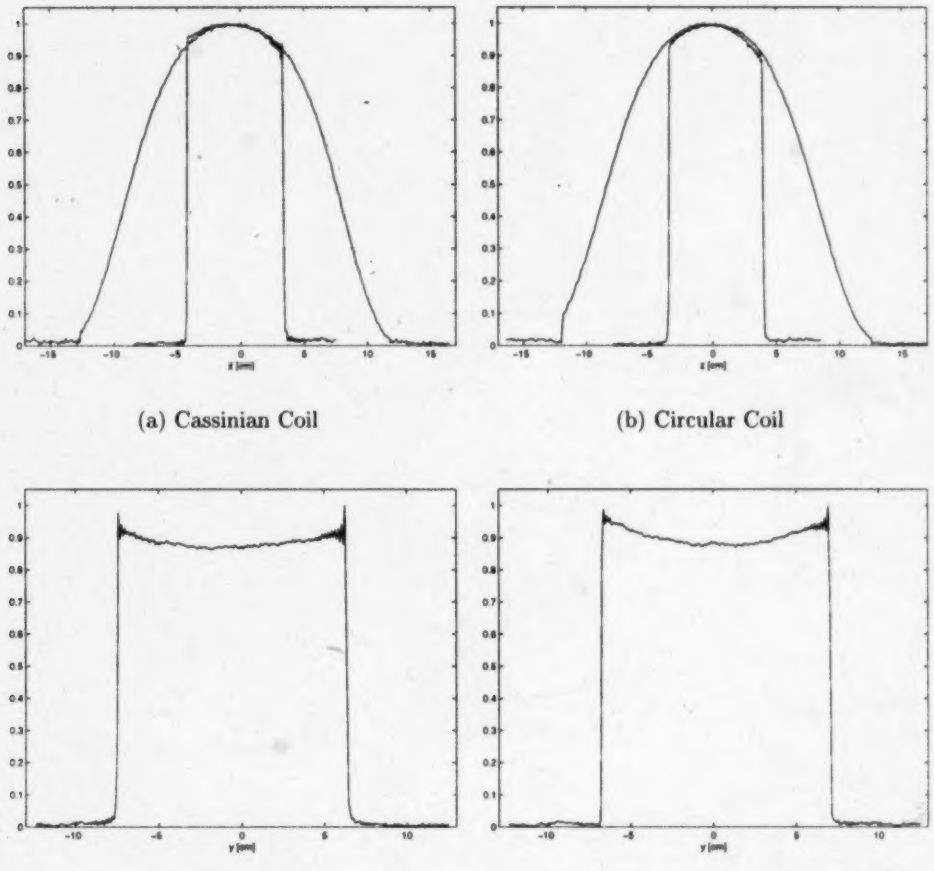

(a) Cassinian Coil

(b) Circular Coil

(c) Cassinian Coil

(d) Circular Coil

Figure 3.7: Normalised axial and transverse spin-echo image profiles of a spherical oil phantom obtained using the Cassinian head coil and the standard circular coil for comparison. a) and b) are the superposition of two profiles obtained by acquiring two images with the phantom offset by ± 4 cm in the axial (z) direction, while for c) and d) the phantom was centered in the coil. Profile c) is taken along the major-axis direction of the oval coil.

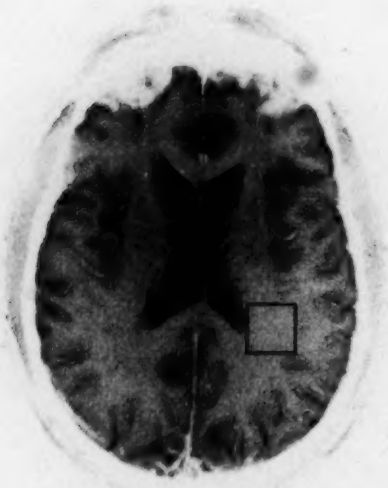

Figure 3.8: Typical brain image obtained using the Cassinian coil prototype. The square indicates the region used to calculate the average signal for the image SNR measurements and also the approximate location of the voxel from which the spectra of Fig. 3.9 were obtained.

average signal amplitude in a 2 × 2 cm region of the occipital lobe, to the standard deviation of the noise, calculated in the top 2 × 2 cm corner of the image where the signal is null. Figure 3.8 shows a typical image and the region used to calculate the average signal. The improvement in image SNR of the Cassinian head coil over the standard circular coil was measured to be an average of 18% over several slices and for two values of the excitation flip angle. Proton spectra acquired from the occipital lobe (Figure 3.9) confirm that there is a 20% improvement in SNR and therefore in input sensitivity (c.f. §1.3.4) in using the Cassinian coil over the circular coil. These values are somewhat lower than the 30% expected improvement in *geometric* sensitivity because of the contribution of noise from the sample which cannot be distinguished from the signal.

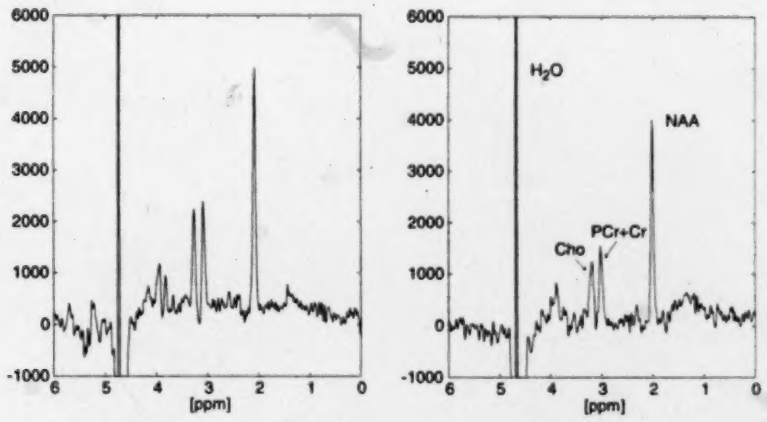

(a) Cassinian Coil (b) Circular Coil

Figure 3.9: Spectra obtained from a $2 \times 2 \times 2$cm voxel in the occipital lobe using a PRESS sequence ($T_E = 120$ ms, $T_R = 4$ s, 32 averages). The SNR gain of a) the Cassinian coil over b) the circular coil is approximately 20%.

3.4 Conclusion

We have demostrated a general method to design and construct anatomically-tailored coils that offer significant improvements in sensitivity over circular coils of similar dimensions, without sacrificing field homogeneity in the process. The degree of improvement depends largely on the axial ratio of the curve and on the frequency of operation. The greatest improvements can be had at lower frequencies, where coil losses are predominant over tissue losses, and with coils whose shape closely conforms to the anatomical region for which they are designed.

While the methodology can be used to determine optimal element placement and shield shape for a large class of cross-sectional shapes, our prototype was constructed on an oval of Cassini, which is able to approximate the shape of many sections of the human anatomy better than the ellipse, the curve previously considered by other

authors. The optimal shield shapes that correspond to the two linear modes of the Cassinian coil do not coincide, as is shown to be uniquely the case for the elliptical geometry, but a shield constructed on a *confocal* Cassinian was found not to alter the field homogeneity appreciably, and to allow the calculation of the field inside it more easily than inside an elliptical shield when the current is discrete. Typical improvements in input sensitivity or signal-to-noise ratio were approximately 20% for a coil designed to accomodate the average adult human head and operate at the 3T proton frequency (128 MHz).

3.5 Appendix: Unique Properties of Confocal Elliptical Shielding

In this appendix we show that the ellipse is the only cross-sectional shape for which the ideal shield is obtained by transforming, using the same transformation $f(z)$ that is used to obtain the coil former, a circle having a radius $r_2 > r_1$, where r_1 is the radius of the circle used to obtain the coil former. Furthermore, the ideal shield is the *same* for both modes and thus the field homogeneity is uncompromised in a quadrature implementation.

The proof begins by noticing that if the currents induced on the shield produce uniform fields inside it, the potentials, $\mathcal{W}^{shield}$, of such fields will have expressions similar to Eqs. (3.3), where the amplitudes $H_1^{sin,cos}$ are substituted by $H_2^{sin,cos}$, and the superscript *shield* emphasises the location of the sources. The superposition of the fields due to the currents on the coil (indicated by a superscript *coil*) and shield must yield a null field outside the shield, i.e.,

$$\frac{d}{dz}\left[\mathcal{W}^{coil}(z) + \mathcal{W}^{shield}(z)\right] = 0. \tag{3.16}$$

Substituting for $\mathcal{W}^{coil}$ and $\mathcal{W}^{shield}$ and collecting the z-dependent terms we obtain

$$\frac{g'(z)-1}{g'(z)} g^2(z) = \frac{H_1^{sin} r_1^2 + H_2^{sin} r_2^2}{H_1^{sin} + H_2^{sin}} \triangleq k^{sin} \tag{3.17a}$$

for the horizontal mode, and

$$\frac{1-g'(z)}{g'(z)}g^2(z) = \frac{H_1^{cos}r_1^2 + H_2^{cos}r_2^2}{H_1^{cos} + H_2^{cos}} \triangleq k^{cos} \tag{3.17b}$$

for the vertical mode. It is evident that these two equations are very similar, and indeed we need to reduce them to a single equation by imposing $k^{sin} = -k^{cos} \triangleq k$ to obtain a single transformation for both field orientations. This constraint is verified for example by choosing the field amplitudes according to the relationships of Eqs. (2.18). The resulting differential equation,

$$\frac{g^2(z)-k}{g^2(z)}g'(z) = 1. \tag{3.18}$$

is readily integrated, and the integration constants are taken care of by imposing that the origin be the centre of the transformation and that its asymptotical behaviour be governed by Eq. (3.1). The transformation that we obtain,

$$g(z) = \frac{z+\sqrt{z^2-4k}}{2}, \tag{3.19}$$

is unique and has exactly the same form that is required for an elliptical coil, with $k = a^2/4$ being one quarter of the focal distance squared (c.f. §2.2.3), thus concluding the proof.

Bibliography

[1] Mark C. Leifer. Theory of the quadrature elliptic birdcage coil. *Magnetic Resonance in Medicine*, 38:726–732, 1997.

[2] Nicola De Zanche and Peter S. Allen. Sensitivity calculations and comparisons for shielded elliptical and circular birdcage coils. *Magnetic Resonance in Medicine*, 2002.

[3] V.I. Ivanov and M.K. Trubetskov. *Handbook of Conformal Mapping with Computer-Aided Visualization.* CRC Press, New York, 1995.

[4] R. Schinzinger and P.A.A. Laura. *Conformal Mapping: Methods and Applications.* Elsevier, 1991.

[5] R.V. Churchill. *Complex Variables and Applications.* McGraw-Hill, New York, second edition, 1960.

[6] W.R. Smythe. *Static and Dynamic Electricity.* McGraw-Hill, New York, third edition, 1968.

[7] Jeffery S. Keller, Mark L. Leifer, Joe Lo Vetri, Enzo A. Barberi, and Brian K. Rutt. Optimal shield shape for quadrature elliptic birdcage coils. In *Proceedings of the ISMRM 6th Annual Meeting*, page 2038. International Society for Magnetic Resonance in Medicine, 1998.

[8] Terry A. Riauka, Nicola F. De Zanche, Richard B. Thompson, Fred E. Vermeulen, Clarence E. Capjack, and Peter S. Allen. A numerical approach to non-circular birdcage RF coil optimization: Verification with a fourth-order coil. *Magnetic Resonance in Medicine*, 41:1180–1188, 1999.

[9] L.G. Farkas, editor. *Anthropometry of the Head and Face.* Raven Press, New York, second edition, 1994.

[10] Jianming Jin. *Electromagnetic Analysis and Design in Magnetic Resonance Imaging.* CRC Press, New York, 1999.

[11] Jeffery S. Keller, Joe Lo Vetri, Enzo A. Barberi, and Brian K. Rutt. Tuning of the quadrature elliptic birdcage coil–part I: Mesh inductance equalization. In *Proceedings of the ISMRM, 7th Annual Meeting*, page 2057, Philadelphia, 1999. International Society for Magnetic Resonance in Medicine.

[12] G.J. Burke and A.J. Poggio. *Numerical Electromagnetics Code (NEC-2) Manual, Part III: User's Guide.* Lawrence Livermore National Laboratory, Livermore, CA, 1981.

[13] C.F. Du Toit and D.B. Davidson. Wiregrid: A NEC2 pre-processor. *Journal of the Applied Computational Electromagnetics Society*, 10(1):31–39, 1995.

[14] P.A. Bottomley, H.C. Charles, P.B. Roemer, D. Flamig, H. Engeseth, W.A. Edelstein, and O.M. Mueller. Human *in vivo* phosphate metabolite imaging with ^{31}P NMR. *Magnetic Resonance in Medicine*, 7:319–336, 1988.

[15] H. Wen, T.J. Denison, R.W. Singerman, and R.S. Balaban. The intrinsic signal-to-noise ratio in human cardiac imaging at 1.5, 3, and 4 T. *Journal of Magnetic Resonance*, 125:65–71, 1997.

[16] David I. Hoult, C.-N. Chen, and V.J. Sank. Quadrature detection in the laboratory frame. *Magnetic Resonance in Medicine*, 1:339–353, 1984.

[17] Carlo G. Someda. *Electromagnetic Waves*. Chapman & Hall, New York, 1998.

Chapter 4

TEM Resonators on Oval Cylinders

In the previous chapter the optimal positioning of the coil elements was determined by conformal mapping, while the modal analysis and calculation of the capacitances required for quadrature operation was performed numerically. This numerical approach was required because of the limitations of the lumped-element model of the birdcage coil as well as those of the mesh inductance equalisation method [1]. In the present chapter the modal analysis will be performed analytically for the TEM resonator by generalising the multiconductor transmission line theory used by Baertlein et al. [2] for the application to the general case of a non-circular coil. Consequently there is a large savings in computational costs needed for the design of such a resonator. As a working example, the Cassinian cross section will be considered, although *any* shield cross section may be used as long as there is a way to determine the transverse magnetic field produced by the current elements inside it. For example, it may be applied to the elliptical section, for which some experimental results have already been obtained [3].

4.1 Inductance Matrix of the Cassinian Transmission Line

As noted in §3.1.3, the conformal transformation in Eq. (3.11) is used to map the interior of the Cassinian shield to the interior of the circular shield where the method of images may be used. This transformation was used to determine the magnetic field distribution with sufficient accuracy to verify that the field inside a Cassinian birdcage coil is adequately uniform in the region occupied by the patient. The currents were assumed to be filamentary and to vary with the sine or cosine of their index.

To calculate the inductance matrix, **L**, required for the modal analysis of a TEM resonator (c.f. §1.3.2), however, the assumption of filamentary current distribution must be modified because it would lead to infinite inductances. Due to the phenomenon known as the "skin effect", a radio frequency current flowing on an *isolated* circular copper wire will be distributed uniformly on its *surface* [4, §4.4]. The magnetic field outside the wire is consequently the same as the field produced by a filamentary current at the wire's *axis*, while inside the wire it is null. If the wire is surrounded by a circular shield whose axis is parallel to but not coincident with that of the wire, the field will be distorted and the position of the equivalent filamentary source current will be displaced from the wire's axis as shown in Appendix C.1.

If the shield has a non-circular cross-section such as the Cassinian oval, a conformal transformation, e.g., Eq. (3.11), is needed to determine the field inside the new shield. If the coil elements are placed at locations ω_n in the model plane according to Eq. (3.14), their radii in the model plane, Δ_n, are determined from the original radii, δ_n, by multiplication with the absolute value of the derivative of transformation (3.11) at the elements' locations, ζ_n, in the Cassinian plane, resulting in

$$\Delta_n \simeq \delta_n \left| \frac{p}{p+\zeta_n^2} \right|^{\frac{3}{2}}, \tag{4.1}$$

where $\zeta_n = r_1 e^{i\theta_n} \sqrt{1 + c^2 e^{-2i\theta_n}}$ and c, r_1 have the same meanings as in Eq. (3.8). This approximation is valid if each element's radius is small relative to the distortion

produced by the conformal transformation of Eq. (3.11). From ω_n, Δ_n, and the shield radius, ρ (c.f. Eq. (3.13)), the axial displacements, f_n, of the equivalent filamentary currents in the circle plane are determined by using Eqs. (C.1). It is important to determine these displacements for the correct application of the method of images and the calculation of the inductances when the longitudinal conductors have finite transverse dimensions.

Another consequence of using conductors of finite cross-section is the distortion of the magnetic field patterns due to the additional boundary conditions imposed by the elements themselves. In fact, if only one of the N elements carries a net current, each of the other elements will locally displace the magnetic field lines so that they will not penetrate inside the conductor. A first-order approximation of the resultant field is obtained by assuming that the original field at the element's location is approximately uniform, and therefore each non-driven element produces a field identical to that produced by a magnetic dipole. The effect of the nearby circular shield is accounted for by using the method of images applied to magnetic dipoles (c.f. Appendix C.2).

The potentials obtained in the model (circle) plane by the superposition of the effects of the equivalent source currents and their respective images, and the dipoles and their respective images, are transformed to the original problem plane by using the transformation of Eq. (3.11). Sample field-line plots of a single driven element are shown for both planes in Figure 4.1, where the effect of the boundary conditions imposed by the non-driven elements is readily observed by the bending of the field lines around them.

It is now possible to apply the definition (see ref. [4, §2.5 and 4.7]) of the inductance L of a closed circuit as the ratio of magnetic flux enclosed by the circuit to either the current that flows in the circuit (self inductance) or another current that is producing the field (mutual inductance). From the properties of conjugate functions [5, §4.11], the magnetic flux per unit length between two points in a field having

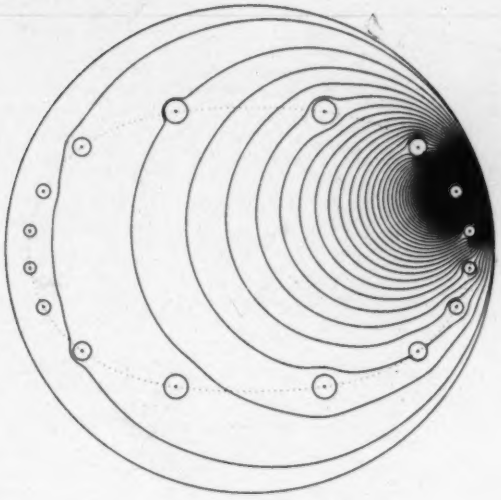

(a) Model Plane

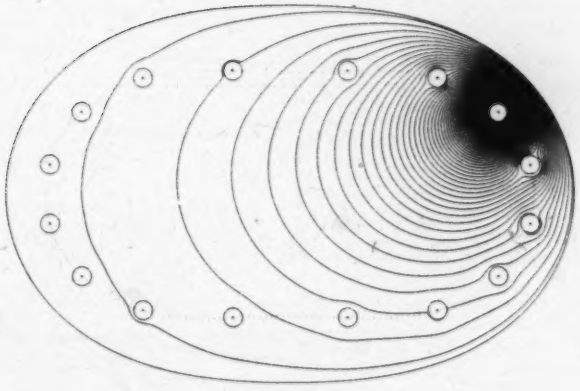

(b) Problem Plane

Figure 4.1: Magnetic field lines in a) the model (circle) plane and b) the problem plane of a TEM coil having a Cassinian shield. Only one element carries a net current while the others locally distort the field lines that it produces. The dashed lines indicate b) the oval of Cassini on which the coil elements are placed, and a) its image in the circle plane which is not a Cassinian.

complex potential $W(z)$ is equal to the difference of the values of the real part of the potential (the *stream* function) at those points, multiplied by the magnetic permeability, μ, of the medium. The self inductance per unit length of the longitudinal elements of a transmission line having any shield contour is therefore proportional to the difference in the stream function between any point on the shield and any point on the driven element when it is driven by a unitary current. Similarly, the mutual inductance per unit length will be proportional to the difference in the stream function between any point on the shield and any point on a non-driven element. Analytic expressions for the inductances are cumbersome to obtain, but numerical results are readily calculated using high-level programming languages such as MATLAB®.

4.2 General Comments on the Calculation of Modal Currents

As discussed in §1.3.2 for the case of a circular TEM coil, a circulant inductance matrix will produce modal currents that vary (co)sinusoidally around the circumference when the termination capacitances are all equal. However, for an oval TEM coil it is impossible for the inductance matrix to be circulant because the number of axial symmetry planes is reduced to two from $2N$ in the case of the circle. It is also plausible that the termination capacitances cannot be all equal if they are to produce the proper current distributions at the desired frequency. Therefore it is not possible to use the basis that diagonalises the inductance matrix to determine the currents at resonance because the reflection matrix (Eq. (1.8)) in modal coordinates would no longer be diagonal, indicating that several *propagation* modes are involved in producing the current and voltage pattern of a single *resonant* mode. The currents at resonance directly influence the homogeneity of the field produced by the resonator and therefore, with the modes' resonant frequencies, they are important variables that must be controlled for the satisfactory design and operation of an oval TEM

resonator.

To determine the correct basis for the resonant modes, it is sufficient to note that, in general, it is Eq. (1.9) that determines the distribution of currents at resonance, and therefore it is the product $\mathbf{Z}_{0,m}\mathbf{Y}_{L,m}$ that must be diagonal. To isolate the *resonant* modes of the TEM coil, the transformation matrix $\mathbf{T}$, whose columns contain the modal current or voltage distributions, must be chosen so that it diagonalises the product $\mathbf{LE}$, where $\mathbf{E}$ is the matrix containing the capacitances that terminate the two ends of the coil.

In order for $\mathbf{LE}$ to produce the modal currents that optimise field homogeneity, several constructive parameters may be varied. Bear in mind, however, that this matrix product need not be perfectly circulant, as that would impose restrictions on the current distributions and eigenvalues of the higher-order modes that are not useful in NMR applications. Firstly, the radii of the rods may be adjusted to equalize the diagonal terms of the inductance matrix. The terms off the diagonal are much less sensitive to the dimensions of the rods, but it is conceivable that small changes in the shape of the shield could be utilised to adjust the mutual inductances between elements. For example, conducting fins protruding into the cavity from the shield can modify the field lines locally, and therefore the amount of flux between each element and the shield may be adjusted. Mechanical adjustments for depth and orientation of the fins would allow for fine-tuning of the mutual and/or self-inductances depending on the fins' positions, but this solution may be excessively costly to implement and therefore may have limited applicability.

It is also possible to vary the positions of the elements on the circumference of the oval to fine-tune the mutual inductances. However, if the elements are no longer in the positions determined by Eq. (3.8) that allow the sinusoidal and cosinusoidal current distributions to produce highly uniform fields, new optimal current distributions will need to be determined for the new positions.

Possibly the simplest method of imparting some of the desired properties on the

product **LE** is to vary the capacitive loads at the cavity ends. Similarly to the inductance matrix, the terms of the diagonal matrix **E** are readily varied as they correspond to the capacitances between the rods and the shield. The terms off the diagonal are normally zero for a TEM resonator, but some may be introduced if necessary by creating connections *between* the elements similarly to the birdcage coil (c.f. Chapter 5).

4.3 An Oval TEM Coil Designed for Linear-Mode Operation

The simplest oval TEM coil design involves using only one of the two field modes that produce uniform fields. Naturally, the mode having the higher geometric sensitivity, namely the one whose field is parallel to the oval's major axis, should be used to take full advantage of the benefits of a tailored coil.

Design of such a coil was performed by numerical optimisation (MATLAB® function `fminsearch()`) by varying the radii of the coil elements concurrently with the termination capacitances in order to minimise the RMS difference between the actual and the ideal (sinusoidal) current distribution of the useful mode. For a coil having $N = 16$ elements, the number of unknown capacitances and radii is $N/2 - 2 = 6$ when two-fold symmetry without elements on the coil axes is exploited (one capacitance and one radius are maintained constant). The cost function also contained a term that kept the frequency of the modes adjacent to the one of interest as far away as possible. This is important in practice, given the wide resonance bandwidth of a loaded coil, to avoid coupling power to modes that do not produce the uniform fields required for in-vivo NMR. A third term was introduced in the cost function to prevent the radii of the elements from deviating excessively from the radius of the first element, as it was found that the algorithm often chose very different radii even though the benefits to the current distribution were minimal.

element	1	2	3	4
radius [mm]	8.0	11.8	7.4	8.6
capacitance [pF]	6.7	8.7	6.0	6.4

Table 4.1: Element radii and termination capacitances needed for linear operation of the Cassinian TEM body coil having a length of 60 cm, access diameters 25.8 × 51.6 cm and shield diameters 40 × 60 cm. Elements are numbered from the one closest to the major axis and values for the remaining 12 elements are obtained by symmetry.

Frequency [MHz]	114.3	120.3	128.1	131.5	138.3	139.3	143.3
Mode Order	0	1	1	2, 2	3	3	4
Frequency [MHz]	146.0	148.0	150.5	151.3	155.3	155.4	162.1
Mode Order	4	5	5	6	6	7	7, 8

Table 4.2: Resonant frequency and order of each mode of the Cassinian TEM body coil optimised for linear operation.

The transverse dimensions of the coil were chosen to accommodate the pelvic and abdominal regions (access diameters 25.8 × 51.6 cm and shield diameters 40 cm × 60 cm) and the length was chosen to be 60 cm. With these transverse dimensions, the expected improvement in geometric sensitivity over a circular coil having the same diameters as the major diameters of the Cassinians is 81% (c.f. Eqs. (2.24a) and (3.15)).

The element radii and termination capacitances determined upon convergence of the optimisation algorithm for resonance at 128 MHz are listed in Table 4.1. The final resonance spectrum of the coil is given in Figure 4.2 and the modes' respective orders and frequencies are listed in Table 4.2. The modal currents of the two modes of order one are shown in Figure 4.3, where it is evident that only the current distribution of the major-axis mode is optimal because the minor-axis mode is not used. Field lines and amplitude contours for that mode, shown in Figure 4.4, indicate that a high degree of homogeneity is achievable.

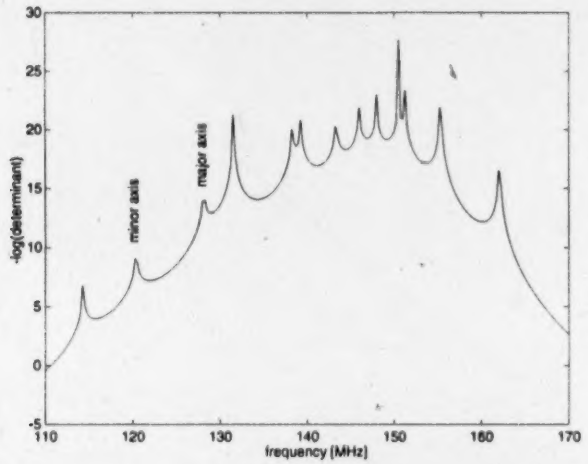

Figure 4.2: Resonance spectrum of the Cassinian TEM body coil having $N = 16$ elements and optimised for linear-mode operation. The major-axis mode is tuned to the 3T proton frequency (128 MHz), while nearby modes are kept as far from it as possible to avoid potential coupling under loaded conditions.

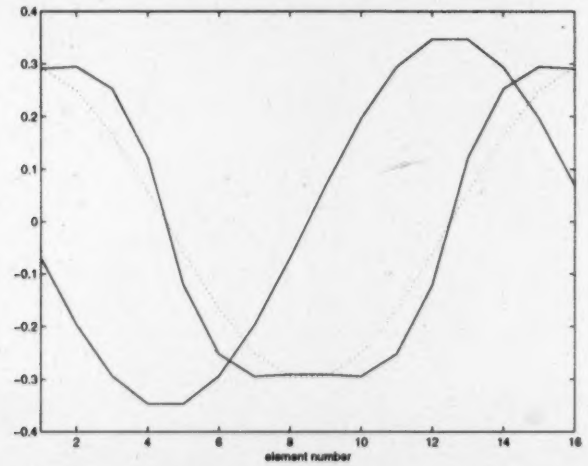

Figure 4.3: Current distributions for the two mode 1 resonances (solid lines) and the ideal distributions they seek to approximate (dashed lines). The distribution of the major-axis mode (sinusoidal current distribution) is nearly ideal while that of the unused minor-axis mode is allowed to deviate from the ideal cosinusoidal distribution.

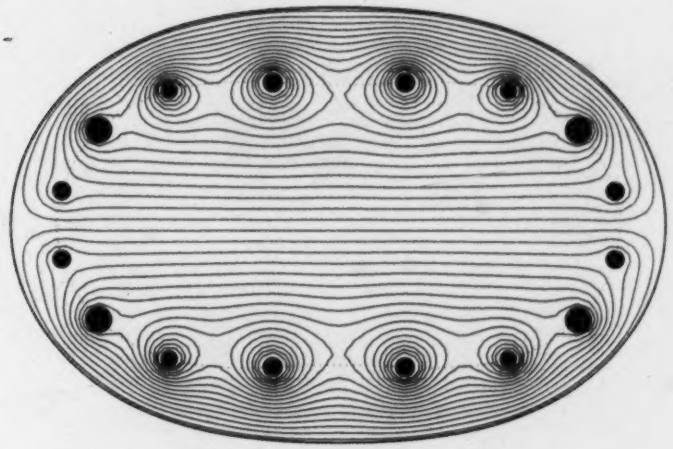

(a) Field Lines

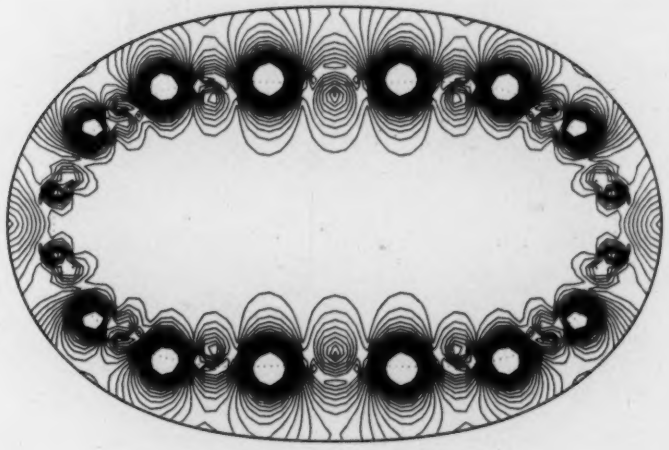

(b) Field homogeneity (10% intervals)

Figure 4.4: Magnetic field produced by the major-axis mode 1 resonance of the linear TEM body coil. a) field lines and b) field amplitude contours in the positively-rotating frame of reference [6] illustrate the high degree of homogeneity that is obtained.

4.4 A Quadrature Oval TEM Coil

A similar optimisation was undertaken to produce a quadrature coil having the same dimensions as the linear coil of the previous section. In addition to the coil elements' radii and termination capacitances, the positions of the elements on the circumference of the Cassinian were also variables in this optimisation, as it was found that without them the algorithm could not converge to a design in which the two modes of order one were degenerate. Consequently, the cost function did no longer measure the deviation of the elemental currents from the ideal sinusoidal pattern, but rather the RMS field amplitude variation over a 21 × 21 rectangular sampling grid centered on the coil axis and measuring 34 × 14 cm. The field was calculated as indicated in §4.1 based on the modal currents determined with the method of §4.2. As a consequence of the increase in the number of variables to $3N/4 - 2$, the number of coil elements was reduced to $N = 12$ to accelerate the convergence of the optimisation. Terms were included, as was done for the linear coil, to keep the frequencies of the modes adjacent to the two useful modes as far away as possible, and to limit the range of element radii.

The element radii and capacitances determined by the optimisation algorithm for resonance at 128 MHz are listed in Table 4.3. The final resonance spectrum of the quadrature coil is given in Figure 4.5 and the modes' respective orders and frequencies are listed in Table 4.4. The modal currents of the two modes of order one are shown in Figure 4.6, and the field lines and homogeneity of the resultant quadrature field are shown in Figures 4.7 and 4.8. These plots indicate that field homogeneity is sacrificed somewhat in order to permit the two resonant frequencies to coincide, but the gain in SNR obtainable using a quadrature probe may justify this loss in particular applications such as cardiac imaging.

element	1	2	3
angular location θ_n [rad]	0.255 (0.262)	0.789 (0.785)	1.35 (1.31)
radius [mm]	10.0	10.1	9.9
capacitance [pF]	7.3	7.6	7.6

Table 4.3: Angular locations in the circle plane, element radii and termination capacitances needed for quadrature operation of a Cassinian TEM body coil having a length of 60 cm, access diameters 25.8 × 51.6 cm and shield diameters 40 × 60 cm. Values for the remaining 9 elements are obtained by symmetry.

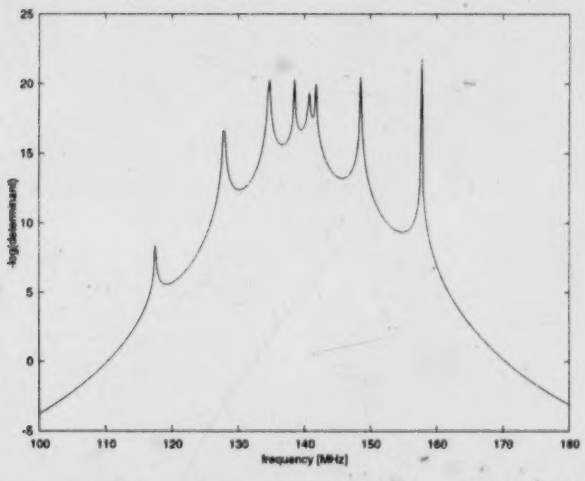

Figure 4.5: Resonance spectrum of the Cassinian oval TEM coil having $N = 12$ elements and optimised for quadrature operation. The two mode 1 frequencies are tuned to the 3T proton frequency (128 MHz), while nearby modes that produce inhomogeneous fields are kept as far away as possible to avoid potential coupling under loaded conditions.

Frequency [MHz]	118	128	135	139	141	142	149	158
Order	0	1, 1	2, 2	3	3	4	4, 5	5, 6

Table 4.4: Resonant frequency and order of each mode of the Cassinian TEM body coil optimised for quadrature operation.

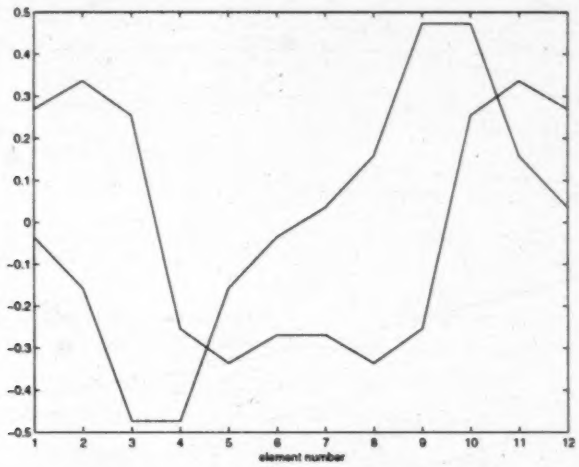

Figure 4.6: Current distributions for the two mode 1 resonances of the quadrature oval TEM coil. The ideal distributions are *not* sinusoidal because the locations of the elements are not the same as those determined previously by conformal mapping.

4.5 Discussion

In this chapter we have demonstrated how to apply multiconductor transmission line theory to predict the resonant behaviour of TEM coils constructed on cylindrical surfaces that are not circular in cross section. Prior work in this area [3] has focussed on the elliptical cross section but the Cassinian oval offers an improved geometric match to numerous parts of the human body (c.f. §3.1.3). An experimental validation of these methods should be the object of future investigations.

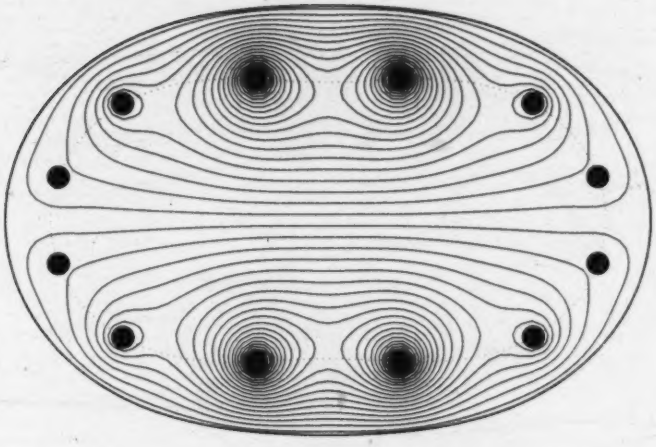

(a) Major-axis mode

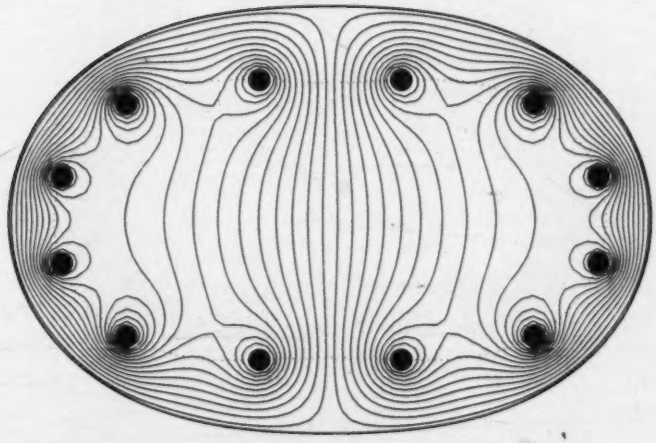

(b) Minor-axis mode

Figure 4.7: Field lines of the two mode 1 resonances of the quadrature oval TEM body coil.

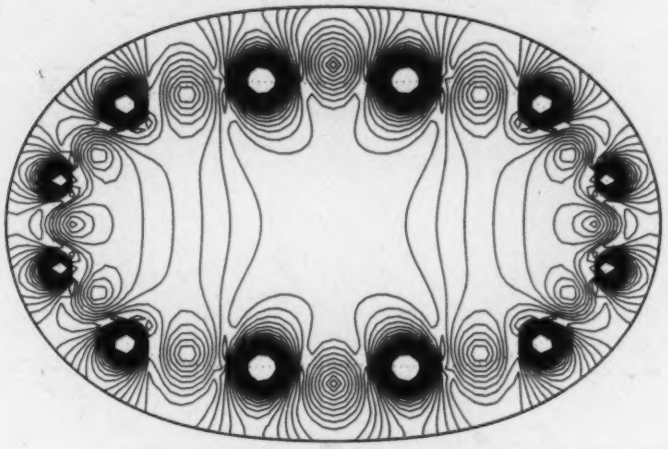

(a) B_1^+ Field homogeneity (10% intervals)

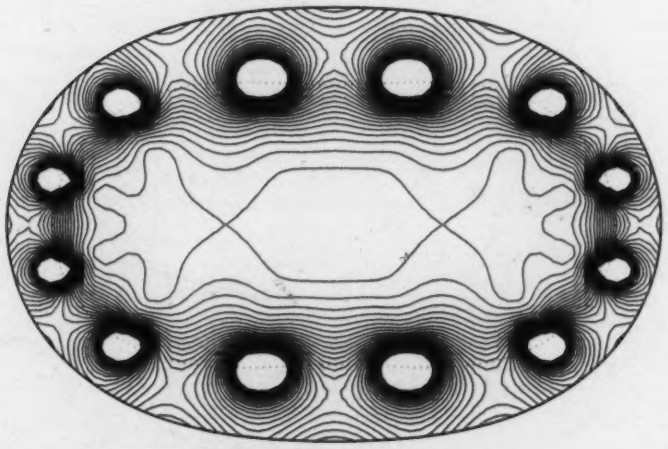

(b) B_1^- Field homogeneity (10% intervals)

Figure 4.8: Rotating-frame field amplitude contours of the quadrature oval TEM coil, calculated according to formulas [14] and [15] of ref. [6]. a) indicates the field homogeneity in the positively-rotating frame of reference, while b) is that in the negatively-rotating frame.

Bibliography

[1] Mark C. Leifer. Theory of the quadrature elliptic birdcage coil. *Magnetic Resonance in Medicine*, 38:726–732, 1997.

[2] Brian A. Baertlein, Ö. Özbay, T. Ibrahim, R. Lee, Y. Yu, A. Kangarlu, and P.-M. L. Robitaille. Theoretical model for an MRI radio frequency resonator. *IEEE Transactions on Biomedical Engineering*, 47(4):535–546, 2000.

[3] Patrick J. Ledden, Lawrence L. Wald, J. Thomas Vaughan, and Denise Hinton. A detunable elliptic transmission line resonator for body imaging at 3T. In *Proceedings of the International Society for Magnetic Resonance in Medicine, Eighth Annual Meeting*, volume 1, page 146, 2000.

[4] S. Ramo, J.R. Whinnery, and T. Van Duzer. *Fields and Waves in Communication Electronics*. John Wiley, New York, third edition, 1994.

[5] W.R. Smythe. *Static and Dynamic Electricity*. McGraw-Hill, New York, third edition, 1968.

[6] David I. Hoult. The principle of reciprocity in signal strength calculations—A mathematical guide. *Concepts in Magnetic Resonance*, 12(4):173–187, 2000.

Chapter 5

A High-Frequency Model of the Birdcage Coil

Analytic models of the birdcage coil that are discussed in the literature usually consist of lumped-element circuits and therefore require the assumption that the wavelength be much larger than the dimensions of the coil itself. However, with the recent increases in $\mathbf{B_0}$ field strengths of in-vivo NMR systems, birdcage coils have been constructed to operate at frequencies of 200 MHz and above [1], where this assumpion is no longer valid. At 200 MHz the free-space wavelength is 1.5 m, and the dimension of one quarter-wavelength, which in transmission-line theory is known to invert the termination impedance, are easily exceeded in a body coil. Consequently, a certain degree of iteration based on empirical observations is required to determine, for example, the capacitance values that will produce resonance at the desired frequency.

A model that is able to account for the finite propagation speed of electromagnetic waves would be useful not only to facilitate the engineering of birdcage coils, but also to gain a clearer understanding of their high-frequency operation. It has been noted [2] that variations in B_1 field intensity along the axis of the coil are determined by its axial propagation constant, k_z, causing the currents on the legs of the birdcage coil to vary along their lengths. For a high-pass coil, for example, a current maximum occurs at the central transverse plane of a symmetric coil, concurrently with an electric

field minimum [3], while the currents taper off toward the ends of the coil as $\cos k_z z$ and are ideally null at a distance of one-quarter wavelength from the central plane (the origin of the axial coordinate, z). This effect consequently limits the maximum practical length of a birdcage coil at a given frequency to a small fraction of the axial wavelength because the magnetic field amplitude also tapers off toward the ends of the coil with the same cosinusoidal dependence. A method to reduce the limitation in the useable length of the birdcage coil is to fill the space between the coil and shield with a material having high electric permittivity [4], or to use a low-pass or hybrid birdcage topology [2]. However, both of these techniques create axial *electric* fields by introducing, respectively, additional boundary conditions at the surface of the dielectric, or voltage discontinuities across the leg capacitors, thus contributing to losses that should in practice be minimised (c.f. §6.4.3). A more accurate high-frequency model of the birdcage is needed to evaluate the electromagnetic field distribution of such designs, while overcoming the limitations of existing high-frequency models [2, 5] which are not able to account for the effects of strong electromagnetic coupling between the coil's longitudinal elements. Modal analysis performed using these models is accurate only when such coupling can be neglected (e.g., when the elements are very close to the shield or far from each other). Numerical methods of performing modal analysis [6] are notoriously slow and are therefore impractical for design methods that require numerous design iterations before a result is obtained.

The practical uses of a high-frequency model of the birdcage coil are to extend its useful frequency range into the range currently occupied by the TEM resonator and to study methods to extend the maximum practical length at a given frequency. One advantage that the birdcage enjoys over the TEM coil is a simpler tuning procedure, which can reduce the overall production cost of such probes.

5.1 Multiconductor Transmission Line Model

The similarities between birdcage and TEM coils has been known for some time and an early application of transmission line theory to predict their resonant frequencies can be found in ref. [7]. However, the researchers who subsequently perfected the multiconductor transmission line model (see ref. [8], as well as Section 1.3.2) by including the mutual couplings between longitudinal elements state that such a model is not applicable to the birdcage coil. In fact the multiconductor transmission line model can be applied to the shielded birdcage coil with some minor modifications to the termination admittance matrix (see Eq. (1.8) et seq.). In the case of the TEM coil, this matrix is diagonal since each element is connected only to the shield. In the birdcage coil, however, each element is connected to the two elements adjacent to it by inductive segments (low-pass configuration) and capacitors in the high-pass and band-pass configurations. If the coil is close enough to the shield, the mutual inductances between segments of an end-ring may be neglected because the shield strongly limits the spatial extent of the magnetic field of each segment. Naturally, the mutual inductances between end-ring segments at opposite ends of the coil are also negligible. The termination admittance matrix at the end ring therefore becomes

$$\mathbf{Y}_L = Y_{er} \begin{bmatrix} 2 & -1 & 0 & \dots & 0 & -1 \\ -1 & 2 & -1 & 0 & \dots & 0 \\ 0 & -1 & 2 & -1 & \dots & 0 \\ \vdots & & & \ddots & & \vdots \\ 0 & \dots & 0 & -1 & 2 & -1 \\ -1 & 0 & \dots & 0 & -1 & 2 \end{bmatrix}, \tag{5.1}$$

where Y_{er} is the total admittance of each end-ring segment, including both inductive and capacitive parts. Here we have also exploited the symmetry of the circular coil and factored out Y_{er} from the matrix, although this step is not valid in general. In the case of a high-pass coil, it is now sufficient to apply Eqs. (1.7–1.9) directly to obtain the resonance spectrum, bearing in mind that Y_{er} will be a function of frequency. A sample resonance spectrum obtained in this manner for a high-pass birdcage coil

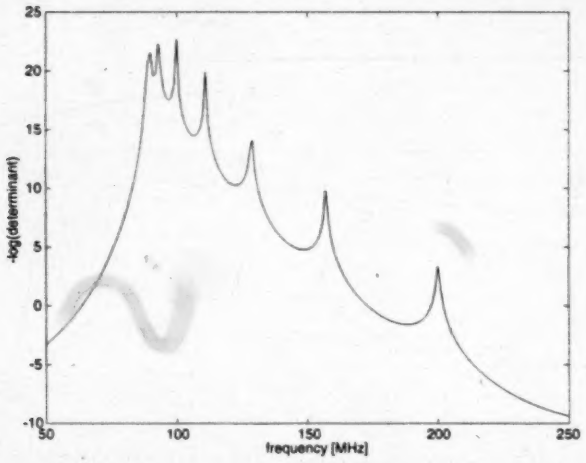

Figure 5.1: Resonance spectrum of a high-pass birdcage coil designed to operate at 200 MHz. The end-ring resonances (not shown) are at 233 MHz.

is shown in Figure 5.1. Its constructive parameters are $N = 16$, $l = 20$ cm, 33cm shield diameter, 28cm coil former diameter, and 8mm-diameter copper rods for the ladder network. For operation at 200 MHz, 16.9pF capacitances are required at the end rings, and the inductance matrix is calculated similarly to §4.1 but without the transformation for the oval shield.

For low-pass or band-pass topologies, where capacitors are placed in series with the coil's legs at the centre of each leg, the symmetry of the coil with respect to the central transverse plane will also need to be exploited. If the leg capacitors are split into two capacitors having double the original capacitance and connected in series, the points between all capacitor pairs will be at virtual ground, and therefore these points can be considered to be shorted to the shield. The modal problem is consequently reduced to that of a coil of half the original length, l, having a different termination matrix at each end. The termination at the end ring will have an admittance matrix given by Eq. (5.1), while the capacitors at the middle of the coil will have a diagonal admittance matrix identical to that of a TEM coil, but where a capacitance of double

the actual value is used so that the series combination of the two capacitances will yield the correct value. The condition for resonance will also need to be modified to

$$\left|\mathbf{1}_N - \mathbf{\Gamma}_{er,m}\mathbf{\Gamma}_{c,m}e^{-i\omega l/c}\right|, \tag{5.2}$$

where $\mathbf{\Gamma}_{er,m}$ and $\mathbf{\Gamma}_{c,m}$ are the modal reflection matrices at the end-ring and central plane, respectively.

5.2 The Band-pass Circular Birdcage Coil Prototype

The methods of the previous section were used to model a circular head coil that is routinely used for 3T proton imaging, and was constructed as a standard for comparison with the Cassinian oval coil (c.f. Chapter 3).

Although the coil is constructed using 6mm-wide copper strips, the inductance per unit length matrix, $\mathbf{L}$, of the circular multiconductor line was calculated assuming the legs to be circular in cross section, with a radius of 1.53 mm determined empirically from the simulations with NEC-2 of §3.2.2. The end-ring inductance was calculated by considering the segment to be over a conducting plane, although its radius was adjusted to 2.1 mm to give an end-ring resonance of 148 MHz that corresponds to the value measured on the bench. Capacitor values (c.f. Table 3.1) are 33 pF in the end rings and 220 pF in the legs of the coil. Simulated and measured resonance spectra of the coil are in good agreement as can be seen in Figure 5.2. In fact, the predicted frequency of the modes of order one are exactly on the mark at the 3T proton frequency, 128 MHz.

5.3 Concluding Remarks

This chapter has shown that multiconductor transmission line theory can be used to model with accuracy the resonance of a birdcage coil, in contrast to the beliefs of

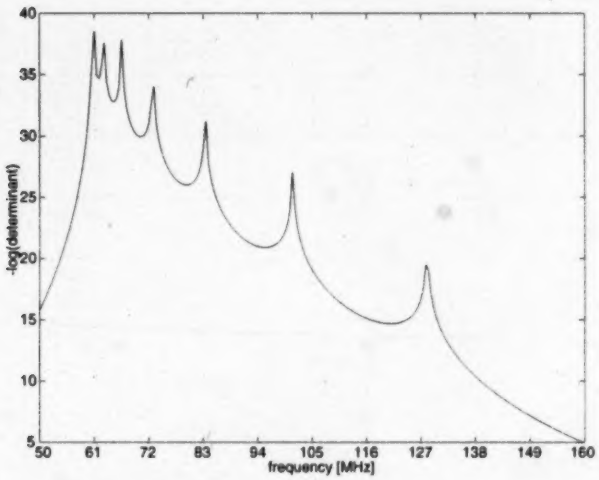

(a) Simulated spectrum (end-ring resonance not shown)

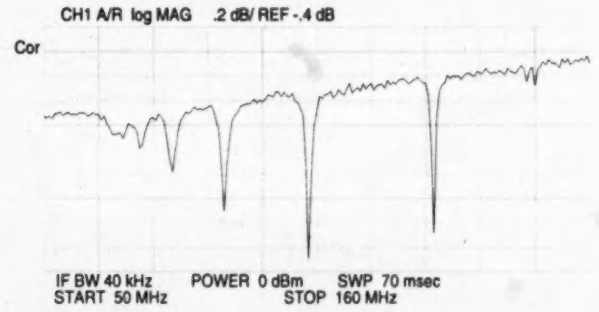

(b) Return loss (S_{11}) measurement using inductive coupling

Figure 5.2: Simulated, a), and measured, b), resonance spectra of the circular hybrid birdcage coil prototype designed to operate at 128 MHz. Excellent agreement is observed in the resonant frequencies, especially those of the useful modes of order one.

other researchers [8]. While there are unquestionably some non-TEM fields produced in the birdcage coil, if the shield is closely coupled to the coil such fields do not extend appreciably into the central region of the coil and their effect can therefore be accounted for by using lumped elements. The lumped elements at the two ends of the coil form the two termination networks of a multiconductor transmission line in which the fields *are* TEM, similarly to the TEM resonator.

Although the implementation illustrated here does not account for any mutual inductances between end-ring segments, the termination admittance matrix could be modified to include such couplings if further precision were required. The fact that end-ring inductances are assumed to be lumped elements is a valid approximation since the electrical length of an end-ring segment will be much less than the wavelength in most in-vivo applications.

Bibliography

[1] F. David Doty, Jr. George Entzminger, Cory D. Hauck, and John P. Staab. Practical aspects of birdcage coils. *Journal of Magnetic Resonance*, 138:144–154, 1999.

[2] Thomas K.F. Foo, Cecil E. Hayes, and Yoon-Won Kang. An analytical model for the design of RF resonators for MR body imaging. *Magnetic Resonance in Medicine*, 21:165–177, 1991.

[3] Peter M. Joseph and Mohamed Saadi-Elmadjra. Electric field measurements in cylindrical imaging coils. *Journal of Magnetic Resonance*, 75:199–212, 1987.

[4] Thomas K.F. Foo, Cecil E. Hayes, and Yoon-Won Kang. Reduction of RF penetration effects in high field imaging. *Magnetic Resonance in Medicine*, 23:287–301, 1992.

[5] P. Mansfield, M. McJury, and P. Glover. High frequency cavity resonator designs for NMR. *Meas. Sci. Technol.*, 1:1052–1059, 1990.

[6] Jianming Jin. *Electromagnetic Analysis and Design in Magnetic Resonance Imaging.* CRC Press, New York, 1999.

[7] Peter Röschmann. Analysis of mode spectra in cylindrical n-conductor transmission line resonators with expansion to low-, high- and band-pass birdcage structures. In *Proceedings of the International Society for Magnetic Resonance in Medicine*, page 1000, 1995.

[8] Brian A. Baertlein, Ö. Özbay, T. Ibrahim, R. Lee, Y. Yu, A. Kangarlu, and P.-M. L. Robitaille. Theoretical model for an MRI radio frequency resonator. *IEEE Transactions on Biomedical Engineering*, 47(4):535–546, 2000.

Chapter 6

Probe Construction and Measurement of Performance

In this chapter I have collected information about the actual construction and testing of NMR probes. Although there is no single reference that covers all the practical aspects of modern NMR probe realisation, Chen and Hoult's *Biomedical Magnetic Resonance Technology* [1] does include a wide variety of valuable information. Also, due to the numerous analogies that exist between telecommunication antennas and NMR probes, many of the same principles and circuits apply and indeed have been introduced to NMR from such texts as Terman's *Electronic and Radio Engineering* [2] or the American Radio Relay League's *Handbook for Radio Amateurs* [3].

6.1 Coil Construction Methods and Materials

The methods of constructing NMR probes may differ considerably depending on the particular application and the institution's philosophy. The suggestions that follow, however, should be applicable rather generally for probes used in *in-vivo* applications. One rule that applies to all materials used in probe construction is that no ferromagnetic materials must be present. In order to avoid unpleasant surprises later, it is a good habit to test all components that contain metal using a permanent magnet to uncover the tell-tale attraction. Ferromagnetic materials are used in everything from

coaxial cables and connectors to the leads on capacitors and other components, but some manufacturers do have guaranteed NMR-friendly components in their product lines.

6.1.1 Mechanical Support

Most NMR probes will need to be built on an electrically insulating frame to provide mechanical support for the coil's components as well as to prevent the patient from coming into direct contact with the conductors. This could be quite a dangerous situation because of the possibility of causing burns given the high peak powers (up to several kilowatts), and consequently high voltages, required for NMR on the human body. Furthermore, to reduce the chance of causing claustrophobia, or to provide access to equipment for visual stimulation for fMRI (see §1.2.3), head coils are often constructed on transparent formers, or formers that have suitable openings to allow the patient a view beyond the usually closely-fitting head coil.

The support should not only be an insulator, but it should also produce little or no NMR signal of its own lest it corrupt the experiment (acrylic plastics are often avoided for this reason), and have a small loss tangent [4, §6.4] to minimise dielectric losses. Common materials used are polycarbonate plastic (Lexan ®) and the various types of inexpensive printed circuit board, on which copper traces can easily be produced. The thickness of the backing material will depend on whether the particular application requires a flexible coil (e.g., a surface coil) or a rigid former. Foam padding is also used for patient comfort as well as to maintain a minimum distance between coil and patient. In fact, if the patient comes too close to the coil, the strong coupling can lead to malfunctioning of the coil, or, worse, to excessive tissue heating (SAR).

For clinical applications, regulatory agencies often require the materials to be flame resistant as a further protection for the patient against possible malfunctions (e.g., short circuits).

6.1.2 Conductors: Resistance and Inductance

Although the material used for the conducting portions of the coil is almost exclusively copper, either in the form of rods, bars, adhesive strips, or bonded to circuit board material, some comparisons to other metals are in order. The conductivity of copper is second only to silver at room temperatures [5, Table B.1], but it is preferred because of its superior resistance to corrosion and lower cost. Gold is more resistant to corrosion than copper but its prohibitive cost and lower conductivity limit its use to places such as contact surfaces. Superconducting probes have also been built [6], but they present numerous challenges because of their need for cryogenic refrigeration.

Another metal often found in NMR probes is solder (lead-tin alloy), and unfortunately its conductivity is only 12% that of copper. Given the small quantities generally used by a skilled solderer, its contribution to the total losses in the conductors may not seem important. However, because of the skin effect [5, pp.193-200], excessive coating of the copper conductors with solder can substantially increase the resistance seen by the RF current. It is therefore important not to use more solder than is necessary to maintain a good mechanical and electrical connection, especially in low-field and microscopy applications where probe losses tend to be dominant [7].

The conductors play an important role in the magnetic energy storage required for the resonant behaviour of an NMR probe. Their transverse dimensions determine the inductance per unit length which can be varied to adjust the resonant frequency. If using copper strips or printed circuit board, an increase in inductance is readily achieved by trimming the edges of the conductive traces with a sharp hobby knife to make them narrower. This tuning method can be much cheaper than varying the capacitive portion of the circuit because it does not require additional components, especially variable capacitors that for NMR applications are particularly expensive and are subject to failure when high power pulses are applied. Of course, by this method tuning is not easily reversed and therefore is suitable for coarse adjustments.

As pointed out by Link [8, §4.3], it is desirable to use the widest possible copper

conductors, not only to reduce resistance, but also to reduce inductance and consequently the voltages and electric fields in the probe. It should be borne in mind, however, that the skin effect will tend to concentrate the current at the edges of wide copper strips, therefore producing a magnetic field that is not identical to that produced by a single filamentary current.

6.1.3 Capacitors

Discrete capacitors are important components that must be chosen carefully in order to obtain the best performance from the probe. Their quality is represented by several parameters that should be listed in the technical documentation provided by the manufacturer. Firstly, the capacitor's breakdown voltage should be sufficiently high to prevent damage during transmission. The maximal voltages produced in the probe depend on the transmitter power as well as the circuit topology and the values of other circuit parameters such as inductance and resistance. If the probe is used only for reception, its capacitors may still be subjected to considerable voltages induced by magnetic coupling with the transmitting coil. The highest voltages are often present in series-resonant circuits such as those used for impedance matching, where it is not uncommon to see low-quality capacitors fail after the first use.

Another important parameter is the capacitor's equivalent series resistance, R_{es}, or similarly the quality factor $Q \triangleq X_C/R_{es} = 1/\omega C R_{es}$, which is numerically high for a low-loss component. Lossy capacitors not only introduce noise on reception, but can actually generate heat during transmission when high-power pulses are sent to the coil. Increased temperatures can lead to failure, as well as to observable thermal drifts of the resonant frequency if the thermal coefficient is not sufficiently low. Capacitors for NMR probes usually have a ceramic or porcelain dielectric because of its low loss tangent and thermal stability. Since high currents are often present in parallel resonant circuits, commonly used for impedance matching, trap circuits, etc., it is especially important that they use low-loss capacitors as they can considerably

contribute to the coil's overall losses.

The tolerance in the capacitance value is important in probes such as the birdcage coil, where any asymmetry will degrade quadrature performance and field uniformity. In such situations it is not necessary, however, to go to the expense of buying capacitors with the best tolerance, which in any case is usually not better than 1%, because it is not the absolute capacitance that needs to be accurately controlled, but rather the *differences* between capacitors that are more important to maintaining symmetry. Fine tuning of the coil frequency can be accomplished by other means, such as with variable capacitors at the coil's ports. It is possible to reduce random variations in a given set of capacitors by buying more than necessary, measuring their capacitance at a frequency near that of operation, if possible, and sorting them into groups having sufficiently close values. Another method is to connect several capacitors of the same nominal value in parallel, thus effectively reducing the statistical variability (standard deviation) by the square root of the number of capacitors.

Capacitors are usually made for either surface mounting or for thru-hole mounting on printed circuit boards. The former, also known as "chip" capacitors because of their small parallelepiped shape, have solder pads on their sides or bottom, while the latter have flexible wires that protrude from a disc-shaped body. While wire leads make measuring and soldering operations easier, they introduce a series inductance that cannot be neglected, especially at frequencies above 100 MHz, and is difficult to model and account for in the design stage. A coil whose leaded capacitors are replaced by chip capacitors of the same nominal value may indeed resonate at a higher frequency because of the reduced inductance. It is therefore important, if leaded capacitors are to be employed, to keep the leads as short as possible and to keep the length consistent if several capacitors are used. This will minimise the chances of the lead inductance affecting coil operation unpredictably.

6.2 Shielding and Grounding

The purpose of shielding an NMR probe is to isolate it from the rest of the NMR system (mostly the gradient coils) and to prevent far-field radiation by providing stable and controlled boundary conditions [7, 8, 9]. Mechanical stability is required because the shield affects the coil's resonant frequency mainly by altering the inductive portions of the circuit relative to the unshielded coil, and therefore the coil must not be allowed to move inside the shield.

Ideally the shield should behave as an ideal conductor at the probe's frequency to minimise losses, but offer a high resistance at the frequencies at which gradient coils are switched (in the audio frequency range) to prevent the induction of eddy currents. This property can be achieved by using metal foil (e.g., phosphor bronze, titanium, etc.) of thickness roughly equal to the skin depth at the Larmor frequency, so that the RF currents experience a low resistance while the gradient eddy currents experience a high resistance. Similar behaviour can be achieved by using a segmented shield having capacitively-coupled overlapped sections that offer low impedance to RF currents and high impedance to gradient eddy currents [10]. If the RF current paths on the shield are well known, and differ substantially from the paths of the gradient eddy currents, they can be cut into the foil to create isolated loops where the RF currents can flow unhindered, while being completely transparent to gradient fields.

Another advantage of using an RF shield is that it can provide a ground reference for the probe and related circuitry. Grounding is important in all electronic circuits to reduce the effects of interference. In the case of NMR probes, a proper ground connection between the shield and the braid of the coaxial cable to which the probe is connected also ensures stable and predictable performance. Without such a connection the voltage between probe and shield would be allowed to fluctuate unpredictably as determined by stray capacitance and other parasitic effects, creating currents that flow on the *outside* of the coaxial cable braid if a shorter path to the

shield is not available. Currents on the outside of coaxial cables can dramatically reduce the quality factor (c.f. §6.4.2) of the probe, as well as introduce parasitic resonances or reactances. Sensitivity to cable positioning is often a symptom of the presence of such currents; another method to detect their presence is by the use of ferrite chokes or cable traps whose purpose is to introduce a high impedance in series with the shield currents. With the trap or ferrite choke placed on the cable as close to the probe as possible, the sensitivity to cable positioning will be reduced, and the effect of the missing cable reactance will be seen as a shift of the resonant frequency.

Cable traps are constructed by coiling a section of semi-rigid coaxial cable and shorting the resulting inductor with a capacitor [11, p.805] to produce a parallel resonance at the Larmor frequency. While cable traps can be used inside the bore of the NMR system, ferrites cannot because of their high magnetic permeability and nonlinear magnetic behaviour. If properly tuned they effectively eliminate cable currents because of the high impedance they introduce; however, the effect is useful only over a narrow relative bandwidth, while ferrite chokes do not provide an ideal open circuit but are effective over large frequency ranges. In either case the signal that travels inside the coaxial cable is not affected by what is done to the outside of its shield if the bend radius is kept large enough not to kink the cable.

It is good practice to make connections between the coil coupling circuitry ground (e.g., coax braid) and the shield at points where the voltage between coil and shield is minimal. Such a voltage nodal plane is found in the symmetric high-pass birdcage or TEM coil in the transverse plane half-way between the ends of the coil. Other practical considerations such as accessibility of the circuits from the coil ends often preclude the strict application of this rule, and undesired effects such as increased losses or coupling between modes can result from improper grounding.

6.3 Coupling Circuitry

The purpose of coupling circuitry is to allow the connection of the transmitter and receiver to the resonant circuit which produces the probe's useful field. The connection must be efficient so that power from the transmitter will be coupled to the probe without reflections, and also to produce the largest possible SNR at the output of the preamplifier.

Another fundamental requirement of such circuitry is that it must not alter the functioning of the resonant circuit (probe) in an undesired way. For example, one cannot connect the shield of a coaxial cable directly to a point of the circuit that normally has a fluctuating voltage, or its resonance frequency and current distribution will change.

In general, coupling arrangements can be described as electric (capacitive) or magnetic (inductive) based on which field is used to excite the probe's resonant circuit. Other tasks that the coupling circuits often perform are impedance transformations and/or changes in the symmetry of the driving voltage (symmetric to asymmetric or vice versa).

6.3.1 Electric Coupling

Electric coupling is achieved by producing a voltage in the resonant circuit (e.g., across a capacitor) by a direct cable connection or through a capacitor. Depending on the particular topology, the capacitor can also be used to adjust the input impedance and/or resonant frequency of the probe.

Electric coupling is often used in quadrature birdcage coils and some methods for providing such connections are given in ref. [12].

6.3.2 Magnetic Coupling

Magnetic coupling is accomplished by bringing a wire loop near the probe so that some magnetic flux coupling is established. The advantage that magnetic coupling enjoys over electric coupling is that the electrical balance of the coil can be maintained more easily since there is no direct connection between the coils. Furthermore, the voltages at the ends of the loop should be considered to be balanced so that the average voltage of the loop will be zero at all times. In this manner, if a stray capacitance exists between the loop and the probe there will likely be no net electric field coupling between the two structures. However, the current circulating in the coupling loop will itself produce a magnetic field that can degrade the overall field homogeneity of the probe, and therefore it is seldom used for volume coils. Furthermore, close coupling can alter the resonant frequency of the probe, a fact which must be taken into account in the probe's design stage.

The use of magnetic coupling is rare in modern quadrature coils not only because of the field produced by the loop, but also because of the difficulty of preventing magnetic coupling between the two loops at the two coupling ports. It is, however, the only viable method of coupling to superconducting probes [6].

6.3.3 Impedance Matching

Impedance matching is required at the ends of a transmission line to prevent power loss and signal distortion from multiple reflections of the waves that travel down the line. Numerous methods for performing impedance matching of any load impedance are discussed in the literature (e.g., ref. [13, §8.9]). Many utilise the concept of "quarter-wavelength" transformer, whereby a quarter-wavelength section of transmission line having characteristic impedance equal to the geometric mean of the load impedance (assumed to be real) and the desired impedance is inserted between the load and the rest of the transmission line. The fact that with a quarter-wavelength transformer the ideal matching condition occurs only in a narrow bandwidth is not

a problem for NMR applications because of the small relative bandwidths required. However, the use of actual transmission lines is impractical because commercially available cables are produced only with discrete values of characteristic impedance (usually 50 or 75Ω for coaxial cable), and the length of cable required for one quarter wavelength is often a cumbersome 1/2 metre or more.

Consequently, impedance matching is commonly performed using networks of discrete capacitors and inductors that simulate the effect of a quarter-wavelength transmission line (e.g., a Π or T network). The Smith chart is a common graphical tool used to determine the values of the various reactances on the network [14, Ch.10]. The choice of network topology is dependent on such factors as component availability, the value of the load impedance relative to that of the transmission line, whether the lines are balanced or unbalanced, etc. If inductors are needed, placement must be such that there will be as little flux coupling as possible between the inductors, including the probe itself.

6.3.4 Balance Transformers

The purpose of balance transformers (baluns) is to transform an unbalanced voltage that travels along an unbalanced transmission line (e.g., coaxial cable), where one conductor is always at ground potential, to a balanced voltage, where the signals on the two conductors of the balanced transmission line are equal and opposite in sign relative to ground potential, and vice versa. NMR probes are often driven using symmetric voltages to reduce the maximum voltage to ground and therefore the dielectric losses. Direct connections to coaxial cable can only be made in cases where the coil's topology and symmetry create a natural ground point to which the cable's braid can then be connected without fear of altering the probe's resonance. Baluns are also useful in preventing shield currents on the outside of coaxial cables.

Several distributed balun designs such as the loop balun are illustrated in ref. [1, Fig.4.15a)-d)]. Another design worthy of notice is the triaxial or "bazooka" balun,

[11, p.804] where a quarter-wavelength section of the outside shield of a triaxial cable is shorted to the inner shield *and grounded*, thus creating an open circuit condition between the two shields at the opposite end. The effect is to block shield currents flowing on the inner shield similarly to a cable trap (see §6.2), although the dimensions of cable baluns normally limit their use to the interconnections between the RF probe and the amplifier or receiver. Many other distributed balun designs are given in Chapter 23 of ref. [11].

Some more compact baluns that use discrete components are given in refs. [15, 16, 17] and [1, Fig.4.15e)]. Such circuits can often be used to accomplish additionally an impedance transformation such as that required for impedance matching, thus eliminating redundant components.

6.4 Bench Measurements

Most of the work of tuning and verifying the performance of a radio frequency probe can be carried out in an electronics workshop that is equipped at least with instruments such as a swept frequency generator and an oscilloscope. In fact, only after satisfactory performance is achieved on the bench should the probe be tested under realistic conditions with the NMR experiment for which it was designed, because NMR experiments rarely provide information on where a probe could be improved if the results are not satisfactory [8]. To facilitate the measurement process, modern instrumentation such as the vector network analyser should be used, along with a test set to perform insertion loss and return loss measurements at the frequency of interest. These highly automated instruments not only accelerate the measurement process over traditional measurements using a sweep generator, directional couplers and oscilloscope, but also reduce the possibility of introducing human error. As with any measurement device, however, care should be taken to allow it to reach its operating temperature and then an external calibration should be performed according to the instrument's documentation. This is required, for example, to compensate for

the propagation effects of the cables used to connect the probe to the analyser. Internal calibration of the instrument should also be performed regularly (e.g., yearly) by a laboratory approved by the instrument's manufacturer. This type of calibration involves verifying internal adjustments and requires the use of standards that are not readily available, and consequently can be rather costly.

6.4.1 Resonant Frequency

The measurement of resonant frequency of an NMR probe is typically performed by exciting the resonance by connecting the generator directly to the coil's output port or by coupling to the probe inductively using a test loop. A small pickup loop is used to detect the resonant response by placing it in the centre of the RF coil and orienting it to maximise flux linkage with the field mode of interest. In order to minimise the loading effect of the pickup loop, its diameter should be large enough to detect a reasonably strong signal, but not larger to prevent it from altering the measurement by excessively loading the probe. The frequency at which the signal picked up by the test loop is maximal corresponds to the resonant frequency.

It is also possible to measure the resonant frequency by using a single connection or coupling loop, i.e., by a return loss (S_{11}) measurement. In the latter case, at resonance the currents induced in the coil will increase the losses and therefore an S_{11} measurement will show a dip at the frequency corresponding to the coil's resonant frequency. In the case of a direct connection, the resonant condition is normally defined as the frequency at which the coil's input impedance is *real*. With a vector network analyser this condition corresponds to a reflected signal having zero phase shift with respect to the incident wave, i.e., lying on the horizontal axis when plotted on a polar diagram.

6.4.2 Quality Factor (Q)

The quality factor, Q, of a resonator is defined as [4, §5.14]

$$Q \triangleq \frac{\omega_0(\text{energy stored})}{\text{average power loss}}, \tag{6.1}$$

where ω_0 is the resonant angular frequency. It is readily shown that the quality factor is equal to the ratio of the resonant frequency to the 3dB width of the response curve (full width at half maximum). For NMR coils, the typical measurement setup involves connecting the coil to the generator as for the frequency measurement and using a pickup loop to detect the coil's response. Once the resonant frequency is recorded, it is divided by the distance between the two 3dB points ($1/\sqrt{2}$ of the maximum amplitude).

It is important to note that the value so obtained is affected by the loading due to the connections to the generator and probe. This loading can cause the measured Q to be less than the actual Q of the coil, therefore a means of correcting for these effects is required. We begin by recalling the property of the combination of quality factors due to different mechanisms of loss, e.g., resistive loss, coupling to a transmission line, losses in the sample, etc. The Q factors due to the single physical effects combine according to the formula [4, §5.14]

$$\frac{1}{Q_{\text{total}}} = \frac{1}{Q_1} + \frac{1}{Q_2} + \cdots \tag{6.2}$$

Let us also define the coupling factor, K, as the ratio of losses due to coupling to a transmission line to the losses within the coil (including sample losses if the coil is loaded) [18, Ch.9] [19],

$$K \triangleq \frac{Q_{\text{coil}}}{Q_{\text{ext}}}. \tag{6.3}$$

With the losses so divided, Eqs. (6.2, 6.3) combine to obtain the corrected value of the coil's quality factor,

$$Q_{\text{coil}} = (K+1)Q_{\text{total}}. \tag{6.4}$$

The coupling factor can be obtained from the measurement of the reflection coefficient, ρ, and the knowledge of whether the coil is over- or undercoupled to the transmission line,

$$K = \frac{1+\rho}{1-\rho} > 1, \; K = \frac{1-\rho}{1+\rho} < 1, \tag{6.5}$$

respectively. To determine in which of these two conditions it is operating it will be sufficient to observe what happens to the match if losses are increased or decreased, for example by introducing or removing a lossy sample from the coil. If the match gets better (worse) as coil losses are increased (decreased) the resonator is overcoupled, if it gets worse (better) as coil losses are increased (decreased) the resonator is undercoupled. At critical coupling ($K = 1$) the measured Q is exactly half of the coil's real Q.

6.4.3 Damping Factor, Efficiency and Dielectric Loss

An important indicator of coil performance that can be measured on the bench is the Q damping factor, r. It is defined as the ratio of the probe's Q without a sample, to the Q with a sample in the coil. This parameter is an indicator of the coil's sensitivity to loading and it should be as high as possible when a magnetically lossy or conductive sample, such as physiological saline, is introduced. With an electrically lossy non-conductive sample, however, the reduction in Q should be *minimal* [20, 8, p.27]. If this is not the case the probe is producing electric fields that are too strong and need to be minimised, for example by the use of electrical shielding.

Similarly, coil efficiency, η is defined as the ratio of the losses in the sample to the total losses, and can be calculated from the unloaded and loaded Q's as [21]

$$\eta \triangleq \frac{1/Q_{\text{loaded}} - 1/Q_{\text{unloaded}}}{1/Q_{\text{loaded}}} = 1 - \frac{1}{r}. \tag{6.6}$$

Ideally it should be equal to one, but generally for a given coil configuration it can be expected to increase with increasing frequency of operation as the losses in the coil conductors become negligible compared to the losses in the biological sample.

6.4.4 Input Sensitivity

The bench measurement of coil input sensitivity (Eq. (1.10b)) can be performed by using a small pickup loop that has been carefully shielded and balanced to prevent coupling to the electric fields produced by the coil [22]. Another method employs a more elaborate dual-loop probe but does not require a physical connection to the coil, which is convenient in the initial stages of construction [23]. At the high frequencies of operation of many modern probes, however, electric pickup is difficult to eliminate and an indirect measurement using NMR may be preferred (c.f. §6.5.1).

6.4.5 Port Isolation

In coils such as surface coil arrays or quadrature volume coils, it is desirable that the coupling between coil ports be as small as possible to ensure proper operation. In the case of quadrature coils an imperfect port isolation will lead to an elliptically polarised magnetic field. In array coils, coupling can lead to alterations in the coils' resonant frequencies as well as introducing correlation between the signals and noise components that are received by coupled coils [24].

Port isolation is measured by setting up the network analyser to perform an S_{21} measurement between the two ports. It should be noted that in general, the isolation will vary with loading and therefore it should be measured under realistic loading conditions.

6.5 NMR Measurements on Phantoms

Once the bench measurements are satisfactory the probe's performance can be verified in the NMR scanner by performing some appropriate experiments.

6.5.1 Field Mapping with Small Samples

In the case of coils designed for the proton frequency, a small (e.g., 1 ml) spherical sample of slightly doped water can be used to test the B_1 field amplitude, and polarisation distribution in the empty coil. Although performance of the empty coil is not an accurate indication of the coil's performance under real operating conditions (the presence of conducting tissue will inevitably alter the magnetic field) it is not possible to simulate the heterogeneity of live subjects with a simple flood-field phantom, nor would it be practical to use butchered animal parts instead. While a small sample will not load the coil appreciably, the coil could be matched especially for such a loading condition, or the subject's loading could be simulated using resistors of appropriate resistance and power handling ability [25].

In the most general case in which the mode balance and orthogonality are less than perfect, the field is elliptically polarised, with varying degrees of amplitude, and polarisation distribution throughout the coil volume. Bearing in mind that such fields can be decomposed into two counter-rotating circularly polarised fields, these characteristics are measured as follows.

1. The amplitude and homogeneity of the main, NMR-inducing component is determined from a non-linear least squares fit [26] of the nuclear signal amplitude, $S(\tau)$, to the model $S(\tau) = S_0|\sin\gamma B_1\tau|$. The length, τ, of the hard pulse is incremented in several steps to span the 180° pulse condition for maximal precision [27]. If an accurate means to measure transmitter power is available (i.e., the software controls of the NMR console are usually not precise enough), the input sensitivity of the coil can then be calculated.

2. The amplitude of the counter-rotating component, which should be zero ideally, contributes only to losses in the sample. It is determined by inverting the phase relationship of the two quadrature signals during reception only. While keeping input power constant, the relative RF amplitude of the two components is

determined by comparing nuclear signal amplitudes, S_n and S_r according to the equation

$$\frac{S_r}{S_n} = \frac{\sin \gamma B_{1r} \tau}{\sin \gamma B_{1n} \tau}, \tag{6.7}$$

where the subscript n refers to normal phase connection and the subscript r refers to the reversal of phase. The pulse duration τ is the same for both. The validity of this expression rests on the constancy of the mode which is used on transmission.

Such measurements can be repeated at various locations within the coil to determine their spatial distribution; however, since this is a very time-consuming technique the procedures in the next section are often preferred.

6.5.2 Field Mapping with Flood-Field Phantoms

Mapping of the B_1 field distribution inside the probe can also be accomplished by using an imaging sequence on a uniform phantom such as a bottle of water or oil. If the field distribution were perfectly uniform one would see an image having uniform intensity throughout the phantom. Techniques that measure the B_1 field amplitude from multiple images acquired using different flip angles have been reported in refs. [28, 29].

Care must be exercised when constructing the phantom so that it does not alter the B_1 field distribution excessively. This is especially important at higher frequencies where field focussing and dielectric resonance effects become more significant [30]. These effects are often observable in aqueous phantoms because of the high relative permittivity of water ($\epsilon_r \sim 80$) and because of the shielding effect of the finite conductivity of the solution. These problems due to conductivity and high permittivity can be dramatically reduced by using a low-permittivity oil instead (e.g., transformer oil) [31]. However, because of the low loss tangent of the oil and consequently low losses, the same methods as §6.5.1 must be used to assure a good coil match.

6.6 *In-Vivo* NMR Measurements

6.6.1 Anatomical Imaging

The noise in an $N \times N$ NMR data set propagates through the standard Fourier transform image reconstruction according to the formula $\sigma_I^2 = \sigma_D^2/N$, where σ_I and σ_D are the noise variances of the image and original data, respectively [32, p.246]. A discussion of image SNR and contrast-to-noise ratio (CNR) as a function of image pixel size is given in ref. [33]. In contrast to imaging techniques that employ ionising radiation, in MR imaging the choice of pixel size is critical because excessively small pixels lead to a loss in SNR that cannot be reversed by averaging adjacent pixels.

Anatomical images can be used to compare RF coils by taking care to produce equal flip angles with the excitation pulses and comparing the SNR's measured on the image. The images must be reconstructed with the same scaling factors, and the signal amplitude is measured as an average over a representative region where it is reasonably uniform. The noise amplitude is estimated by calculating the standard deviation of the image intensity in a region where there is no signal (neither real nor artefact), e.g., at one of the corners.

6.6.2 Spectroscopy

The noise performance of RF probes can also be compared in-vivo by using localised spectroscopic sequences such as STEAM [34] or PRESS [35]. The spectra must be from the same anatomical region and the same subject, in order to avoid variations in signal intensity due to differences in the concentrations of metabolites. The signal-to-noise ratio is measured by comparing the areas of the metabolite peaks relative to the amplitude of the noise that is superimposed. Examples of such comparisons are found in references [36, 37] and in Chapter 3.

Bibliography

[1] C.N. Chen and David I. Hoult. *Biomedical Magnetic Resonance Technology.* Medical Science Series. Adam Hilger, Bristol, UK, 1989.

[2] Frederick Emmons Terman. *Electronic and Radio Engineering.* McGraw-Hill, New York, fourth edition, 1955.

[3] Chuck Hutchinson, Joel Kleinman, and Dean R. Straw, editors. *The ARRL Handbook for Radio Amateurs.* American Radio Relay League, Newington, Conn., 78th edition, November 2000.

[4] S. Ramo, J.R. Whinnery, and T. Van Duzer. *Fields and Waves in Communication Electronics.* John Wiley, New York, third edition, 1994.

[5] Herbert P. Neff, Jr. *Introductory Electromagnetics.* John Wiley, New York, 1991.

[6] Markus Vester, Florian Steinmeyer, Bernhard Roas, Günther Thummes, and Kai Klundt. High-temperature superconducting surface coils with liquid nitrogen or pulse tube refrigeration. In *Proceedings of the ISMRM 5th Annual Meeting*, volume 3, page 1528, 1997.

[7] Axel Haase, Florian Odoj, Markus Von Kienlin, Jan Warnking, Florian Fidler, Alexander Weisser, Mathias Nittka, Eberhard Rommel, Titus Lanz, Bernhard Kalusche, and Mark Griswold. NMR probeheads for *in vivo* applications. *Concepts in Magnetic Resonance*, 12(6):361–388, 2000.

[8] Jürgen Link. The design of resonator probes with homogeneous radiofrequency fields. *NMR Basic Principles and Progress*, 26:3–31, 1992.

[9] John F. Schenck. Radiofrequency coils: Types and characteristics. In Michael J. Bronskill and Perry Sprawls, editors, *The Physics of MRI: 1992 AAPM Summer*

School Proceedings, pages 98–134. American Institute of Physics, Woodbury, NY, 1993.

[10] Cecil E. Hayes and Matthew G. Eash. Shield for decoupling RF and gradient coils in an NMR apparatus. U.S. Patent 4642569, Feb. 1987.

[11] John D. Kraus and Ronald J. Marhefka. *Antennas for All Applications*. McGraw-Hill, New York, third edition, 2002.

[12] Peter B. Roemer, William A. Edelstein, Cecil E. Hayes, and Matthew G. Eash. Method for providing multiple coaxial cable connections to a radio-frequency antenna without baluns. U.S. Patent 4887039, Dec. 12 1989.

[13] Carlo G. Someda. *Electromagnetic Waves*. Chapman & Hall, New York, 1998.

[14] Philip H. Smith. *Waveguide, Circuit and Component Analysis*. McGraw-Hill, New York, 1969.

[15] S. Frankel. Reactance networks for coupling between unbalanced and balanced circuits. *Proceedings of the IRE*, 29:486–493, September 1941.

[16] David M. Peterson, G. Randy Duensing, and J.R. Fitzsimmons. MRI basics and coil design principles. *RF Design*, pages 56–64, January 1997.

[17] G.R. Duensing and S.M. Varosi. Novel circuit provides true balanced connection for RF coils. In *Proceedings of the ISMRM 5th Annual Meeting*, volume 3, page 1525, 1997.

[18] Edward E. Ginzton. *Microwave Measurements*. McGraw-Hill, New York, 1957.

[19] J.R. Ashley and F.M. Palka. Reflection coefficient measurement of microwave resonator Q factors. *The Microwave Journal*, pages 35–39, June 1971.

[20] George Sergiadis. Performance evaluation of whole-body NMR scanner antenna systems. *Magnetic Resonance in Medicine*, 2:328–335, 1985.

[21] H. Wen, T.J. Denison, R.W. Singerman, and R.S. Balaban. The intrinsic signal-to-noise ratio in human cardiac imaging at 1.5, 3, and 4 T. *Journal of Magnetic Resonance*, 125:65–71, 1997.

[22] C-N. Chen, V.J. Sank, S.M. Cohen, and D.I. Hoult. The field dependence of NMR imaging I: Laboratory assessment of signal-to-noise ratio and power deposition. *Magnetic Resonance in Medicine*, 3:722–729, 1986.

[23] Luc Darrasse and Ghazi Kassab. Quick measurement of NMR-coil sensitivity with a dual-loop probe. *Review of Scientific Instruments*, 64(7):1841–1844, July 1993.

[24] P.B. Roemer, W.A. Edelstein, Cecil E. Hayes, S.P. Souza, and O.M. Mueller. The NMR phased array. *Magnetic Resonance in Medicine*, 16:192–225, 1990.

[25] W.A. Edelstein, P.A. Bottomley, and L.M. Pfeifer. A signal-to-noise calibration procedure for NMR imaging systems. *Medical Physics*, 11(2):180–185, 1984.

[26] E. Carson, C. Cobelli, and L. Finkelstein. *The Mathematical Modeling of Metabolic and Endocrine Systems*. John Wiley & Sons, New York, 1983.

[27] David I. Hoult, C.-N. Chen, and V.J. Sank. Quadrature detection in the laboratory frame. *Magnetic Resonance in Medicine*, 1:339–353, 1984.

[28] C.H. Oh, S.K. Hilal, Z.H. Cho, and I.K. Mun. Radio frequency field intensity mapping using a composite spin-echo sequence. *Magnetic Resonance in Medicine*, 8:21–25, 1990.

[29] R. Stollberger and P. Wach. Imaging the active B_1 field *in vivo*. *Magnetic Resonance in Medicine*, 35:246–251, 1996.

[30] David I. Hoult. Sensitivity and power deposition in a high-field imaging experiment. *Journal of Magnetic Resonance Imaging*, 12:46–67, 2000.

[31] P.S. Tofts, G.J. Barker, T.L. Dean, H. Gallagher, A.P. Gregory, and R.N. Clarke. A low dielectric constant customized phantom design to measure RF coil nonuniformity. *Magnetic Resonance Imaging*, 15(1):69–75, 1997.

[32] Zhi-Pei Liang and Paul C. Lauterbur. *Priciples of Magnetic Resonance Imaging: A Signal Processing Perspective*. IEEE Press Series on Biomedical Engineering. IEEE Press, 2000.

[33] W.A. Edelstein, G.H. Glover, C.J. Hardy, and R.W. Redington. The intrinsic signal-to-noise ratio in NMR imaging. *Magnetic Resonance in Medicine*, 3:604 618, 1986.

[34] Jens Frahm, Klaus-Dietmar Merboldt, and Wolfgang Hänicke. Localized proton spectroscopy using stimulated echoes. *Journal of Magnetic Resonance*, 72:502–508, 1987.

[35] P.A. Bottomley. Selective volume method for performing localized NMR spectroscopy. U.S. Patent 4480228, 1984.

[36] Enzo A. Barberi, J.S. Gati, Brian K. Rutt, and Ravi S. Menon. A transmit-Only/Receive-only (TORO) RF system for high-field MRI/MRS applications. *Magnetic Resonance in Medicine*, 43:284–289, 2000.

[37] Terry A. Riauka, Nicola F. De Zanche, Richard B. Thompson, Fred E. Vermeulen, Clarence E. Capjack, and Peter S. Allen. A numerical approach to non-circular birdcage RF coil optimization: Verification with a fourth-order coil. *Magnetic Resonance in Medicine*, 41:1180–1188, 1999.

Chapter 7

Summary and Conclusions

The primary objective of this thesis was to develop a method to design, build and test NMR radio frequency probes constructed on non-circular cylinders that conform to particular anatomical regions. As expected, by tailoring the geometry of the probe to the head, an improvement in the quality of the acquired signal (SNR) has resulted. Reciprocally, an improvement in the input sensitivity (see Eq. (1.10b)) of the probe is also observed. This method is applicable to a wide variety of cross-sectional shapes and to both the birdcage and TEM coil topologies.

7.1 Theoretical Analysis

The theoretical part of the work included in this thesis can be divided into two broad categories. The first category includes methods for the design of RF coils on non-circular cylindrical shapes to take advantage of potential improvements in SNR and coil sensitivity. The second deals with methods to model the high-frequency behaviour of probes such as the birdcage coil or the TEM resonator. Chapter 4 brings together both methodologies for the design of non-circular TEM resonators.

While improving SNR is the primary goal of this research project, another potential reason to construct coils on non-circular formers is for use inside elliptical gradient coils, where dimensional conflicts may exclude the use of circular coils. An earlier ap-

proach employed at the in-vivo NMR research facility of the University of Alberta to design tailored RF coils was essentially numerical, while the methods utilised in this thesis are principally analytical. Consequently they can be implemented using very limited computational power. The complex representation of magnetic fields is used in conjunction with the techniques of conformal mapping to solve boundary-value problems such as the field inside a non-circular RF shield. The optimal placement of birdcage coil conductors on an oval former can also be reduced to a boundary-value problem that is solved using conformal mapping. One apparent limitation of the complex representation is that it cannot deal directly with three-dimensional field distributions. However, since both the birdcage and TEM coils are cylindrical, and the fields produced inside are largely transverse electromagnetic (TEM), the two-dimensional field distributions can be extended to three dimensions, for example, by multiplication with a factor that accounts for the phase of the propagating wave. This is a consequence of the separability of the Helmholtz equation into longitudinal and transverse components [1, §8.2-8.3] which, although rigorously valid only in the case of infinitely long transmission lines, is known to yield quantitatively accurate results also for lines of finite length.

The conformal mapping method grew out of some prior work on the elliptical birdcage coil by Leifer [2]. Our methods, however, are applicable to almost any cylindrical shape, and provide both the optimal placement of the longitudinal current elements as well as the appropriate contour on which to construct the shield. The field produced by a coil designed in this manner is therefore highly uniform, similarly to the gold-standard circular birdcage coil. The shape that was chosen for the prototype coil is the oval of Cassini, named after the 17^{th} century astronomer who introduced this oval shape to interpret the orbits of the planets [3]. The ovals of Cassini are able to approximate the human anatomy more accurately than the ellipse, and the mapping functions are known and have simple algebraic expressions.

The effort to apply this method to a general cross-section has also shed light on

some properties that are unique to the elliptical cross-section. In Chapter 2 it is shown that the optimal shield for a coil constructed on an elliptical former should be constructed on a confocal elliptical cylinder. Furthermore, the geometric sensitivities of such a coil have simple algebraic expressions that are functions of the dimensions alone. While, similarly to other oval shapes, the two sensitivities that correspond to the two field orientations are different, the ideal shield contours do coincide, which is shown not to be the case for any other oval shape.

In addition to the conformal mapping methods that are used to determine the optimal placement of the coil's longitudinal conductors and shield, high-frequency multiconductor transmission line theory has been successfully extended to the modal analysis of TEM resonators built on such oval shapes as the oval of Cassini. Two such designs are shown, one intended for linear operation, and the other for quadrature operation to take full advantage of the improvement in SNR.

Multiconductor transmission line theory has also been applied with success to predict the high-frequency behaviour of the birdcage coil. While the original authors [4] that applied this theory to the TEM coil believed that it was not applicable to the birdcage, with some modifications it has been shown to give results that are quantitatively accurate.

7.2 Experimental Validation

The experimental work completed for this thesis focusses on a birdcage coil built for proton imaging and spectroscopy at 3 T on an oval of Cassini having dimensions adequate for the average adult head.

While the conformal mapping methods allow us to determine the geometry of the coil, electrical variables of the coil such as the capacitances could not be calculated analytically with accuracy and therefore a numerical method was used to determine the values of capacitance that would permit the coil to resonate at the desired frequency. This optimisation algorithm used a method of moments package (NEC-2) to

perform the modal analysis of the coil with each successive set of capacitances until a suitable set was found. After several days of computations, the set of capacitances that was produced worked perfectly in the prototype coil, producing two degenerate and uniform linear-field modes.

Another coil, circular in cross-section, was also constructed as a gold standard to evaluate the performance of the oval coil. The dimensions and materials used for the two coils are identical except for the reduced minor diameter of the Cassinian coil. Measurements of field uniformity are nearly identical, indicating that coils designed using the conformal mapping methods are indeed able to produce highly uniform fields. More importantly, an improvement in SNR of approximately 20% was observed in anatomical images as well as spectroscopic data from the brain. A maximum of 30% would be expected if patient losses were negligible.

The circular coil was also used to validate the multiconductor transmission line model of the birdcage coil, and excellent agreement was found between the calculated and measured resonance spectra.

7.3 Future Directions

There are many ways, both practical and theoretical, in which the research conducted for this thesis will be expanded and continued.

The oval TEM coils of Chapter 4 should be constructed and their resonance spectra should be compared to those predicted by theory. It is important to validate the accuracy of the multiconductor transmission line model, including the methods used to calculate the inductance matrix. Subsequent theoretical investigations could be aimed at methods for determining the optimal termination capacitances that are required for resonance at the correct frequency. This is essentially a problem of assigning given eigenvalues and eigenvectors to a matrix.

The multiconductor transmission line model should also be validated further by constructing some birdcage coils to operate at higher frequencies (e.g., 200 MHz for

the facility's new 4.7T system). It should also be extended to deal with non-circular birdcage coils such as the Cassinian head coil constructed for the present thesis, for example to calculate the required capacitances without having to resort to time-consuming iterative numerical methods. Ultimately, the multiconductor transmission line model may also be used to study methods of maintaining the leg currents more uniform along their length in order to extend the frequency range of the birdcage coil without suffering a degradation in axial field homogeneity.

Bibliography

[1] S. Ramo, J.R. Whinnery, and T. Van Duzer. *Fields and Waves in Communication Electronics.* John Wiley, New York, third edition, 1994.

[2] Mark C. Leifer. Theory of the quadrature elliptic birdcage coil. *Magnetic Resonance in Medicine*, 38:726–732, 1997.

[3] Jean Baptiste Joseph Delambre. *Histoire de l'Astronomie Moderne*, volume 2. Johnson Reprint Corporation, New York, 1969.

[4] Brian A. Baertlein, Ö. Özbay, T. Ibrahim, R. Lee, Y. Yu, A. Kangarlu, and P.-M. L. Robitaille. Theoretical model for an MRI radio frequency resonator. *IEEE Transactions on Biomedical Engineering*, 47(4):535–546, 2000.

Appendix A

Comments on "Theoretical Model for an MRI Radio Frequency Resonator"[1]

In a recent paper [1] Baertlein et al. describe an analytical model for the so-called TEM resonator used as a radio frequency probe in high-field magnetic resonance imaging. The unloaded resonator is modelled using multiconductor transmission line theory, which allows a calculation of the resonant frequencies to be made based on the geometry and physical parameters. Their approach is a detailed and practical contribution to the work that has been carried out since the invention of the TEM coil [2] in order to make an accurate prediction of its resonant behaviour.

The comments in the present note stem from an inconsistency between the definition of the voltage reflection matrix [3] in Eq. (11) and the sign of the left-hand side of Eq. (10), which should be positive. Although this sign difference could easily be typographical in nature, it appears to have more profound consequences in later sections where the authors discuss the field patterns produced at resonance. For example, they suggest that there is an intrinsic difference between birdcage coils and TEM coils because, they conclude, the latter produce electric and magnetic field

[1] A version of this appendix has been accepted for publication in the *IEEE Transactions on Biomedical Engineering*.

maxima at the same points along the longitudinal (axial) direction of the coil. In contrast, high-pass birdcage coils are known to produce an electric field *minimum* at the center of the coil [4], which is desirable to limit both the RF power deposition in the patient, and, by reciprocity, the noise generated on reception of the nuclear signal. [5]

The conclusion that TEM coils have coincident electric and magnetic field maxima, however, seems at variance with the application of Maxwell's equations. Under the assumption of transverse electric (**E**) and magnetic (**H**) fields, the Helmholtz equation for the electric field reduces to

$$\frac{\partial^2 \mathbf{E}}{\partial z^2} = -k^2 \mathbf{E} \tag{A.1}$$

where $k = 2\pi/\lambda = \omega\sqrt{\mu\epsilon}$ is the wavenumber, and z is the direction of propagation (coil axis). Equation (A.1) is separable into two one-dimensional Helmholtz equations, one for each Cartesian field component, which may then be treated independently. For standing waves, such as in the TEM resonator, the general solutions of Eq. (A.1) are

$$E_x = E_{0,x}\cos(kz + \phi_x) \tag{A.2}$$

$$E_y = E_{0,y}\cos(kz + \phi_y), \tag{A.3}$$

where the complex amplitudes $E_{0,x}, E_{0,y}$ and the spatial phases ϕ_x, ϕ_y are the independent parameters describing the waves. By applying Maxwell's curl equation for the electric field, $\nabla \times \mathbf{E} = -i\omega\mu\mathbf{H}$, we obtain the magnetic fields for the two orthogonal polarisations,

$$H_y = -iE_{0,x}\sqrt{\frac{\epsilon}{\mu}}\sin(kz + \phi_x) \tag{A.4}$$

$$H_x = iE_{0,y}\sqrt{\frac{\epsilon}{\mu}}\sin(kz + \phi_y), \tag{A.5}$$

respectively. Equations (4) and (5) demonstrate that for each mode, the coupled electric and magnetic fields are geometrically orthogonal, they are in phase quadrature

and their maxima (as well as their minima) along the z direction are separated by a distance of $\lambda/4$. This spatial distribution is not, as stated in [1], the same for electric and magnetic fields, but is totally analogous to their behaviour in the birdcage coil.

As a consequence, the TEM coil will, like the high-pass birdcage coil, have an electric field minimum at the coil center, thus limiting electrical losses in the load. We conclude that the TEM coil may be capable of equal or better noise performance than the birdcage coil and, hence, should not be dismissed as a high-field magnetic resonance probe.

Bibliography

[1] Brian A. Baertlein, Ö. Özbay, T. Ibrahim, R. Lee, Y. Yu, A. Kangarlu, and P.-M. L. Robitaille. Theoretical model for an MRI radio frequency resonator. *IEEE Transactions on Biomedical Engineering*, 47(4):535–546, 2000.

[2] Peter Röschmann. High-frequency coil system for a magnetic resonance imaging apparatus. U.S. Patent 4746866, May 1988.

[3] J.A. Brandão Faria. *Multiconductor Transmission-Line Structures: Modal Analysis Techniques*. John Wiley & Sons, Inc., New York, NY, 1993.

[4] Peter M. Joseph and Mohamed Saadi-Elmadjra. Electric field measurements in cylindrical imaging coils. *Journal of Magnetic Resonance*, 75:199–212, 1987.

[5] Ogan Ocali and Ergin Atalar. Ultimate intrinsic signal-to-noise ratio in MRI. *Magnetic Resonance in Medicine*, 39:462–473, 1998.

Appendix B

Programs Used for Modal Analysis and Capacitor Optimisation of the Cassinian Birdcage Coil

B.1 Coil Capacitance Cost Function

The following Matlab® function calculates the cost which is minimised when optimising coil capacitances to produce degenerate orthogonal field modes having the postulated (co)sinusoidal rung current distribution. It calls NEC-2 to calculate the resonant frequencies and rung currents of the two linear modes. The optimisation itself is performed by using one of the pre-existing Matlab® optimisation functions (e.g. `fminsearch`).

```
function costfn=callNEC(caps)
% creates .nec file with capacitances and calls NEC

disp(caps); %row vector containing 8 independent capacitance
%values: C1,C2,C3,C4,C5,C12,C23,C34,C45

%file declarations:    NB must be changed by hand in the system calls!!!
nec_file_x='m_cass_x.nec';
nec_file_y='m_cass_y.nec';
out_file_x='m_cass_x.out'; %produced by NEC
out_file_y='m_cass_y.out';

%other declarations:
f0=127.7; % desired resonant frequency [MHz]
```

```
no_caps=72; % 72 capacitors altogether
param=zeros(1,3); % parameters of Lorentzian fit
capacitances=[caps';flipud(caps');caps';flipud(caps')]; %[pF]  factor 2 is
%because of symmetry (in series)
capacitances=capacitances.*([2 1 1 1 2 2 2 2 2 2 2 ...
2 2 2 1 1 1 2 2 1 1 1 2 2 2 2 2 2 2 2 2 2 2 1 1 1 2]');
capacitances=[capacitances;capacitances]; %in sequential order
loads=['LD  0   17    1    0      0.05        0.'; %around the coil:C1
   'LD  0   18    2    0       0.1        0.'; %C2
   'LD  0   19    2    0       0.1        0.'; %C3
   'LD  0   20    2    0       0.1        0.'; %C4
   'LD  0   21    2    0      0.05        0.'; %C5
   'LD  0   13    5    0      0.05        0.'; %these are on the legs: C12
   'LD  0   14    5    0      0.05        0.'; %C23
   'LD  0   15    5    0      0.05        0.'; %C34
   'LD  0   16    5    0      0.05        0.';  %C45
   'LD  0   78    5    0      0.05        0.'; %C45
   'LD  0   77    5    0      0.05        0.'; %C34
   'LD  0   76    5    0      0.05        0.'; %C23
   'LD  0   75    5    0      0.05        0.'; %C12
   'LD  0   83    2    0      0.05        0.'; %C5
   'LD  0   82    2    0       0.1        0.'; %C4
   'LD  0   81    2    0       0.1        0.'; %C3
   'LD  0   80    2    0       0.1        0.'; %C2
   'LD  0   79    1    0      0.05        0.'; %C1
   'LD  0  110    1    0      0.05        0.'; %C1
   'LD  0  111    2    0       0.1        0.'; %C2
   'LD  0  112    2    0       0.1        0.'; %C3
   'LD  0  113    2    0       0.1        0.'; %C4
   'LD  0  114    2    0      0.05        0.'; %C5
   'LD  0  106    5    0      0.05        0.'; %C12
   'LD  0  107    5    0      0.05        0.'; %C23
   'LD  0  108    5    0      0.05        0.'; %C34
   'LD  0  109    5    0      0.05        0.'; %C45
   'LD  0   47    5    0      0.05        0.'; %C45
   'LD  0   46    5    0      0.05        0.'; %C34
   'LD  0   45    5    0      0.05        0.'; %C23
   'LD  0   44    5    0      0.05        0.'; %C12
   'LD  0   52    2    0      0.05        0.'; %C5
   'LD  0   51    2    0       0.1        0.'; %C4
   'LD  0   50    2    0       0.1        0.'; %C3
   'LD  0   49    2    0       0.1        0.'; %C2
   'LD  0   48    1    0      0.05        0.'; %C1
   'LD  0   26    1    0      0.05        0.'; %bottom half of the coil:C1
   'LD  0   27    2    0       0.1        0.'; %C2
   'LD  0   28    2    0       0.1        0.'; %C3
   'LD  0   29    2    0       0.1        0.'; %C4
   'LD  0   30    2    0      0.05        0.'; %C5
```

```
    'LD  0   22    5    0      0.05        0.'; %C12
    'LD  0   23    5    0      0.05        0.'; %C23
    'LD  0   24    5    0      0.05        0.'; %C34
    'LD  0   25    5    0      0.05        0.'; %C45
    'LD  0   87    5    0      0.05        0.'; %C45
    'LD  0   86    5    0      0.05        0.'; %C34
    'LD  0   85    5    0      0.05        0.'; %C23
    'LD  0   84    5    0      0.05        0.'; %C12
    'LD  0   92    2    0      0.05        0.'; %C5
    'LD  0   91    2    0       0.1        0.'; %C4
    'LD  0   90    2    0       0.1        0.'; %C3
    'LD  0   89    2    0       0.1        0.'; %C2
    'LD  0   88    1    0      0.05        0.'; %C1
    'LD  0  119    1    0      0.05        0.'; %C1
    'LD  0  120    2    0       0.1        0.'; %C2
    'LD  0  121    2    0       0.1        0.'; %C3
    'LD  0  122    2    0       0.1        0.'; %C4
    'LD  0  123    2    0      0.05        0.'; %C5
    'LD  0  115    5    0      0.05        0.'; %C12
    'LD  0  116    5    0      0.05        0.'; %C23
    'LD  0  117    5    0      0.05        0.'; %C34
    'LD  0  118    5    0      0.05        0.'; %C45
    'LD  0   56    5    0      0.05        0.'; %C45
    'LD  0   55    5    0      0.05        0.'; %C34
    'LD  0   54    5    0      0.05        0.'; %C23
    'LD  0   53    5    0      0.05        0.'; %C12
    'LD  0   61    2    0      0.05        0.'; %C5
    'LD  0   60    2    0       0.1        0.'; %C4
    'LD  0   59    2    0       0.1        0.'; %C3
    'LD  0   58    2    0       0.1        0.'; %C2
    'LD  0   57    1    0      0.05        0.';]; %C1
exponent='E-12';

%
%creating NEC input files: both must be done here for some reason
%

% move preamble to NEC input file
!type pream_y.txt>m_cass_y.nec

% open nec_file_y in append text mode
fid_y=fopen(nec_file_y,'at');

% append load information.....rounded to 4 sig. digs. in order to fit
for t=1:no_caps
   number=num2str(capacitances(t));
   spaces=6-size(number,2);
   if spaces<1 %truncate if too many digits
```

```
      number=num2str(round(capacitances(t)*100)/100);%round 2 dec. places
      number=number(1,1:min([5;size(number,2)])); %make sure there are
      spaces=1; % only 5 characters max
   end
   fwrite(fid_y,[loads(t,:),blanks(spaces),number,exponent,char(10)],'uchar');
end;

%close file
fclose(fid_y);

% append epilogue to output file
!type epilog_y.txt>>m_cass_y.nec

% move preamble to output file
!type pream_x.txt>m_cass_x.nec

% open nec_file_x in append text mode
fid_x=fopen(nec_file_x,'at');

% append load information.....4 sig. digs.
for t=1:no_caps
   number=num2str(capacitances(t));
   spaces=6-size(number,2);
   if spaces<1 %truncate if too many digits
      number=num2str(round(capacitances(t)*100)/100);%round 2 dec. places
      number=number(1,1:min([5;size(number,2)])); %make sure there are
      spaces=1; % only 5 characters max
   end
   fwrite(fid_x,[loads(t,:),blanks(spaces),number,exponent,char(10)],'uchar');
end;

%close nec_file_x
fclose(fid_x);

% append epilogue to NEC input file
!type epilog_x.txt>>m_cass_x.nec

% return; %uncomment to create NEC files only

%         %
% X mode  %
%         %

%call nec
!nec2d_cmd m_cass_x

%read input parameters
file=out_file_x;
```

```
readfreq;

%probably better to do an interpolation
[resistance freq_index]=max(input_pars(:,7));
if (freq_index<=2)|(freq_index>=no_runs-1)
   disp('WARNING: resonant frequency too close to boundary!');
end
param=LSQCURVEFIT('lorentz',[0.02  0.03  127.7],frequencies,input_pars(:,7));
if ~isempty(param) %checks if curve fitting succeeded
   resfreq_x=param(1,3);
else
   resfreq_x=frequencies(freq_index);
end

disp(resfreq_x);

figure(3); %plot resistance peak
plot(frequencies,input_pars(:,7),'r-',resfreq_x*[1 1],[resistance 0],...
'r:',frequencies,lorentz(param,frequencies),'ro');
xlabel('[MHz]');
ylabel('[ohms]');

readnec;
legcur_x;

%        %
% Y mode %
%        %

%call nec
!nec2d_cmd m_cass_y

%read input parameters
file=out_file_y;
readfreq;

%probably better to do an interpolation
[resistance freq_index]=max(input_pars(:,7));
if (freq_index<=2)|(freq_index>=no_runs-1)
   %resfreq=frequencies(freq_index);
   disp('WARNING: resonant frequency too close to boundary!');
end
param=LSQCURVEFIT('lorentz',[0.02  0.03  127.7],frequencies,input_pars(:,7));
if ~isempty(param) %checks if curve fitting succeeded
   resfreq_y=param(1,3);
else
   resfreq_y=frequencies(freq_index);
end
```

```
disp(resfreq_y);

figure(3); %plot resistance peak
hold on
plot(frequencies,input_pars(:,7),'b-',resfreq_y*[1 1],[resistance 0],...
'b:',frequencies,lorentz(param,frequencies),'bo');
hold off

readnec;
legcur_y;

costfn=8*(abs(f0-resfreq_x)+abs(f0-resfreq_y))+(err_x+err_y)
```

B.2 Sample NEC-2 Command File

The following is a sample set of NEC-2 program cards that is produced by the Matlab® function above during the optimisation. Please refer to reference [1] for an explaination of the NEC-2 programming language.

```
CMCassinian head coil and shield prototype
CEsquare loop (X) excitation
GW 13   10    0.1374    0.0221     0.107    0.1374    0.0221        0.   0.00133
#element 1
GW 14   10    0.1171    0.0625     0.107    0.1171    0.0625        0.   0.00133
#element 2
GW 15   10    0.0791    0.0926     0.107    0.0791    0.0926        0.   0.00133
#element 3
GW 16   10    0.0281    0.1081     0.107    0.0281    0.1081        0.   0.00133
#element 4
GW 17    2      0.14        0.     0.107    0.1374    0.0221     0.107   0.00133
#end rings
GW 18    3    0.1374    0.0221     0.107    0.1171    0.0625     0.107   0.00133
GW 19    3    0.1171    0.0625     0.107    0.0791    0.0926     0.107   0.00133
GW 20    3    0.0791    0.0926     0.107    0.0281    0.1081     0.107   0.00133
GW 21    2    0.0281    0.1081     0.107        0.      0.11     0.107   0.00133
GW  0    2      0.01      0.01        0.      0.01      0.01      0.01     0.001
# excitation loop
GW  0    2      0.01      0.01      0.01      0.01        0.      0.01     0.001
GX  9  001             #reflect along z
#begin shield mesh
GW  0    1   0.16353        0.  -0.13000   0.16350   0.01070  -0.13000  0.003422
GW  0   14   0.16350   0.01070  -0.13000   0.16350   0.01070   0.16000  0.003422
GW  0    1   0.16350   0.01070   0.16000   0.16353        0.   0.16000  0.003422
```

```
GW  1   1  0.16350  0.01070 -0.13000  0.15990  0.03180 -0.13000  0.003422
GW  1  14  0.15990  0.03180 -0.13000  0.15990  0.03180  0.16000  0.003422
GW  1   1  0.15990  0.03180  0.16000  0.16350  0.01070  0.16000  0.003422
GW  2   1  0.15990  0.03180 -0.13000  0.15270  0.05180 -0.13000  0.003422
GW  2  14  0.15270  0.05180 -0.13000  0.15270  0.05180  0.16000  0.003422
GW  2   1  0.15270  0.05180  0.16000  0.15990  0.03180  0.16000  0.003422
GW  3   1  0.15270  0.05180 -0.13000  0.14250  0.07030 -0.13000  0.003422
GW  3  14  0.14250  0.07030 -0.13000  0.14250  0.07030  0.16000  0.003422
GW  3   1  0.14250  0.07030  0.16000  0.15270  0.05180  0.16000  0.003422
GW  4   1  0.14250  0.07030 -0.13000  0.12970  0.08660 -0.13000  0.003422
GW  4  14  0.12970  0.08660 -0.13000  0.12970  0.08660  0.16000  0.003422
GW  4   1  0.12970  0.08660  0.16000  0.14250  0.07030  0.16000  0.003422
GW  5   1  0.12970  0.08660 -0.13000  0.11480  0.10070 -0.13000  0.003422
GW  5  14  0.11480  0.10070 -0.13000  0.11480  0.10070  0.16000  0.003422
GW  5   1  0.11480  0.10070  0.16000  0.12970  0.08660  0.16000  0.003422
GW  6   1  0.11480  0.10070 -0.13000  0.09860  0.11240 -0.13000  0.003422
GW  6  14  0.09860  0.11240 -0.13000  0.09860  0.11240  0.16000  0.003422
GW  6   1  0.09860  0.11240  0.16000  0.11480  0.10070  0.16000  0.003422
GW  7   1  0.09860  0.11240 -0.13000  0.08140  0.12180 -0.13000  0.003422
GW  7  14  0.08140  0.12180 -0.13000  0.08140  0.12180  0.16000  0.003422
GW  7   1  0.08140  0.12180  0.16000  0.09860  0.11240  0.16000  0.003422
GW  8   1  0.08140  0.12180 -0.13000  0.06360  0.12890 -0.13000  0.003422
GW  8  14  0.06360  0.12890 -0.13000  0.06360  0.12890  0.16000  0.003422
GW  8   1  0.06360  0.12890  0.16000  0.08140  0.12180  0.16000  0.003422
GW  9   1  0.06360  0.12890 -0.13000  0.04550  0.13410 -0.13000  0.003422
GW  9  14  0.04550  0.13410 -0.13000  0.04550  0.13410  0.16000  0.003422
GW  9   1  0.04550  0.13410  0.16000  0.06360  0.12890  0.16000  0.003422
GW 10   1  0.04550  0.13410 -0.13000  0.02730  0.13740 -0.13000  0.003422
GW 10  14  0.02730  0.13740 -0.13000  0.02730  0.13740  0.16000  0.003422
GW 10   1  0.02730  0.13740  0.16000  0.04550  0.13410  0.16000  0.003422
GW 11   1  0.02730  0.13740 -0.13000  0.00910  0.13910 -0.13000  0.003422
GW 11  14  0.00910  0.13910 -0.13000  0.00910  0.13910  0.16000  0.003422
GW 11   1  0.00910  0.13910  0.16000  0.02730  0.13740  0.16000  0.003422
GW 12   1       0.  0.13910 -0.13000  0.00910  0.13910 -0.13000  0.003422
GW 12   1  0.00910  0.13910  0.16000       0.  0.13910  0.16000  0.003422
GW  0   1  0.16350  0.01070 -0.10929  0.16353       0. -0.10929  0.003422
GW  0   1  0.16350  0.01070 -0.08857  0.16353       0. -0.08857  0.003422
GW  0   1  0.16350  0.01070 -0.06786  0.16353       0. -0.06786  0.003422
GW  0   1  0.16350  0.01070 -0.04714  0.16353       0. -0.04714  0.003422
GW  0   1  0.16350  0.01070 -0.02643  0.16353       0. -0.02643  0.003422
GW  0   1  0.16350  0.01070 -0.00571  0.16353       0. -0.00571  0.003422
GW  0   1  0.16350  0.01070  0.01500  0.16353       0.  0.01500  0.003422
GW  0   1  0.16350  0.01070  0.03571  0.16353       0.  0.03571  0.003422
GW  0   1  0.16350  0.01070  0.05643  0.16353       0.  0.05643  0.003422
GW  0   1  0.16350  0.01070  0.07714  0.16353       0.  0.07714  0.003422
GW  0   1  0.16350  0.01070  0.09786  0.16353       0.  0.09786  0.003422
GW  0   1  0.16350  0.01070  0.11857  0.16353       0.  0.11857  0.003422
GW  0   1  0.16350  0.01070  0.13929  0.16353       0.  0.13929  0.003422
```

```
GW  1   1   0.16350   0.01070   0.13929   0.15990   0.03180   0.13929   0.003422
GW  1   1   0.16350   0.01070   0.11857   0.15990   0.03180   0.11857   0.003422
GW  1   1   0.16350   0.01070   0.09786   0.15990   0.03180   0.09786   0.003422
GW  1   1   0.16350   0.01070   0.07714   0.15990   0.03180   0.07714   0.003422
GW  1   1   0.16350   0.01070   0.05643   0.15990   0.03180   0.05643   0.003422
GW  1   1   0.16350   0.01070   0.03571   0.15990   0.03180   0.03571   0.003422
GW  1   1   0.16350   0.01070   0.01500   0.15990   0.03180   0.01500   0.003422
GW  1   1   0.16350   0.01070  -0.00571   0.15990   0.03180  -0.00571   0.003422
GW  1   1   0.16350   0.01070  -0.02643   0.15990   0.03180  -0.02643   0.003422
GW  1   1   0.16350   0.01070  -0.04714   0.15990   0.03180  -0.04714   0.003422
GW  1   1   0.16350   0.01070  -0.06786   0.15990   0.03180  -0.06786   0.003422
GW  1   1   0.16350   0.01070  -0.08857   0.15990   0.03180  -0.08857   0.003422
GW  1   1   0.16350   0.01070  -0.10929   0.15990   0.03180  -0.10929   0.003422
GW  2   1   0.15990   0.03180   0.13929   0.15270   0.05180   0.13929   0.003422
GW  2   1   0.15990   0.03180   0.11857   0.15270   0.05180   0.11857   0.003422
GW  2   1   0.15990   0.03180   0.09786   0.15270   0.05180   0.09786   0.003422
GW  2   1   0.15990   0.03180   0.07714   0.15270   0.05180   0.07714   0.003422
GW  2   1   0.15990   0.03180   0.05643   0.15270   0.05180   0.05643   0.003422
GW  2   1   0.15990   0.03180   0.03571   0.15270   0.05180   0.03571   0.003422
GW  2   1   0.15990   0.03180   0.01500   0.15270   0.05180   0.01500   0.003422
GW  2   1   0.15990   0.03180  -0.00571   0.15270   0.05180  -0.00571   0.003422
GW  2   1   0.15990   0.03180  -0.02643   0.15270   0.05180  -0.02643   0.003422
GW  2   1   0.15990   0.03180  -0.04714   0.15270   0.05180  -0.04714   0.003422
GW  2   1   0.15990   0.03180  -0.06786   0.15270   0.05180  -0.06786   0.003422
GW  2   1   0.15990   0.03180  -0.08857   0.15270   0.05180  -0.08857   0.003422
GW  2   1   0.15990   0.03180  -0.10929   0.15270   0.05180  -0.10929   0.003422
GW  3   1   0.15270   0.05180   0.13929   0.14250   0.07030   0.13929   0.003422
GW  3   1   0.15270   0.05180   0.11857   0.14250   0.07030   0.11857   0.003422
GW  3   1   0.15270   0.05180   0.09786   0.14250   0.07030   0.09786   0.003422
GW  3   1   0.15270   0.05180   0.07714   0.14250   0.07030   0.07714   0.003422
GW  3   1   0.15270   0.05180   0.05643   0.14250   0.07030   0.05643   0.003422
GW  3   1   0.15270   0.05180   0.03571   0.14250   0.07030   0.03571   0.003422
GW  3   1   0.15270   0.05180   0.01500   0.14250   0.07030   0.01500   0.003422
GW  3   1   0.15270   0.05180  -0.00571   0.14250   0.07030  -0.00571   0.003422
GW  3   1   0.15270   0.05180  -0.02643   0.14250   0.07030  -0.02643   0.003422
GW  3   1   0.15270   0.05180  -0.04714   0.14250   0.07030  -0.04714   0.003422
GW  3   1   0.15270   0.05180  -0.06786   0.14250   0.07030  -0.06786   0.003422
GW  3   1   0.15270   0.05180  -0.08857   0.14250   0.07030  -0.08857   0.003422
GW  3   1   0.15270   0.05180  -0.10929   0.14250   0.07030  -0.10929   0.003422
GW  4   1   0.14250   0.07030   0.13929   0.12970   0.08660   0.13929   0.003422
GW  4   1   0.14250   0.07030   0.11857   0.12970   0.08660   0.11857   0.003422
GW  4   1   0.14250   0.07030   0.09786   0.12970   0.08660   0.09786   0.003422
GW  4   1   0.14250   0.07030   0.07714   0.12970   0.08660   0.07714   0.003422
GW  4   1   0.14250   0.07030   0.05643   0.12970   0.08660   0.05643   0.003422
GW  4   1   0.14250   0.07030   0.03571   0.12970   0.08660   0.03571   0.003422
GW  4   1   0.14250   0.07030   0.01500   0.12970   0.08660   0.01500   0.003422
GW  4   1   0.14250   0.07030  -0.00571   0.12970   0.08660  -0.00571   0.003422
GW  4   1   0.14250   0.07030  -0.02643   0.12970   0.08660  -0.02643   0.003422
```

```
GW  4  1  0.14250  0.07030 -0.04714  0.12970  0.08660 -0.04714  0.003422
GW  4  1  0.14250  0.07030 -0.06786  0.12970  0.08660 -0.06786  0.003422
GW  4  1  0.14250  0.07030 -0.08857  0.12970  0.08660 -0.08857  0.003422
GW  4  1  0.14250  0.07030 -0.10929  0.12970  0.08660 -0.10929  0.003422
GW  5  1  0.12970  0.08660  0.13929  0.11480  0.10070  0.13929  0.003422
GW  5  1  0.12970  0.08660  0.11857  0.11480  0.10070  0.11857  0.003422
GW  5  1  0.12970  0.08660  0.09786  0.11480  0.10070  0.09786  0.003422
GW  5  1  0.12970  0.08660  0.07714  0.11480  0.10070  0.07714  0.003422
GW  5  1  0.12970  0.08660  0.05643  0.11480  0.10070  0.05643  0.003422
GW  5  1  0.12970  0.08660  0.03571  0.11480  0.10070  0.03571  0.003422
GW  5  1  0.12970  0.08660  0.01500  0.11480  0.10070  0.01500  0.003422
GW  5  1  0.12970  0.08660 -0.00571  0.11480  0.10070 -0.00571  0.003422
GW  5  1  0.12970  0.08660 -0.02643  0.11480  0.10070 -0.02643  0.003422
GW  5  1  0.12970  0.08660 -0.04714  0.11480  0.10070 -0.04714  0.003422
GW  5  1  0.12970  0.08660 -0.06786  0.11480  0.10070 -0.06786  0.003422
GW  5  1  0.12970  0.08660 -0.08857  0.11480  0.10070 -0.08857  0.003422
GW  5  1  0.12970  0.08660 -0.10929  0.11480  0.10070 -0.10929  0.003422
GW  6  1  0.11480  0.10070  0.13929  0.09860  0.11240  0.13929  0.003422
GW  6  1  0.11480  0.10070  0.11857  0.09860  0.11240  0.11857  0.003422
GW  6  1  0.11480  0.10070  0.09786  0.09860  0.11240  0.09786  0.003422
GW  6  1  0.11480  0.10070  0.07714  0.09860  0.11240  0.07714  0.003422
GW  6  1  0.11480  0.10070  0.05643  0.09860  0.11240  0.05643  0.003422
GW  6  1  0.11480  0.10070  0.03571  0.09860  0.11240  0.03571  0.003422
GW  6  1  0.11480  0.10070  0.01500  0.09860  0.11240  0.01500  0.003422
GW  6  1  0.11480  0.10070 -0.00571  0.09860  0.11240 -0.00571  0.003422
GW  6  1  0.11480  0.10070 -0.02643  0.09860  0.11240 -0.02643  0.003422
GW  6  1  0.11480  0.10070 -0.04714  0.09860  0.11240 -0.04714  0.003422
GW  6  1  0.11480  0.10070 -0.06786  0.09860  0.11240 -0.06786  0.003422
GW  6  1  0.11480  0.10070 -0.08857  0.09860  0.11240 -0.08857  0.003422
GW  6  1  0.11480  0.10070 -0.10929  0.09860  0.11240 -0.10929  0.003422
GW  7  1  0.09860  0.11240  0.13929  0.08140  0.12180  0.13929  0.003422
GW  7  1  0.09860  0.11240  0.11857  0.08140  0.12180  0.11857  0.003422
GW  7  1  0.09860  0.11240  0.09786  0.08140  0.12180  0.09786  0.003422
GW  7  1  0.09860  0.11240  0.07714  0.08140  0.12180  0.07714  0.003422
GW  7  1  0.09860  0.11240  0.05643  0.08140  0.12180  0.05643  0.003422
GW  7  1  0.09860  0.11240  0.03571  0.08140  0.12180  0.03571  0.003422
GW  7  1  0.09860  0.11240  0.01500  0.08140  0.12180  0.01500  0.003422
GW  7  1  0.09860  0.11240 -0.00571  0.08140  0.12180 -0.00571  0.003422
GW  7  1  0.09860  0.11240 -0.02643  0.08140  0.12180 -0.02643  0.003422
GW  7  1  0.09860  0.11240 -0.04714  0.08140  0.12180 -0.04714  0.003422
GW  7  1  0.09860  0.11240 -0.06786  0.08140  0.12180 -0.06786  0.003422
GW  7  1  0.09860  0.11240 -0.08857  0.08140  0.12180 -0.08857  0.003422
GW  7  1  0.09860  0.11240 -0.10929  0.08140  0.12180 -0.10929  0.003422
GW  8  1  0.08140  0.12180  0.13929  0.06360  0.12890  0.13929  0.003422
GW  8  1  0.08140  0.12180  0.11857  0.06360  0.12890  0.11857  0.003422
GW  8  1  0.08140  0.12180  0.09786  0.06360  0.12890  0.09786  0.003422
GW  8  1  0.08140  0.12180  0.07714  0.06360  0.12890  0.07714  0.003422
GW  8  1  0.08140  0.12180  0.05643  0.06360  0.12890  0.05643  0.003422
```

```
GW  8   1  0.08140  0.12180  0.03571  0.06360  0.12890  0.03571  0.003422
GW  8   1  0.08140  0.12180  0.01500  0.06360  0.12890  0.01500  0.003422
GW  8   1  0.08140  0.12180 -0.00571  0.06360  0.12890 -0.00571  0.003422
GW  8   1  0.08140  0.12180 -0.02643  0.06360  0.12890 -0.02643  0.003422
GW  8   1  0.08140  0.12180 -0.04714  0.06360  0.12890 -0.04714  0.003422
GW  8   1  0.08140  0.12180 -0.06786  0.06360  0.12890 -0.06786  0.003422
GW  8   1  0.08140  0.12180 -0.08857  0.06360  0.12890 -0.08857  0.003422
GW  8   1  0.08140  0.12180 -0.10929  0.06360  0.12890 -0.10929  0.003422
GW  9   1  0.06360  0.12890  0.13929  0.04550  0.13410  0.13929  0.003422
GW  9   1  0.06360  0.12890  0.11857  0.04550  0.13410  0.11857  0.003422
GW  9   1  0.06360  0.12890  0.09786  0.04550  0.13410  0.09786  0.003422
GW  9   1  0.06360  0.12890  0.07714  0.04550  0.13410  0.07714  0.003422
GW  9   1  0.06360  0.12890  0.05643  0.04550  0.13410  0.05643  0.003422
GW  9   1  0.06360  0.12890  0.03571  0.04550  0.13410  0.03571  0.003422
GW  9   1  0.06360  0.12890  0.01500  0.04550  0.13410  0.01500  0.003422
GW  9   1  0.06360  0.12890 -0.00571  0.04550  0.13410 -0.00571  0.003422
GW  9   1  0.06360  0.12890 -0.02643  0.04550  0.13410 -0.02643  0.003422
GW  9   1  0.06360  0.12890 -0.04714  0.04550  0.13410 -0.04714  0.003422
GW  9   1  0.06360  0.12890 -0.06786  0.04550  0.13410 -0.06786  0.003422
GW  9   1  0.06360  0.12890 -0.08857  0.04550  0.13410 -0.08857  0.003422
GW  9   1  0.06360  0.12890 -0.10929  0.04550  0.13410 -0.10929  0.003422
GW 10   1  0.04550  0.13410  0.13929  0.02730  0.13740  0.13929  0.003422
GW 10   1  0.04550  0.13410  0.11857  0.02730  0.13740  0.11857  0.003422
GW 10   1  0.04550  0.13410  0.09786  0.02730  0.13740  0.09786  0.003422
GW 10   1  0.04550  0.13410  0.07714  0.02730  0.13740  0.07714  0.003422
GW 10   1  0.04550  0.13410  0.05643  0.02730  0.13740  0.05643  0.003422
GW 10   1  0.04550  0.13410  0.03571  0.02730  0.13740  0.03571  0.003422
GW 10   1  0.04550  0.13410  0.01500  0.02730  0.13740  0.01500  0.003422
GW 10   1  0.04550  0.13410 -0.00571  0.02730  0.13740 -0.00571  0.003422
GW 10   1  0.04550  0.13410 -0.02643  0.02730  0.13740 -0.02643  0.003422
GW 10   1  0.04550  0.13410 -0.04714  0.02730  0.13740 -0.04714  0.003422
GW 10   1  0.04550  0.13410 -0.06786  0.02730  0.13740 -0.06786  0.003422
GW 10   1  0.04550  0.13410 -0.08857  0.02730  0.13740 -0.08857  0.003422
GW 10   1  0.04550  0.13410 -0.10929  0.02730  0.13740 -0.10929  0.003422
GW 11   1  0.02730  0.13740  0.13929  0.00910  0.13910  0.13929  0.003422
GW 11   1  0.02730  0.13740  0.11857  0.00910  0.13910  0.11857  0.003422
GW 11   1  0.02730  0.13740  0.09786  0.00910  0.13910  0.09786  0.003422
GW 11   1  0.02730  0.13740  0.07714  0.00910  0.13910  0.07714  0.003422
GW 11   1  0.02730  0.13740  0.05643  0.00910  0.13910  0.05643  0.003422
GW 11   1  0.02730  0.13740  0.03571  0.00910  0.13910  0.03571  0.003422
GW 11   1  0.02730  0.13740  0.01500  0.00910  0.13910  0.01500  0.003422
GW 11   1  0.02730  0.13740 -0.00571  0.00910  0.13910 -0.00571  0.003422
GW 11   1  0.02730  0.13740 -0.02643  0.00910  0.13910 -0.02643  0.003422
GW 11   1  0.02730  0.13740 -0.04714  0.00910  0.13910 -0.04714  0.003422
GW 11   1  0.02730  0.13740 -0.06786  0.00910  0.13910 -0.06786  0.003422
GW 11   1  0.02730  0.13740 -0.08857  0.00910  0.13910 -0.08857  0.003422
GW 11   1  0.02730  0.13740 -0.10929  0.00910  0.13910 -0.10929  0.003422
GW 12   1        0.  0.13910  0.13929  0.00910  0.13910  0.13929  0.003422
```

```
GW 12   1       0.   0.13910   0.11857   0.00910   0.13910   0.11857   0.003422
GW 12   1       0.   0.13910   0.09786   0.00910   0.13910   0.09786   0.003422
GW 12   1       0.   0.13910   0.07714   0.00910   0.13910   0.07714   0.003422
GW 12   1       0.   0.13910   0.05643   0.00910   0.13910   0.05643   0.003422
GW 12   1       0.   0.13910   0.03571   0.00910   0.13910   0.03571   0.003422
GW 12   1       0.   0.13910   0.01500   0.00910   0.13910   0.01500   0.003422
GW 12   1       0.   0.13910  -0.00571   0.00910   0.13910  -0.00571   0.003422
GW 12   1       0.   0.13910  -0.02643   0.00910   0.13910  -0.02643   0.003422
GW 12   1       0.   0.13910  -0.04714   0.00910   0.13910  -0.04714   0.003422
GW 12   1       0.   0.13910  -0.06786   0.00910   0.13910  -0.06786   0.003422
GW 12   1       0.   0.13910  -0.08857   0.00910   0.13910  -0.08857   0.003422
GW 12   1       0.   0.13910  -0.10929   0.00910   0.13910  -0.10929   0.003422
GX 31   110     #reflect along x&y
GE
LD  0   17   1   0      0.05          0. 65.01E-12
LD  0   18   2   0       0.1          0. 32.5E-12
LD  0   19   2   0       0.1          0. 32.5E-12
LD  0   20   2   0       0.1          0. 29E-12
LD  0   21   2   0      0.05          0. 64.99E-12
LD  0   13   5   0      0.05          0. 609.6E-12
LD  0   14   5   0      0.05          0. 610.1E-12
LD  0   15   5   0      0.05          0. 609.1E-12
LD  0   16   5   0      0.05          0. 610.2E-12
LD  0   78   5   0      0.05          0. 610.2E-12
LD  0   77   5   0      0.05          0. 609.1E-12
LD  0   76   5   0      0.05          0. 610.1E-12
LD  0   75   5   0      0.05          0. 609.6E-12
LD  0   83   2   0      0.05          0. 64.99E-12
LD  0   82   2   0       0.1          0. 29E-12
LD  0   81   2   0       0.1          0. 32.5E-12
LD  0   80   2   0       0.1          0. 32.5E-12
LD  0   79   1   0      0.05          0. 65.01E-12
LD  0  110   1   0      0.05          0. 65.01E-12
LD  0  111   2   0       0.1          0. 32.5E-12
LD  0  112   2   0       0.1          0. 32.5E-12
LD  0  113   2   0       0.1          0. 29E-12
LD  0  114   2   0      0.05          0. 64.99E-12
LD  0  106   5   0      0.05          0. 609.6E-12
LD  0  107   5   0      0.05          0. 610.1E-12
LD  0  108   5   0      0.05          0. 609.1E-12
LD  0  109   5   0      0.05          0. 610.2E-12
LD  0   47   5   0      0.05          0. 610.2E-12
LD  0   46   5   0      0.05          0. 609.1E-12
LD  0   45   5   0      0.05          0. 610.1E-12
LD  0   44   5   0      0.05          0. 609.6E-12
LD  0   52   2   0      0.05          0. 64.99E-12
LD  0   51   2   0       0.1          0. 29E-12
LD  0   50   2   0       0.1          0. 32.5E-12
```

```
LD  0   49    2    0      0.1        0. 32.5E-12
LD  0   48    1    0     0.05        0. 65.01E-12
LD  0   26    1    0     0.05        0. 65.01E-12
LD  0   27    2    0      0.1        0. 32.5E-12
LD  0   28    2    0      0.1        0. 32.5E-12
LD  0   29    2    0      0.1        0. 29E-12
LD  0   30    2    0     0.05        0. 64.99E-12
LD  0   22    5    0     0.05        0. 609.6E-12
LD  0   23    5    0     0.05        0. 610.1E-12
LD  0   24    5    0     0.05        0. 609.1E-12
LD  0   25    5    0     0.05        0. 610.2E-12
LD  0   87    5    0     0.05        0. 610.2E-12
LD  0   86    5    0     0.05        0. 609.1E-12
LD  0   85    5    0     0.05        0. 610.1E-12
LD  0   84    5    0     0.05        0. 609.6E-12
LD  0   92    2    0     0.05        0. 64.99E-12
LD  0   91    2    0      0.1        0. 29E-12
LD  0   90    2    0      0.1        0. 32.5E-12
LD  0   89    2    0      0.1        0. 32.5E-12
LD  0   88    1    0     0.05        0. 65.01E-12
LD  0  119    1    0     0.05        0. 65.01E-12
LD  0  120    2    0      0.1        0. 32.5E-12
LD  0  121    2    0      0.1        0. 32.5E-12
LD  0  122    2    0      0.1        0. 29E-12
LD  0  123    2    0     0.05        0. 64.99E-12
LD  0  115    5    0     0.05        0. 609.6E-12
LD  0  116    5    0     0.05        0. 610.1E-12
LD  0  117    5    0     0.05        0. 609.1E-12
LD  0  118    5    0     0.05        0. 610.2E-12
LD  0   56    5    0     0.05        0. 610.2E-12
LD  0   55    5    0     0.05        0. 609.1E-12
LD  0   54    5    0     0.05        0. 610.1E-12
LD  0   53    5    0     0.05        0. 609.6E-12
LD  0   61    2    0     0.05        0. 64.99E-12
LD  0   60    2    0      0.1        0. 29E-12
LD  0   59    2    0      0.1        0. 32.5E-12
LD  0   58    2    0      0.1        0. 32.5E-12
LD  0   57    1    0     0.05        0. 65.01E-12
FR  0    6    0    0    126.7      1.00          #frequency range
EX  0    0   57    0       1.        0.      0.       0.       0.       0.
#first element of first loop
EX  0    0 1011    0       1.        0.      0.       0.       0.       0.
XQ
EN
```

Bibliography

[1] G.J. Burke and A.J. Poggio. *Numerical Electromagnetics Code (NEC-2) Manual, Part III: User's Guide.* Lawrence Livermore National Laboratory, Livermore, CA, 1981.

Appendix C

The Method of Images for Currents and Magnetic Dipoles

The method of images has long been a useful tool to solve boundary value problems in electromagnetics.[1, Ch. XI] Although in two dimensions it is directly applicable only in cases where the boundary is circular or linear, it can be extended to more general shapes by the use of conformal mapping functions. Most texts illustrate this method for the electric field, but in two dimensions the results are easily applied to the magnetic field due to the formal analogies that exist between the two fields.[2, §7.25] This appendix contains results used in the previous chapters for the calculation of two-dimensional magnetic field distributions, and is provided as a reference to the reader.

C.1 Location of the Equivalent Source Line

When a transmission line is constructed by placing a circular conductive rod inside a cylindrical shield so that the two are parallel but not coaxial, the resultant magnetic field lines are circles whose centres lie on a line joining the centres of the rod and shield. Figure C.1 shows the magnetic field distribution in the region between the rod and shield. This distribution is obtained in reference [3, §25] by considering the field produced by two parallel filamentary currents of equal intensity flowing in

opposite directions. These two line currents are considered to be *images* of each other with respect to the plane equidistant to the two lines.

If we define R to be the radius of the shield, r to be the radius of the rod, c to be the distance between the centres of rod and shield, then the distance f between the centre of the rod and the position of the equivalent filamentary current is given by

$$f = b - \sqrt{b^2 - r^2}, \tag{C.1a}$$

where

$$b = \frac{1}{2}\left(\frac{R^2 - r^2}{c} - c\right). \tag{C.1b}$$

It is important not to neglect the effect of the displacement f when calculating quantities such as inductance with a high degree of accuracy.

The image current is located along the line from the centre of the shield to the centre of the rod, at a radial distance given by $R^2/(c + f)$.

C.2 Image of a Magnetic Dipole

The behaviour of a magnetic dipole in a cylindrical shield is useful to account for the field distortion produced by the presence of longitudinal conducting rods such as those found in the birdcage and TEM resonators. Under the influence of the field produced by a source within the shield, the currents induced on a perfectly-conducting rod will satisfy the boundary conditions by producing a field identical to the field used to calculate the ideal current distributions of the circular birdcage in Chapter 2. In the following analysis it will be assumed that the incident field that is displaced is essetially uniform, and therefore the field produced by the currents on the rod will be that of a two-dimensional magnetic dipole.

A magnetic dipole can be thought of as two filamentary currents carrying equal currents of intensity I in opposite directions and separated by an infinitesimal distance δ. The magnetic moment per unit length can then be defined as $P = I\delta$.

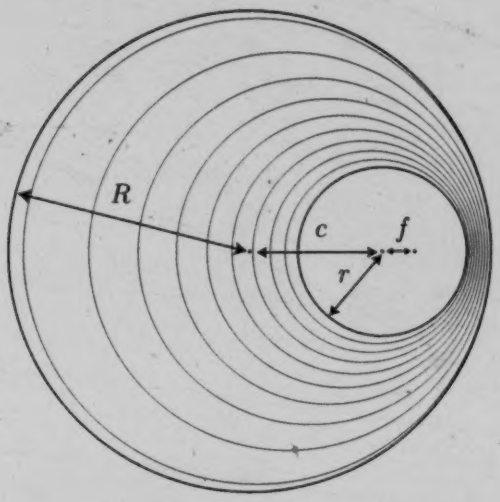

Figure C.1: Magnetic field lines of a current-carrying rod enclosed in a cylindrical shield. Notice that the equivalent line source is not coaxial with the rod but is at a distance f from the rod's axis. The image current is located at a radial distance of $R^2/(c+f)$ from the centre of the shield.

Alternatively, if the incident uniform magnetic field has an amplitude of H_1, and the radius of the rod is r, the magnetic moment produced by the rod to counter the incident field will be given by $P = H_1 r^2$, and its complex potential is exactly that of Eqs. (2.10) depending on its orientation.

The effect of the shield is handled by applying the method of images to the single line currents, and results in the creation of an image dipole having moment $P_i = P(R/c)^2$ at a radial position of R^2/c, where R and c have the same meanings as those of the previous section. In addition to the its amplitude, the direction of the image dipole is also modified by a rotation around its axis. The angle between P_i and the vector joining the shield and dipole centres is equal but opposite to the angle between the vector and P. For example, if P is oriented radially then P_i will point in the same direction, whereas if P is oriented azimuthally then P_i will point in the opposite direction. Figure C.2 shows the magnetic field lines of a dipole enclosed in

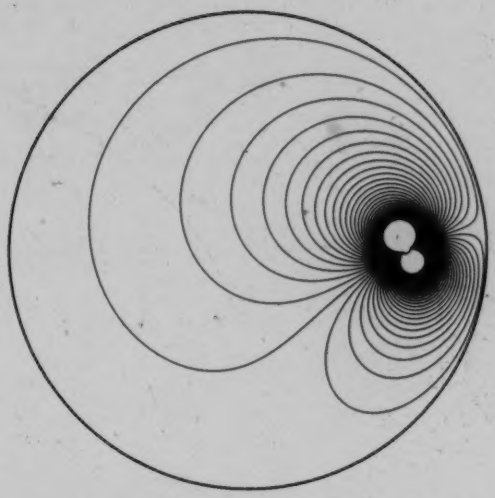

Figure C.2: Magnetic field lines of a magnetic dipole enclosed in a cylindrical shield. Such field distributions represent the field produced by the currents induced on a conducting rod in the presence of a field produced by another current inside the shield.

an ideal cylindrical shield and oriented at an arbitrary angle. The boundary condition of tangential magnetic field at the shield is seen to be fully satisfied.

Bibliography

[1] James Clerk Maxwell. *A Treatise on Electricity & Magnetism.* Dover, New York, third edition, 1954.

[2] W.R. Smythe. *Static and Dynamic Electricity.* McGraw-Hill, New York, third edition, 1968.

[3] Arnold Sommerfeld. *Electrodyamics.* Lectures on Theoretical Physics. Academic Press, New York, 1952.